

Multiscale study and modeling of dispersion properties relevant for liquid-liquid extraction : adaptation of breakup and coalescence kernels to industrial processes

Simone Castellano

▶ **To cite this version:**

Simone Castellano. Multiscale study and modeling of dispersion properties relevant for liquid-liquid extraction : adaptation of breakup and coalescence kernels to industrial processes. Chemical and Process Engineering. Université de Lyon, 2019. English. NNT : 2019LYSE1243 . tel-02505193

HAL Id: tel-02505193
https://theses.hal.science/tel-02505193

Submitted on 11 Mar 2020

HAL is a multi-disciplinary open access archive for the deposit and dissemination of scientific research documents, whether they are published or not. The documents may come from teaching and research institutions in France or abroad, or from public or private research centers.

L'archive ouverte pluridisciplinaire **HAL**, est destinée au dépôt et à la diffusion de documents scientifiques de niveau recherche, publiés ou non, émanant des établissements d'enseignement et de recherche français ou étrangers, des laboratoires publics ou privés.

N°d'ordre NNT : xxx

THESE de DOCTORAT DE L'UNIVERSITE DE LYON

opérée au sein de

l'Université Claude Bernard Lyon 1

Ecole Doctorale N° 206

Chimie de Lyon

Spécialité de doctorat : Génie des procédés

Soutenue publiquement le 05/11/2019, par :

Simone Castellano

Multiscale study and modeling of dispersion properties relevant for liquid-liquid extraction. Adaptation of breakup and coalescence kernels to industrial processes

---

Devant le jury composé de :

Professeur Lance Michel/Université Claude Bernard Lyon 1 Président

Professeur Baldyga Jerzy /Université de technologie de Varsovie Rapporteur
Professeur Nopens Ingmar/Université de Gand Rapporteur
Professeur Schaer Eric/Université de Lorraine Examinateur

Docteur Othman Nida/Université Claude Bernard Lyon 1 Directrice de thèse
Docteur Charton Sophie/Commissariat à l'Energie Atomique Co-directrice de thèse

Résumé en anglais

This PhD project deals with the study of the hydrodynamics of the dispersions in the liquid-liquid extractors employed in the nuclear recycle industry.

In the first part of the project, a zero-dimensional homogenous Population Balance Model (0D-PBM), based on the evaluation of the volume-averaged coalescence and breakup rates, is adopted to fit low-viscosity turbulent liquid-liquid dispersion experiments. The method accounts for the spatial inhomogeneities in mixing, namely for the probability density function of the turbulent kinetic energy dissipation in the apparatus.

In the second part of this study, a generalized model for the breakage and coalescence kernels, valid for the entire spectrum of turbulence, is proposed and validated. Most of the available kernels in literature indeed are based on the Kolmogorov second-order structure function, which is only valid in the *inertial subrange*. However, in many industrially encountered situations, most of the droplets may have size in the *dissipation range*, where the Kolmogorov second-order structure function does not apply. The generalized model is based on the Davidson second-order structure function, valid in the entire spectrum of turbulence.

In the last part of the study, a model that allows to simulate the hydrodynamic behavior of a pulsed column is proposed. The model is based on a 1D Population Balance Equation (1D-PBE), whose source terms were modeled through the generalized Coulaloglou and Tavlarides kernels. The turbulent inhomogeneities in the pulsed column were accounted through the probability density function of the turbulent dissipation rate. The model well reproduces the experimental Sauter mean diameters and the dispersed phase volume fractions in a compartment of the pulsed column.

Résumé en français

Ce projet de thèse porte sur l'étude de l'hydrodynamique des dispersions dans les extracteurs liquide-liquide utilisés dans l'industrie du recyclage nucléaire.

Dans la première partie du projet, un modèle de bilan de population homogène (0D-PBM), basé sur l'évaluation des taux moyens en volume de coalescence et de rupture, est proposé. La méthode tient compte des inhomogénéités spatiales dans le mélange, notamment de la fonction de densité de probabilité de la dissipation de l'énergie cinétique turbulente dans l'appareil. Le modèle est capable de reproduire les expériences de dispersion liquide-liquide turbulentes à faible viscosité.

Dans la deuxième partie de cette étude, un modèle généralisé pour les noyaux de rupture et coalescence, valable pour l'ensemble du spectre de la turbulence, est proposé et validé. La plupart des noyaux disponibles dans la littérature sont basés sur la fonction de structure de second-ordre de Kolmogorov, qui n'est valable que dans le domaine inertiel. Cependant, dans des nombreuses situations rencontrées au niveau industriel, la plupart des gouttes peuvent avoir une taille dans le domaine dissipatif, où la fonction de structure de second-ordre de Kolmogorov ne s'applique pas. Le modèle généralisé est basé sur la fonction de structure de second ordre de Davidson, valable dans tout le spectre de la turbulence.

Dans la dernière partie de l'étude, un modèle permettant de simuler le comportement hydrodynamique d'une colonne pulsée est proposé. Le modèle est basé sur un bilan de population 1D, dont les termes source ont été modélisés à l'aide des noyaux de Coulaloglou et Tavlarides généralisés. Les inhomogénéités turbulentes dans la colonne pulsée ont été prises en compte par la fonction de densité de probabilité du taux de dissipation turbulent. Un bon accord modèle-expérience est obtenu en ce qui concerne le diamètre et la concentration moyenne des gouttes dans un compartiment.

Summary

1. Introduction 19

2. Modeling of polydisperse systems 25

2.1. General PBE 25

2.2. Solving the 0D PBE 28

2.3. Turbulence theory 37

2.4. Breakage kernels 40

2.4.1. Coulaloglou and Tavlarides 40

2.4.2. The Alopaeus model 42

2.4.3. The Luo and Svendsen model 43

2.4.4. The Baldyga and Podgorska model 45

2.4.5. Daughter size distribution functions 46

2.5. Coalescence kernels 49

2.5.1. The Coulaloglou and Tavlarides model 49

2.5.2. The Sovova model 50

3. Materials and methods 53

3.1. Experiments 53

3.1.1. Aqueous and organic phases 53

3.1.2. Liquid-liquid contactors 55

3.1.3. The SOPAT probe and software 61

3.2. Numerical models 62

3.2.1. CFD simulations 62

3.2.2. Note on the single-phase assumption.....71

4. Turbulence inhomogeneity.....73

4.1. Volume-averaged turbulent dissipation rate ε.....73

4.2. Compartment method.....74

4.3. Volume-averaged kernels.....75

4.3.1. Population Balance Modelling.....75

4.3.2. Materials and methods.....77

4.3.3. Results and discussions.....80

4.3.4. Conclusions.....90

5. Improved kernel turbulence.....93

5.1. Generalized second-order structure function.....93

5.1.1. Breakage and Coalescence kernels.....95

5.2. Materials and methods.....96

5.2.1. Materials.....96

5.2.2. Experimental procedure.....97

5.2.3. 0D Population Balance Model.....98

5.2.4. Numerical details.....99

5.3. Results and discussions.....100

5.3.1. Parameters identification.....101

5.3.2. Low continuous phase viscosity.....103

5.3.3. High continuous phase viscosity.....107

5.4. Conclusions.....113

6. A hydrodynamic model of the pulsed column 116

6.1. Experimental case study 116

6.1.1. Experimental setup 116

6.1.2. Tested phase system 118

6.1.3. Experimental procedure 118

6.1.4. CFD simulations 119

6.2. Model development 121

6.2.1. 1D PBE model 121

6.2.2. Mass conservation 123

6.2.3. Droplet velocity 123

6.2.4. Breakage and Coalescence kernels 125

6.2.5. Structure of the model 125

6.2.6. Numerical resolution 126

6.2.7. Kernel computation 130

6.3. Results and discussions 131

6.3.1. CFD simulation results 131

6.3.2. Identification of the parameter values 135

6.3.3. Validation of the model 137

6.4. Conclusions 143

7. Conclusions & Perspectives 144

Annex I 146

Annex II 150

Notation.....154

Bibliography.....156

List of Figures

Figure 2.1: Representation of the daughter size distribution function proposed by Valentas and implemented by Coulaloglou and Tavlarides 47

Figure 2.2: Surface energy increase as function of the volume fraction of the daughter droplet 48

Figure 2.3: Examples of U-shaped (left) and M-shaped(right) daughter size distribution functions 48

Figure 3.1: Power number Np for different impellers taken from [55] 57

Figure 3.2: Geometry of the stirred tank reactor 58

Figure 3.3: Interior of the stirred tank reactor 59

Figure 3.4: Scheme of a pulsed column 60

Figure 3.5: Packing of the lab-scale column employed for the experiments [17] 60

Figure 3.6: Lab-scale pulsed column 61

Figure 3.7: SOPAT endoscopic probe 61

Figure 3.8: Surface mesh of the Mixel TT impeller 68

Figure 3.9: Section of the fluid subdomain where the MRF approach is applied 69

Figure 3.10: 2D mesh of 1 compartment of the pulsed column 70

Figure 3.11: Example of the probability density functions of ε obtained through a single (red) and a two (blue)-phase simulation of the STR at 800rpm. 72

Figure 4.1: Turbulent kinetic energy dissipation rate distribution (same volume-average value, i.e. ε = 1) in a stirred tank reactor employing a Mixel TT impeller and in a pulsed column 73

Figure 4.2: Turbulent kinetic energy rate dissipation distribution in a stirred tank reactor employing a Rushton turbine (ε =0.5) 74

Figure 4.3: Example of image treated through the SOPAT software. The half bottom image represents the photographed droplets. The half upper, the detected ones, enlightened by green circles. 78

Figure 4.4: Probability density functions, f(ε) for water (left) and Isane (right) at different impeller rotational speeds (600-700-800rpm). 80

Figure 4.5: Comparison of the probability density functions for Isane and water at 600rpm (top-left), 700rpm (top-right), 800rpm (bottom). 81

Figure 4.6: Space distributions of the turbulent dissipation rate, ε (m^2/s^3), at 600 rpm (left), 700rpm (center), 800 rpm (right) according to water-phase CFD simulation. 83

Figure 4.7: Time evolution of the droplet Sauter mean diameters for oil-in-water experiments at 1% (left) and 2% (right) volume fraction of Isane hold-up and 600rpm, 700rpm and 800rpm. 84

Figure 4.8: Time evolutions of the droplet Sauter mean diameters for the water-in-oil experiments at 1 % volume fraction of water hold-up and 600rpm, 700rpm and 800rpm. 85

Figure 4.9: Time evolutions of droplet Sauter mean diameters for oil-in-water (empty) and water-in-oil (plain) experiments at 1% disperse phase hold-up and at 600rpm (red) 700rpm (blue) and 800rpm (black) rotational speeds. 86

Figure 4.10: Parameters identification on oil in water experiments at 1% (circles) and 2% (rhombus) of Isane hold-up employing the pdf (blue) or assuming a uniform value (black) of ε. 87

Figure 4.11: Parameters testing on oil-in-water experiments at 1-2 % of Isane hold-ups employing the pdf or assuming a uniform value of ε. 89

Figure 4.12: Parameters testing on oil-in-water experiments at 1% volume fraction of water hold-up employing the pdf or assuming a uniform value of ε. 90

Figure 5.1: Energy spectrum representation of the eddies according to their wavelength in the energy-containing range and the inertial and dissipation subranges of turbulence. 94

Figure 5.2: Droplet caption with the SOPAT® probe (left) and detection (right, green circles). 97

Figure 5.3: Main steps and sequence of the numerical procedure. 100

Figure 5.4: Time-evolution of the droplet Sauter mean diameters for water-in-oil experiments: continuous phase viscosity 1.2 cP, water volume fraction of 2%, stirring rate of 600, 700, and 800 rpm. 101

Figure 5.5: Parameters identification of the "generalized model" on water-in-Isane experiments (error bar: 1% of the experimental value): continuous phase viscosity 1.2 cP, water volume fraction of 1 (left) – 2 (right) %, stirring rate of 600 rpm. 102

Figure 5.6: "Generalized model" testing on water-in-Isane experiments (error bar: 3% of the experimental value): continuous phase viscosity 1.2 cP, water volume fraction of 1 (top) – 2 (bottom) %, stirring rate of 700 (left) and 800 (right) rpm. 104

Figure 5.7: Examples of droplet number density function for water-in-Isane experiments: water volume fraction of 2%, stirring rate of 600 (green), 700 (red) and 800 (blue) rpm. 106

Figure 5.8: "Generalized model" testing on water-in-*Isane70%/Marcol30%* experiments (error bar: 3% of the experimental value): continuous phase viscosity 2.4 cP, water volume fraction of 1%, stirring rate of 600 (top-left), 700 (top-right), and 800 (bottom) rpm. 108

Figure 5.9: "Generalized model" testing on water-in-*Isane70%/Marcol30%* experiments (error bar: 3% of the experimental value): continuous phase viscosity 2.4 cP, water volume fraction of 2%, stirring rate of 600 (top-left), 700 (top-right), and 800 (bottom) rpm. 109

Figure 5.10: "Generalized model" testing on water-in-*Isane55%/Marcol45%* experiments (error bar: 3% of the experimental value): continuous phase viscosity 4.1 cP, water volume fraction of 1%, stirring rate of 600 (top-left), 700 (top-right), and 800 (bottom) rpm. 112

Figure 6.1: Lab-scale pulsed column with the SOPAT probe 117

Figure 6.2: Schematic representation of the model structure 126

Figure 6.3: Time-averaged turbulent dissipation rate distribution in a compartment at a pulsation of 3.5 cm/s 131

Figure 6.4: Time-averaged turbulent dissipation rate distribution in a compartment at pulsations of 4.5 cm/s (left) and 5.5 cm/s (right). 132

Figure 6.5: Time-averaged turbulent dissipation rate distribution in a compartment for a continuous phase flowrate of 50 ml/min and pulsations of 3.5 cm/s(left), 4.5 cm/s (centre) and 5.5 cm/s (right). 133

Figure 6.6: Time-averaged turbulent dissipation rate distribution in a compartment for a continuous phase flowrate of 100 ml/min and pulsations of 3.5 cm/s(left), 4.5 cm/s (centre) and 5.5 cm/s (right). 134

Figure 6.7: Probability density functions of ε for pulsations of 3.5, 4.5, 5.5 cm/s at continuous phase flowrates of 0 (top-left), 50 (top-right) and 100 (bottom) ml/min 135

List of Tables

Table 3.1: Physico-chemical properties of the liquids employed in the turbulent liquid-liquid dispersions 55

Table 4.1: properties of water and Isane employed in the emulsification experiments .. 77

Table 4.2: Averaged turbulent dissipation rates ε (m^2/s^3) according to correlation (eq. 4.5) and by CFD simulations (water-isane) 82

Table 4.3: Reynolds numbers for Isane continuous-phase experiments (first row) and water continuous-phase experiments (second row) at different rotational speeds of the impeller. 83

Table 4.4: Volume-averaged turbulent dissipation rates ε (m^2/s^3) in the recirculation zone, in the impeller zone and in the total volume for water-phase CFD simulations. 84

Table 4.5: Identified parameters for the Coulaloglou and Tavlarides kernel employing the pdf of ε or assuming a uniform value..... 87

Table 5.1: Properties of Isane 175/Marcol 82 mixtures employed as solvents in the emulsification experiments. 97

Table 5.2: Identified parameters for the "generalized" model. Also the parameters for the "initial" model are reported [22]. 102

Table 5.3: Relative errors according to Eq. (5.7) in the determination of the adjusted parameters at an impeller rotation speed of 600 rpm..... 102

Table 5.4: Relative errors (Eq. 5.7) by fitting the 1-2% water-in-Isane experiments through the "generalized" and "initial" models..... 105

Table 5.5: Kolmogorov microscale (η) and Inertial/Dissipation subranges boundary (l_{DI}) for the Isane/Marcol experiments at different viscosity and turbulent conditions 106

Table 5.6: Relative errors (Eq. 5.7) by fitting the 1% water-in-Isane70%Marcol30% experiments through the "generalized" and "initial" models: 110

Table 5.7: Relative errors (Eq. 5.7) by fitting the 2% water-in-Isane70%Marcol30% experiments through the "generalized" and "initial" models: 110

Table 5.8: Impeller Reynolds numbers at different rotational speeds and viscosities . 111

Table 5.9: Relative errors (Eq. 5.7) by fitting the 1% water-in-Isane55%Marcol45% experiments through the "generalized" and "initial" models: 113

Table 6.1: Physical-chemical properties of the tested phases 118

Table 6.2: Time-averaged value of the turbulent dissipation rate in a compartment of the pulsed column as function of the experimental pulsations and continuous phase flowrates.. 134

Table 6.3: Experimental and simulated Sauter mean diameters and dispersed phase volume fraction considering a dispersed phase flowrate of 50 ml/min, a pulsation of 3.5 cm/s and a continuous phase flowrate equal to zero. 136

Table 6.4: Parameters identified through the *patternsearch* function 137

Table 6.5: Experimental and simulated Sauter mean diameters and dispersed phase volume fraction considering a dispersed phase flowrate of 50 ml/min, pulsations of 4.5 and 5.5 cm/s and a continuous phase flowrate equal to zero. 138

Table 6.6: Experimental and simulated Sauter mean diameters and dispersed phase volume fraction considering a dispersed phase flowrate of 60 ml/min, pulsations of 3.5, 4.5 and 5.5 cm/s and a continuous phase flowrate equal to zero. 139

Table 6.7: Experimental and simulated Sauter mean diameters and dispersed phase volume fraction considering a dispersed phase flowrate of 70 ml/min, pulsations of 3.5, 4.5 and 5.5 cm/s and a continuous phase flowrate equal to zero. 140

Table 6.8: Experimental and simulated Sauter mean diameters and dispersed phase volume fraction considering a dispersed phase flowrate of 50 ml/min, pulsations of 3.5, 4.5 and 5.5 cm/s and a continuous phase flowrate equal to 50 ml/min. 141

Table 6.9: Experimental and simulated Sauter mean diameters and dispersed phase volume fraction considering a dispersed phase flowrate of 50 ml/min, pulsations of 3.5, 4.5 and 5.5 cm/s and a continuous phase flowrate equal to 100 ml/min. 142

1. Introduction

Liquid-liquid extraction is a common unit operation in the chemical, pharmaceutical, food and nuclear industries. It represents a valid alternative to distillation for those processes where the sensitivity to the temperature is important (bio-products), the boiling temperatures of the components to separate are close or the heat required to boil the components is too elevated [1].

In the nuclear industry, the recycling of uranium and plutonium from irradiated fuel rods is achieved through the PUREX process [2]. The heart of this process consists of several liquid-liquid extraction steps that allow the separation of these compounds from the other irradiated fuel components: minor actinides and fission products. The plutonium recycling is moreover dictated by the possibility to produce new fuel to be fed to the nuclear reactors, hence reducing the need for uranium ore extraction.

In the PUREX process, the high concentrated nitric acid liquor, where the spent fuel has been dissolved, is contacted with an organic phase containing Tributyl Phosphate (TBP), an extracting molecule. The process is performed in extraction columns, mixer-settlers and centrifugal extractors. In these contactors, the two phases are mechanically or pneumatically agitated in order to achieve the formation of a liquid-liquid dispersion, which is highly suitable for the phase transfer process thanks to its high interfacial area.

Although the PUREX process, as well as other extraction technologies, are already optimized and running from several decades, new technological challenges require a better understanding of the physics of the separation processes. It is the case of nuclear recycle processes which aim at the extraction of uranium and plutonium without involving REDOX reactions, as for the PUREX process, that lead to the formation hazardous by-products. In order to avoid expensive experiments, the modeling of the hydrodynamic behavior inside the liquid-liquid contactors, which allows to predict some important extraction parameters, is of crucial importance. The aim of this work is to better comprehend the behavior of turbulent liquid-liquid dispersions, in order to model the spatial and time evolution of the interfacial area and the dispersed phase volume fraction.

The design of a liquid-liquid contactor (or its efficiency improvement) is therefore influenced by the possibility of predicting the interfacial area between the two phases according

to the operating conditions. Many semi-empirical equilibrium correlations have been proposed to compute the contact area in the pulsed columns and in the mixer-settlers [3–5]. However, these correlations present the drawbacks of being valid in a narrow range of operating conditions (the experimented ones) and not considering the transient behavior of this property. Furthermore, such correlations predict only a mean droplet size, and not the full distribution.

A step further in the prediction of the time evolution of the contact area can be achieved through the solution of a Population Balance Model (PBM) [6,7]. The PBM (or PBE, Population Balance Equation) is an integral-differential equation which determines the time-evolution of a number density function (NDF), that represents the number concentration of the dispersed population having some properties of interest in a determined interval. In the case of liquid-liquid extraction, the droplet diameter and/or the solute concentration may be considered as internal coordinates. Through these two properties, indeed, the mass-transfer between the continuous and the dispersed phase can be computed.

The PBE is characterized by the presence of source terms that quantify the breakage and coalescence events in the liquid-liquid contactor. Their modeling is of crucial importance, since an accurate solution of the PBE depends on a good prediction of breakage and coalescence rates. The breakage and coalescence kernels are complex functions of the properties of both the continuous and dispersed phases (interfacial tension, densities, viscosities), and of the flow regime in the liquid-liquid extractor. A turbulent flow is generally preferred, since in this regime the mass-transfer is enhanced. Indeed, the turbulent eddies cause droplet breakage by transferring their turbulent kinetic energy to the droplets, which leads to the generation of a greater interfacial area. Besides this, their chaotic motion enhances the solute transfer, since the eddies transport the solute from the droplet to the continuous phase bulk (or *vice versa*), if compared to molecular diffusion mass-transfer processes [1].

The breakage and coalescence kernels used in chemical engineering have been formulated assuming the droplets to be strongly influenced by the eddy behavior in the liquid-liquid contactor [8–15]. Indeed, the droplet breakage is triggered by the pressure and velocity fluctuations caused by eddies of smaller dimensions which arrive on the droplet surface. The breakage event is assumed to depend on the turbulent kinetic energy dissipation rate, ε, which represents the turbulent kinetic energy transferred to the droplet and which allows to compute

the turbulent stresses which lead to droplet instability. These stresses are counterbalanced by the restoring stresses caused by the droplet surface tension and internal viscosity, which tend to keep the droplet in its spherical form. Droplet breakage takes place when the turbulent stresses are high enough to overtake the restoring stresses [16]. As in the case of breakage, also coalescence is influenced by the eddy motion. Indeed, eddies of bigger dimensions transport the droplet in the flow increasing the droplet collision frequency. Droplet coalescence takes place if the inertia at which the droplet is transported, which is expressed through the turbulent dissipation rate, is high enough to drain the continuous phase film that is trapped in between the droplets during the collision.

It is clear that, according to breakage and coalescence mechanisms, turbulence plays a fundamental role in these processes, mainly through the turbulent kinetic dissipation energy rate ε. For this reason, the theory of turbulence is briefly exposed in Chapter 2.

When the first breakage and coalescence kernels were proposed, the turbulent dissipation rate ε was considered uniform in the liquid-liquid contactors. This assumption is far from the real physics in the liquid-liquid contactors, since the ε varies importantly in space, being higher in the proximity of walls or rotating parts [17]. Since in the nuclear recycle industry, accurate hydrodynamic models that facilitate the scale-up from lab-scale to industrial extractors or the transposition from simple to more complex contactors are needed, due to the impossibility (radiotoxicity) to run experiments at large scale, this problem will be investigated.

In order to account for the turbulent inhomogeneities, CFD simulations are performed. Two different approaches are used: i) CFD-PBM coupling [17–19] or, ii) the exploitation of CFD results in a 0D PBM routine. While being the most accurate method, the CFD-PBM coupling requires huge computational resources and time, which is not suitable for industrial applications. The second approach, instead, allows to save computational time, since the performed CFD simulations do not require the solutions of additional equations representing the PBM. Buffo et al. [20] proposed a method based on the probability density function (PDF) of ε, which allows to account for turbulent inhomogeneities in a 0D PBE model. In Chapter 4, this approach will be implemented and validated on turbulent liquid-liquid dispersion experiments performed in a stirred tank reactor.

Besides the assumption of a uniform ε, the breakage and coalescence kernels were developed assuming the droplets to have dimension in the inertial subrange of turbulence. In this subrange, according to the Kolmogorov theory, the statistical properties of eddies are only dependent on the turbulent dissipation rate ε, and not on the viscosity. Although this, in the case of extraction processes performed at high continuous phase viscosities, a non-negligible number of droplets have their size outside the inertial subrange of turbulence. In Chap. 5, a generalization of the breakage and coalescence kernels is proposed, which makes them valid in the entire spectrum of turbulence. The validity of the proposed model was verified on turbulent liquid-liquid experiments carried out at high viscosities, which mimic the physics of the PUREX process.

Finally, the improvements for the breakage and coalescence kernels were implemented in a 1D PBE model of the pulsed column (Chap. 6). This model allows the prediction of the Sauter mean diameters and of the dispersed phase volume fraction in the column. The model was validated through liquid-liquid dispersion experiments performed in a pulsed column at dispersed and continuous flowrates and pulsations.

The manuscript is therefore structured as follows:

In Chapter 2, the typical methodologies used to model poly-dispersed systems are reviewed and analyzed. The turbulence theory is described first, then the second part of this chapter deals with the discussion of the breakage and coalescence kernel.

Chapter 3 presents the experimental and numerical tools implemented in the PhD project to characterize and monitor the droplet size distribution, on one hand, and to assess the turbulence distribution in the considered contactors, on the other hand.

The following chapters are dedicated to the PhD results:

Chapter 4 presents a method which allows to account for turbulent inhomogeneities in a 0D PBE model. It is based on the computation of volume-averaged breakage and coalescence kernels through the probability density function of the turbulent dissipation rate.

Chapter 5 details the derivation of generalized breakage and coalescence kernels which are valid for the entire turbulence spectrum. These models are based on more refined second-order structure function and eddy energy spectrum.

Chapter 6 presents the development of a new pulsed column model, based on the findings of Chap 4 and 5. This hydrodynamic model is based on a two-fluid approach, with the dispersed phase modelled by a PBE.

Finally, the conclusions will show all the possible future development of the work that has been performed during this work.

2. Modeling of polydisperse systems

2.1. General PBE

Multiphase flows are characterized by the presence of two or more phases which exchange momentum, energy and mass [21]. In the case of a liquid-liquid extraction implemented in a pulsed column, one of the phases constitutes a continuous medium (continuous phase), while the second one is dispersed in the form of droplets (dispersed phase). The mass-transfer between the two phases is influenced by some macroscopic properties, as the interfacial area, which depends on the droplet size distribution. The evolution of the droplet population in the liquid-liquid contactor can be predicted through the solution of a Population Balance Equation (PBE).

The PBE is an integro-differential equation based on the number density function (NDF) [6]. The NDF depends on the time t, on the spatial coordinates $\boldsymbol{x}$ (also called external coordinates) and on the internal coordinates $\boldsymbol{\varphi}$, which represent the droplet properties that are relevant to track (due to the interest in the interfacial area, the droplet volume (or diameter) is considered, i.e. $\boldsymbol{\varphi} = v\ (or\ \boldsymbol{\varphi} = d)$). The NDF represents the droplet number concentration in the physical and the internal coordinate spaces. The time and spatial evolution of the NDF (considering the droplet volume as the internal coordinate) can be determined through the PBE model:

$$\frac{\partial n(\boldsymbol{x},v,t)}{\partial t} + \langle u_i \rangle \frac{\partial n(\boldsymbol{x},v,t)}{\partial x_i} - \frac{\partial}{\partial x_i}\left[\left(D_t + D_p\right)\frac{\partial n(\boldsymbol{x},v,t)}{\partial x_i}\right] = \frac{\partial}{\partial v}[n(\boldsymbol{x},v,t)\dot{v}] + s(\boldsymbol{x},v,t) \qquad (2.1)$$

Similarly to other transport equations, the PBE expresses the balance of accumulation, advection and diffusive terms. The velocity $\langle u_i \rangle$ represents the Reynolds-averaged i^{th} component of the dispersed phase velocity that can be computed through a momentum balance. D_t and D_p are the turbulent and molecular diffusivities, respectively. The first term on the right-hand side of the equation represents the PBE growth term. This term considers the physical phenomena that cause a continuous variation of one of the internal properties (volume v) of the droplet population, as evaporation, which leads to the droplet shrinkage, or condensation, which increases the droplet size. Except for the exchange of dilute species in the case of solvent

extraction (which is not considered in this PhD project), negligible mass flux takes place between the two phases, since their reciprocal solubility is low. Therefore, the growth term, which would quantify the increase or decrease of droplet diameter due to mass exchange, is assumed null:

$$\frac{\partial}{\partial v}[n(\boldsymbol{x}, v, t)\dot{v}] = 0$$

The last term of the PBE is the source term, which describes the changes of the NDF caused by discontinuous processes as droplet breakage and coalescence.

The PBE presents some unknowns, as the dispersed phase velocity or the turbulent diffusivity, which may be computed only by solving additional equations. As discussed in the introduction, an approach that has been adopted in the literature is to couple the PBE with CFD. This coupled method allows the solution of the PBM according to the results of the fluid motion obtained through the CFD. Although being the most accurate approach, this method is highly time consuming and demanding in term of computational resources. Therefore, in this work, a simplified PBM is adopted in order to reduce the computational time, based on the assumption of a homogeneous NDF. This assumption is valid when the dispersed phase volume fraction is low. As stated by Marchisio and Fox [6], breakage and coalescence events tend to create spatial inhomogeneity of the NDF, while the droplet diffusivity leads to the homogenization of this function. The breakage and coalescence characteristic times both depend on the dispersed phase volume fraction. The higher the volume fraction, the higher the frequency of breakage and coalescence events. Indeed, a higher dispersed phase volume fraction leads to a higher number of droplets, increasing the droplet collision frequency and therefore the aggregation rate. An important aggregation rate leads to the formation of bigger droplets, that are more likely to break and, finally, to a higher breakage rate. Therefore, concentrated dispersed phases will be characterized by a strong inhomogeneity. In the case of a dilute system, on the contrary, aggregation and breakage rates are low. For these systems, the homogenizing effect due to diffusion is prevailing, leading to an NDF that can be assumed homogeneous. In this PhD project, **low dispersed phase volume fractions are studied**. Hence, a homogeneous NDF is assumed and defined as:

$$\tilde{n}(t,v) = \frac{1}{V}\int_V n(t,\boldsymbol{x},v)\,d\boldsymbol{x} \tag{2.2}$$

By substituting the homogeneous number density function (Eq. 2.2) and by applying a volume-averaged procedure [18,22] to the PBM (Eq. 2.1), the following equation is obtained:

$$\frac{\partial \tilde{n}(t,v)}{\partial t} = \frac{1}{V}\int_V s(\boldsymbol{x},t,v)\,d\boldsymbol{x} \tag{2.3}$$

It is of fundamental importance to remark that, although considering a homogeneous NDF, the source term depends on the spatial coordinates, since breakage and coalescence kernels depends on the turbulent properties, which are function of space. Rendering explicit the source term, the 0D PBE model reads:

$$\begin{aligned}\frac{\partial \bar{n}(v,t)}{\partial t} = &\int_v^{\infty} p(v')\beta(v|v')\frac{1}{V}\int_{\boldsymbol{x}}\Gamma(\boldsymbol{x},v)d\boldsymbol{x}\,\bar{n}(v',t)dv' \\ &- \bar{n}(v,t)\int_0^{\infty}\frac{1}{V}\int_{\boldsymbol{x}} \mathrm{Q}(\boldsymbol{x},v,v')d\boldsymbol{x}\,\bar{n}(v',t)\,dv' \\ -\bar{n}(v,t)\frac{1}{V}\int_{\boldsymbol{x}}\Gamma(\boldsymbol{x},v)d\boldsymbol{x} &+ \frac{1}{2}\int_0^{v}\frac{1}{V}\int_{\boldsymbol{x}}\mathrm{Q}(\boldsymbol{x},v-v',v')d\boldsymbol{x}\,\bar{n}(v-v',t)\bar{n}(v',t)dv'\end{aligned} \tag{2.4}$$

The first source term represents the birth of droplets due to breakage of bigger ones. This term is characterized by $p(v')$, which represents the number of fragments deriving from the breakage of a mother droplet. In this work, **binary breakage will be assumed** (*i.e.* formation of 2 daughter droplets). $\beta(v|v')$, the daughter distribution function (DDF), represents the probability that a mother droplet of volume v gives birth to a daughter droplet of volume v' (and consecutively to a droplet of volume $v-v'$). $\Gamma(\boldsymbol{x},v')$ represents the breakage frequency, which gives the breakage rate of a droplet of volume v'. The kernel is function of the continuous and dispersed phase properties and of the flow stresses, which strongly depend on the flow regime (laminar, turbulent). The second source term quantifies the number of droplets of volume v which disappears due to breakage. The third source term represents the number of droplets of volume v generated due to the coalescence of smaller droplets. It is characterized

by the coalescence kernel $Q(\boldsymbol{x}, v - v', v')$, which gives the coalescence rate of two droplet classes of volume $v - v'$ and v'. Finally, the last source term indicates the number of droplets of volume v' which disappear due to coalescence with other droplets.

2.2. Solving the 0D PBE

As it is very rare to have an analytical solution of the population balance equations, three different numerical methods have been proposed for solving population balance equations:

- **The discretization (class) methods** [23–30] are based on the discretization of the internal coordinate of the PBE in order to obtain a set of macroscopic balance equations to be solved as a single differential equation in each discretized size-interval.
- **The Methods of Moments** [31–36], which consider the properties of the DSD (its first moments) rather than the DSD itself. The moments methods consider as many equations as moments (usually 6). They are hence more convient for coupling with CFD simulations requiring the population balance equation to be solved in each grid cell .
- **The stochastic Monte Carlo methods** [37–40]**,** which although being more and more considered for the derivation of breakage/coalescence probability models, they are not appropriate for the simulation of real processes.

In this work, the Fixed Pivot Method, a popular class method, was employed in the solution of the PBE. In the following subsections, the principal class methods (Fixed Pivot Method, Cell Average Technique, Finite Volume Method) and the Quadrature Method Of Moment are detailed.

2.2.1.1. The Fixed Pivot Method

The Fixed Pivot Method (FPM) is a class method developed by Kumar and Ramkrishna [24,28]. Considering v, the droplet volume, as the internal variable, the FPM requires the discretization of the internal coordinate domain into N $[v_i, v_{i+1}]$ intervals. In this method, it is assumed that the droplets whose dimension is in the interval $[v_i, v_{i+1}]$, have volume equal to the pivot of the interval x_i, defined as $v_i < x_i < v_{i+1}$. Due to this assumption, the number density function is expressed as:

$$n(v,t) = \sum_{k=1}^{M} N_k(t)\delta(v - x_k) \tag{2.5}$$

The FPM is based on the integration of the PBE in each interval $[v_i, v_{i+1}]$ of the discretization:

$$\begin{aligned}\frac{dN_i(t)}{dt} = \frac{1}{2}\int_{v_i}^{v_{i+1}} \left(\int_0^v n(v-v')n(v',t)Q(v-v',v')dv' \right) dv \\ - \int_{v_i}^{v_{i+1}} n(v,t) \left(\int_0^{\infty} n(v',t)Q(v,v')dv' \right) dv \\ + \int_{v_i}^{v_{i+1}} \left(\int_v^{\infty} \beta(v,v')n(v',t)\Gamma(v')dv' \right) dv - \int_{v_i}^{v_{i+1}} \Gamma(v)n(v,t)\, dv\end{aligned} \tag{2.6}$$

This class method allows the preservation of all the droplet population moments. While this is always true for an arithmetic grid, problems arise when a geometric grid is employed. If we consider the coalescence of two droplets of volume x_i and x_{i+1} (being for definition two pivots of the discretization), the resulting droplet would have a volume $x_i + x_{i+1}$ that, in a geometric grid, could not be a pivot, leading to a problem of attribution. In order to achieve the volume conservation, a repartition of the generated volume after a breakage or a coalescence event among the nearest pivots is done. The number of moments that it is possible to preserve is equal to the number of confining pivots employed for the redistribution. In the case of two preserved moments:

$$\begin{aligned} a{x_i}^k + b{x_{i+1}}^k = v^k \\ a{x_i}^j + b{x_{i+1}}^j = v^j \end{aligned} \tag{2.7}$$

Kumar and Ramkrishna considered the conservation of the zeroth (total number of droplets) and the first (total volume) moments of the distribution (considering the droplet volume as the internal coordinate), with:

$$a = \frac{x_{i+1} - v}{x_{i+1} - x_i}$$
$$b = \frac{v - x_i}{x_{i+1} - x_i} \tag{2.8}$$

Additionally, if more than 2 moments have to be preserved, more equations could be added to the system of Eqs. 2.7. Hence, to preserve 4 moments [41]:

$$a{x_{i-1}}^k + b{x_i}^k + c{x_{i+1}}^k + d{x_{i+2}}^k = v^k$$
$$a{x_{i-1}}^j + b{x_i}^j + c{x_{i+1}}^j + d{x_{i+2}}^j = v^j$$
$$a{x_{i-1}}^l + b{x_i}^l + c{x_{i+1}}^l + d{x_{i+2}}^l = v^l$$
$$a{x_{i-1}}^m + b{x_i}^m + c{x_{i+1}}^m + d{x_{i+2}}^m = v^m$$

Once the number of moments to be preserved is decided, it is possible to derive the numerical method that solves the PBM.

The birth term due to breakage in the PBE is expressed as:

$$R_{Bb} = \int_{v_i}^{v_{i+1}} \left(\int_v^{\infty} \beta(v,v') n(v',t) \Gamma(v') dv' \right) \tag{2.9}$$

according to Eq. 2.7, Eq. 2.9 rewrites:

$$R_{Bb} = \int_{x_i}^{x_{i+1}} a(v,x_i) \left(\int_v^{\infty} \beta(v,v') n(v',t) \Gamma(v') dv' \right) dv + \int_{x_{i-1}}^{x_i} b(v,x_i) \left(\int_v^{\infty} \beta(v,v') n(v',t) \Gamma(v') dv' \right) dv \tag{2.10}$$

by substituiting Eq. 2.5 in Eq. 2.10, the birth term reads:

$$R_{Bb} = \sum_{x_i}^{x_{i+1}} n_{i,k}\, \Gamma_k N_k(t) \tag{2.11}$$

where:

$$n_{i,k} = \int_{x_i}^{x_{i+1}} \frac{x_{i+1} - v}{x_{i+1} - x_i} \beta(v, x_k) dv + \int_{x_{i-1}}^{x_i} \frac{v - x_{i-1}}{x_i - x_{i-1}} \beta(v, x_k) dv \tag{2.12}$$

Accordingly, Kumar et Ramkrishna derived the other terms of the PBE:

$$R_{Db} = \Gamma_i N_i(t)$$

$$R_{Ab} = \sum_{\substack{j,k \\ x_{i-1} \le (x_j + x_k) \le x_{i+1}}}^{j \ge k} \left(1 - \frac{1}{2}\delta_{j,k}\right) \eta\, Q_{j,k} N_j(t) N_k(t) \tag{2.13}$$

$$R_{Da} = N_i(t) \sum_{k=1}^{M} Q_{i,k} N_k(t)$$

where η:

$$\eta = \begin{cases} \dfrac{x_{i+1} - v}{x_{i+1} - x_i} & x_i \le v \le x_{i+1} \\ \dfrac{v - x_{i-1}}{x_i - x_{i-1}} & x_{i-1} \le v \le x_i \end{cases}$$

Finally, the discretized form of Eq. 2.6 reads:

$$\frac{dN_i(t)}{dt} = \sum_{\substack{j,k \\ x_{i-1} \le (x_j + x_k) \le x_{i+1}}}^{j \ge k} \left(1 - \frac{1}{2}\delta_{j,k}\right) \eta\, Q_{j,k} N_j(t) N_k(t) - \Gamma_i N_i(t) \tag{2.14}$$

$$-N_i(t)\sum_{k=1}^{M} Q_{i,k}N_k(t) + \sum_{x_i}^{x_{i+1}} n_{i,k}\,\Gamma_k N_k(t)$$

The Fixed Pivot Method was retained in this study to solve and inverse the PBE, as it is relatively easy to program, robust and with low computation time. The FPM is combined with arithmetic grids (see Sec. 4.3).

2.2.1.2. The Cell Average Technique

The cell average technique (CAT) is a class method developed by Kumar et al. [30], with the aim of reducing possible overprediction of the number density function by employing the FPM. As in the previous case, the CAT is based on the discretization of the internal coordinate v and the integration of the population balance balance equation in each interval of center $[v_i, v_{i+1}]$. It is moreover assumed that the droplets with dimensions in the interval $[v_i, v_{i+1}]$ are concentrated in the cell center x_i.

The major difference between the FPM and CAT lies in the way this redistribution is carried out. Whereas in the FPM each newborn droplet is redistributed to the pivots with the closest volumes, in the CAT, the average volume of the newborn droplets is computed and then redistributed to the nearest pivots. The final formulation of the PBE according to the CAT is:

$$\frac{dN_i}{dt} = B^{CA}_{agg+break,i} - D^{CA}_{agg+break,i} \tag{2.15}$$

where:

$$\begin{aligned} B^{CA}_{agg+break,i} &= B_{agg+break,i-1}\lambda_i^-(\bar{v}_{i-1})H(\bar{v}_{i-1} - x_{i-1}) \\ &+ B_{agg+break,i}\lambda_i^+(\bar{v}_i)H(\bar{v}_i - x_i) + B_{agg+break,i}\lambda_i^-(\bar{v}_i)H(x_i - \bar{v}_i) \\ &+ B_{agg+break,i+1}\lambda_i^+(\bar{v}_{i+1})H(x_{i+1} - \bar{v}_{i+1}) \end{aligned} \tag{2.16}$$

$$D^{CA}_{agg+break,i} = D_{agg,i} + D_{break,i}$$

The final expressions to calculate birth and death terms due to breakage or coalescence are:

$$
\begin{aligned}
D_{break,i} &= \Gamma_i N_i(t) \\
B_{agg,i} &= \sum_{\substack{j,k \\ x_{i-1} \le (x_j + x_k) \le x_{i+1}}}^{j \ge k} Q_{j,k} N_j(t) N_k(t) \\
D_{agg,i} &= N_i(t) \sum_{k=1}^{M} Q_{i,k} N_k(t) \\
B_{break,i} &= \sum_{k \ge i} N_k(t) S_k \int_{x_{i-\frac{1}{2}}}^{p_k^i} b(t, x, x_k) dx
\end{aligned}
\tag{2.17}
$$

The average volume of the newborn particles in a cell is computed as:

$$
\bar{v}_i = \frac{V_{agg,i} + V_{break,i}}{B_{agg,i} + B_{break,i}}
$$

where :

$$
\begin{aligned}
V_{break,i} &= \sum_{k \ge i} N_k(t) \Gamma_k \int_{v_{i-\frac{1}{2}}}^{p_k^i} v \beta(t, v', v_k) dv \\
V_{agg,i} &= \sum_{\substack{j,k \\ v_{i-\frac{1}{2}} \le (v_j + v_k) \le v_{i+\frac{1}{2}}}}^{j \ge k} \left(1 - \frac{1}{2}\delta_{j,k}\right) Q_{j,k} N_j(t) N_k(t) (v_j + v_k)
\end{aligned}
\tag{2.18}
$$

2.2.1.3. The Finite Volume method

The Finite Volume method (FVM) is a class method initially formulated for coalescence problems by Filbet and Laurencot [29] and later adapted to breakage by Kumar et al. [42]. As

in the case of the previous two methods, the FVM is based on the discretization of the internal coordinate v in intervals $[v_i, v_{i+1}]$. However, while the FPM and the CAT require a redistribution of the newborn particles according to the cell center or the pivots of the grid, the FVM defines the mass fluxes of the droplets entering or leaving a given interval. According to the authors, the Population Balance Equation can be re-formulated as follows:

$$\frac{d(vn(v,t))}{dt} = \frac{dJ_{coal}(n,v)}{dv} + \frac{dJ_{break}(n,v)}{dv} \tag{2.19}$$

where:

$$\begin{aligned} J_{coal}(n,v) &= \int_0^v \left(\int_{v-u}^{\infty} uQ(u,v')n(v,t)n(u,t)dv' \right) du \\ J_{break}(n,v) &= \int_v^{\infty} \left(\int_0^v u\beta(u,v')S(v')n(v')du \right) dv' \end{aligned} \tag{2.20}$$

Defining $g = vn$, the final formulation of the FVM leads to:

$$g_i^{n+1} = g_i^n - \frac{\Delta t}{\Delta x_i}\left(J^{h,m}_{break+coal,i+1} - J^{h,m}_{break+coal,i-1}\right) \tag{2.21}$$

where:

$$\begin{aligned} J^{h,m}_{coal,i+1} &= \sum_{k=0}^{i} \Delta x_k g_k^m \left\{ \sum_{j=\alpha_{i,k}}^{M} \int_{v_j}^{v_{j+1}} \frac{Q(v',v_k)}{v'} dv' \, g_j^m + \int_{v_{i+1}-v_k}^{v_{\alpha_{i,k}-1}} \frac{Q(v',v_k)}{v'} dv' \, g^m_{\alpha_{i,k}-1} \right\} \\ J^{h,m}_{break,i+\frac{1}{2}} &= -\sum_{k=i+1}^{M} g_k^m \int_k^{k+1} \frac{S(v')}{v'} dv' \int_0^{v_{i+1}} u\beta(u,v_k)du \end{aligned} \tag{2.22}$$

2.2.1.4. Quadrature Method Of Moment (QMOM)

The QMOM differs from the previous numerical methods since it solves a set of equations for the moments of the number density function [6,31,32]. The advantage of this method resides in the lower number of equations that must be solved if compared to a class method. Although this, the QMOM does not provide directly the number density function, giving instead access to some properties of interest as the Sauter mean diameter. When the DSD is required, a reconstruction method must be applied using the computed moments [6]. However, the reconstruction methods can be rather inaccurate, especially as non mono-modal populations are concerned.

Considering a number density function whose internal coordinate is the droplet diameter, it is possible to compute the k^{th}-order moment of the distribution as:

$$m_k = \int_0^\infty d^k n(d) dd \tag{2.23}$$

by applying the integration of Eq. 2.23 to the PBE, the following equation is obtained:

$$\begin{aligned}\frac{dm_k}{dt} = \frac{1}{2}\int_0^\infty n(d)\int_0^\infty Q(d,\lambda)(d^3+\lambda^3)^{\frac{k}{3}} n(\lambda) d\lambda dd \\ - \int_0^\infty d^k n(d)\int_0^\infty Q(d,\lambda) n(\lambda) d\lambda dd \\ + \int_0^\infty d^k \int_0^\infty S(\lambda)\beta(d|\lambda) n(\lambda) d\lambda dd - \int_0^\infty d^k S(d) n(d) dd\end{aligned} \tag{2.24}$$

The QMOM is based on the approximation of the k^{th}-order moment through a quadrature approximation:

$$m_k = \int_0^\infty d^k n(d) dd = \sum_{i=1}^{N} w_i d_i \tag{2.25}$$

where w_i are the weights and $L_i$the abscissas. Indeed, in the QMOM the moments of the distribution are approximated through a fictitious population of N classes, each class having a weight w and being concentrated in the abscissa L.

By substituting Eq. 2.25 in Eq. 2.24 and rearranging, the final equation is obtained:

$$\frac{dm_k}{dt} = \frac{1}{2}\sum_i w_i \sum_j w_j \left({d_i}^3 + {d_j}^3\right)^{\frac{k}{3}} Q_{i,j} - \sum_i {d_i}^k w_i \sum_j Q_{i,j} w_j + \sum_i \Gamma_i \overline{\beta_i^{(k)}} w_i - \sum_i d_i^k \Gamma_i w_i \qquad (2.26)$$

where:

$$\overline{\beta_i^{(k)}} = \int_0^\infty d^k \beta(d|d_i) dd$$

In order to solve Eq. 2.26, the knowledge of the weights w_i and the abscissas L_i is needed. These values can be obtained through the Product-Difference (PD) algorithm [6], which allows their determination by minimizing the error in approximating the k^{th}-order moment. The PD algorithm is based on the construction of the M matrix, whose components will be identified as $M_{i,j}$. The latter can be computed as follows:

$$\begin{aligned} P_{i,1} &= \delta_{i,1} && i \in 1, \dots, 2N_q + 1 \\ P_{i,2} &= (-1)^{i-1} m_{i-1} && i \in 1, \dots, 2N_q + 1 \\ & && j \in 3, \dots, 2N_q + 1 \\ P_{i,j} &= P_{1,j-1} P_{i+1,j-2} - P_{1,j-2} P_{i+1,j-1} && \\ & && i \in 1, \dots, 2N_q + 2 - j \end{aligned} \qquad (2.27)$$

where N_q represents the number of the quadrature points employed in the moment approximations. The quadrature approximation is true until the moment of order $2N_q$.For this

reason, if the interest lies in the first N moments, an exact quadrature can be obtained through $N_q = \frac{N}{2}$ quadrature points.

Once the M matrix has been constructed, a second matrix, R, can be computed from the components of M which allow the determination of the weights w_i and the abscissas L_i. The R matrix is tridiagonal, where the elements on the diagonal are represented by a_i and the elements on the codiagonals by b_i. These elements can be computed once a set of coefficients α_i is determined ($\alpha_1 = 0$):

$$\alpha_i = \frac{P_{1,i+1}}{P_{1,i}P_{1,i-1}} \qquad i \in 2, \dots, 2N_q \tag{2.28}$$

Consecutively, the coefficients of the R matrix are:

$$\begin{aligned} a_i &= \alpha_{2i} + \alpha_{2i-1} && i \in 1, \dots, 2N_q - 1 \\ b_i &= -\sqrt{\alpha_{2i+1} + \alpha_{2i-1}} && i \in 2, \dots, 2N_q - 2 \end{aligned} \tag{2.29}$$

Finally, the eigenvalues of the R matrix represent the abscissas L_i, while the first value of each eigenvector stands for the weights w_i. By substituting the abscissas and the weights in Eq. 2.26, the solution of the moment transport equations can be obtained.

2.3. Turbulence theory

In order to obtain an accurate solution of PBM, the knowledge of the breakage and coalescence kernel is of crucial importance. To better understand how these models were formulated, the theory of turbulence is introduced.

A fully developed turbulent flow is characterized by the presence of eddies, which are local swirls of fluid with a characteristic dimension l and velocity u. The eddies generate when

the viscosity of the fluid is not anymore capable to dampen the instabilities that arise in a flow with an important inertia (i.e., at high Reynolds number) [43,44].

Eddies can have very different sizes. Indeed, the biggest ones have dimensions of the same order of magnitude of the characteristic flow length scale (L), while the smallest ones many orders less. According to Richardson [45], bigger eddies, which are highly energetic and unstable, break and transmit their energy to smaller ones. This phenomenon repeats at smaller and smaller scales until the smallest eddies and their related energy are dissipated by viscosity. Therefore, a turbulent flow is characterized by a cascade of energy from bigger scales to smaller ones.

Starting from Richardson's view of turbulent flows, Kolmogorov developed a turbulence theory that is widely assumed in breakage and coalescence kernel formulation. The Kolmogorov theory is based on three hypothesis [45]. Firstly, Kolmogorov assumed that in a fully developed turbulent flow, the small-scales eddies ($l \ll L$) are statistically isotropic (hypothesis of local isotropy). This means that the information on the flow geometry, which causes the anisotropy of the biggest eddies, is lost at small scales. Therefore, Kolmogorov postulated the existence of a universal subrange of turbulence where the eddy properties are not influenced by the process geometry. Indeed, for any turbulent flow, at small scales, the eddies behave in the same way. Then, Kolmogorov postulated two hypothesis of similarity: the first hypothesis states that for every fully-developed turbulent flow, the statistics of the small scale eddies ($l \ll L$) depend only on the turbulent kinetic dissipation energy rate ε and on the kinematic viscosity of the fluid, ν. ε represents the amount of turbulent kinetic energy which is transferred in the energy cascade from a scale to a smaller one. According to this hypothesis, it is possible to define the smallest size of an eddy, η, in a fully developed turbulent flow:

$$\eta = \left(\frac{\nu^3}{\varepsilon}\right)^{\frac{1}{4}} \tag{2.30}$$

Once an eddy reaches the Kolmogorov microscale η, it is dissipated by the viscosity. The second similarity hypothesis states that for scales much smaller than the characteristic flow length ($l \ll L$) but much bigger than the Kolmogorov microscale ($l \gg \eta$), the statistics of these

scales depend only on the turbulent kinetic energy dissipation rate ε. This subrange of turbulence, characterized by $\eta \ll l \ll L$, is defined as the inertial subrange of turbulence.

Thanks to the Kolmogorov theory, important properties of the turbulent flow can be obtained. Indeed, through the second similarity hypothesis, it is possible to define by dimensional analysis, the energy spectrum of eddies in the inertial subrange:

$$E(\kappa) = C_K \varepsilon^{\frac{2}{3}} \kappa^{-\frac{5}{3}} \tag{2.31}$$

where C_K is the Kolmogorov constant (≈ 1.5) and κ represents the eddy wavelength:

$$\kappa = \frac{2\pi}{l}$$

According to Kolmogorov, the turbulent kinetic energy per unit mass of fluid of the eddies with wavelength κ between $[\kappa, \kappa + \Delta\kappa]$ can be computed as:

$$k_{\kappa,\kappa+\Delta\kappa} = \int_{\kappa}^{\kappa+\Delta\kappa} C_K \varepsilon^{\frac{2}{3}} \kappa^{-\frac{5}{3}} d\kappa$$

It is fundamental to remark that this expression of the energy spectrum is not valid for length scales of the same magnitude as the characteristic flow length (*i.e.* where anisotropy is important) or as the Kolmogorov microscale (where the effect of viscosity is not negligible, i.e., the dissipation subrange).

An important statistical property that can be defined through the Kolmogorov theory in the inertial subrange of turbulence is the second-order structure function, $\langle [\Delta u(l)]^2 \rangle$. This function represents the mean relative square velocity between two points distant l in a fully turbulent flow. Again, by dimensional analysis, Kolmogorov expressed this quantity as:

$$\langle [\Delta u(l)]^2 \rangle = C_K \varepsilon^{\frac{2}{3}} l^{\frac{2}{3}} \tag{2.32}$$

The second-order structure function allows to define the turbulent stresses applied by the eddies on the droplets in the kernel formulations. It depends on the turbulent dissipation rate ε, which itself is function of the spatial coordinates of the flow. Indeed, ε assumes higher values in the proximity of rotating parts or walls. Therefore, the knowledge of the ε distribution in the space permits a more accurate computation of $\langle[\Delta u(l)]^2\rangle$. It is important to remark that the assumption of a homogeneous number density function in the liquid-liquid contactor does not imply that ε, and consecutively the second-order structure function, does not depend anymore on spatial coordinates. Therefore, also in a 0D PBE model, the ε distribution is of valuable importance in the breakage and coalescence kernel computation.

2.4. Breakage kernels

A liquid-liquid dispersion is characterized by the motion of the continuous and dispersed phases. In a turbulent flow, the droplets are subjected to the disruptive stresses generated by the eddy velocity and pressure fluctuations. These stresses are counterbalanced by restoring stresses, which are caused by the droplet surface tension and viscosity, which tend to restore the original spherical shape of the droplet. Obviously, if the external stresses are more important than the restoring ones, the droplet will break. The breakage models that are discussed in the next section are based on these principles.

2.4.1. Coulaloglou and Tavlarides

Coulaloglou and Tavlarides [10] formulated a model that computes the droplet breakage rate in a fully-developed turbulent flow. It was assumed that the droplets have dimensions d in the inertial subrange of turbulence ($\eta \ll d \ll L$, where L is the characteristic flow length). They started by expressing Γ(d), the breakage frequency of a droplet of diameter d, as:

$$\Gamma(d) = \frac{1}{t_b}\frac{N_{break}(d)}{N_{tot}(d)} \tag{2.33}$$

where t_b is the breakage time, and the fraction of breaking droplets depends on the collisions between eddies and droplets. Indeed, Coulaloglou and Tavlarides assumed that a

droplet breaks when the turbulent kinetic energy transmitted by turbulent eddies, of equal or smaller size than the droplet, is higher than the droplet surface energy of the droplets.:

$$E_{kinetic,eddy(d)} > E_{surface,drop(d)}$$

Therefore, by analogy with the kinetic theory of gases and by assuming random motion of the eddies (*i.e.* a normal distribution of kinetic energy), this fraction is:

$$\frac{N_{break}(d)}{N_{tot}(d)} = e^{-\frac{E_{surface,drop(d)}}{E_{kinetic,eddy(d)}}} \tag{2.34}$$

The latter energies are expressed as:

$$E_{surface,drop(d)} = k_1 \sigma d^2$$

$$E_{kinetic,eddy(d)} = k_2 \rho_d d^3 \langle [\Delta u(d)]^2 \rangle$$

where σ and ρ_d are the surface tension and the dispersed phase density respectively.

Coulaloglou and Tavlarides assumed that the droplet breakage time is proportional to the time needed by two contacting lumps of fluid in a turbulent flow to get at a distance d. Assuming the droplet size to be in the inertial subrange of turbulence, the breakage time is expressed as [46]:

$$t_b = c_1 \varepsilon^{-\frac{1}{3}} d^{\frac{2}{3}} \tag{2.35}$$

Finally, the breakage frequency reads:

$$\Gamma(d) = c_1 \varepsilon^{\frac{1}{3}} d^{-\frac{2}{3}} exp\left(- \frac{c_2 \sigma}{\rho_d \varepsilon^{\frac{2}{3}} d^{\frac{5}{3}}} \right) \tag{2.36}$$

where c_1 and c_2 are tuning parameters that the authors obtained by fitting to experimental data.

This breakage frequency needs to be combined with a daughter size distribution that defines the sizes of the two daughter droplets (see Section 2.4.5).

2.4.2. The Alopaeus model

Narsimhan and Gupta [8] represented the interaction between the eddy and the droplet by a Poisson process, thus obtaining the following kernel:

$$\Gamma(d) = c_5 erfc\left(\sqrt{\frac{\sigma}{\rho_c}\frac{c_6}{\varepsilon^{\frac{1}{3}}d^{\frac{5}{6}}}}\right) \tag{2.37}$$

Narsimhan and Gupta assumed that c_5, which is the number of eddies hitting the droplet per unit time, does not depend on the droplet diameter and the turbulence intensity. Alopaeus et al. [8] improved the above kernel by asserting that this parameter is proportional to the turbulent kinetic energy dissipation rate: $c_5\ \alpha\ \varepsilon^{\frac{1}{3}}$. Moreover, the authors considered the viscous stresses that counterbalance the turbulent stresses applied by the eddies:

$$E_{kinetic,eddy(d)} > E_{surface,drop(d)} + E_{viscous,drop(d)}$$

which leads to:

$$c_4\rho d^3\langle[\Delta u(d)]^2\rangle > c_5\sigma d^2 + c_6\sqrt{\frac{\rho_c}{\rho_d}}\mu_d\varepsilon^{\frac{1}{3}}d^{\frac{7}{3}} \tag{2.38}$$

where ρ_c is the contiuous phase density, and ρ_d and μ_d are the dispersed phase density and viscosity respectively. As in the case of the Coulaloglou and Tavlarides kernels, a fully turbulent flow is considered and the droplets assumed to have dimension in the inertial subrange of turbulence. Finally, the breakage frequency reads:

$$\Gamma(d) = c_7\, \varepsilon^{\frac{1}{3}} erfc\left(\sqrt{c_8 \frac{\sigma}{\rho_c \varepsilon^{\frac{2}{3}} d^{\frac{5}{3}}} + c_9 \frac{\mu_d}{\sqrt{\rho_c \rho_d}\, \varepsilon^{\frac{1}{3}} d^{\frac{4}{3}}}}\right) \tag{2.39}$$

where c_7, c_8 and c_9 are tuning parameters of the kernel. Similarly, this breakage frequency needs to be combined with a daughter size distribution.

2.4.3. The Luo and Svendsen model

Luo and Svendsen [9] proposed a kernel that does not require any adjustable parameters (except a guess of the integration limits) and that combines the breakage frequency with the daughter size distribution function in a single expression. The kernel is based on the following hypothesis:

- Turbulence is assumed to be isotropic.
- No additional daughter size distribution function is needed as it is computed directly in the kernel. It is assumed that the velocity and pressure fluctuations induce the droplet breakage. Viscous restoring stresses are considered negligible, since it was initially proposed for bubble breakage.
- The volume fraction of the newborn daughter droplet is a stochastic variable, in agreement with the observation of Hesketh [47], who reported that this fraction is not related to the dimension of the mother droplet.
- The authors, according to Narsimhan and Gupta, postulated that the droplet oscillation frequency is much higher than the eddies arrival frequency. This means that if an eddy with sufficient energy approaches the particle surface, an instantaneous breakage event is produced.
- Breakage is caused by the eddies of smaller dimensions than the droplet, while bigger eddies will just transport it.

Luo and Svendsen considered the breakage rate of a droplet of volume v into two daughter droplets of volume $vf_{BV,}$ and $v(1-f_{BV})$ to be function of the eddy-droplet collision frequency

$\dot{\omega}$ and the probability P_B that the hitting eddy had a kinetic energy higher than the droplet surface energy:

$$\Gamma(v{:}vf_{BV}) = \int_{\lambda_{min}}^{d} P_B(v{:}vf_{BV},\lambda)\dot{\omega}_{B,\lambda}(v)d\lambda \tag{2.40}$$

where f_{BV} is the breakage volume fraction ($0 < f_{BV} < 1$) and λ is the eddy size.

In Eq. 2.40, the upper integration limit is the dimension of the mother droplet, while the lower one represents the minimum size of eddies which can cause breakage.

By analogy with the kinetic theory of gas, the eddy-droplet collision frequency can be expressed as:

$$\dot{\omega}_{B,\lambda}(d) = \frac{\pi}{4}(d+\lambda)^2\sqrt{\langle[\Delta u(d)]^2\rangle}\dot{n}_\lambda n \tag{2.41}$$

where the velocity of an eddy in a turbulent flow is approximated as $\sqrt{\langle[\Delta u(d)]^2\rangle} = \beta(\varepsilon d)^{\frac{2}{3}}$, n is the number of droplets and $\dot{n}_\lambda$ is the number of eddies with dimension equal or lower than d given by:

$$\dot{n}_\lambda = \frac{0.822(1-\phi_d)}{\lambda^4}$$

leading to :

$$\dot{\omega}_{B,\lambda}(d) = \dot{\omega}_{B,\xi}(\xi) = 0.822(1-\phi_d)n(\varepsilon d)^{\frac{1}{3}}\frac{(1+\xi)^2}{d^2\xi^{\frac{11}{3}}} \tag{2.42}$$

where $\xi = \lambda/d$.

The breakage probability is function of the ratio of the increase in surface energy due to breakage event of f_{BV} to the mean kinetic energy of an eddy, in a similar way as the Coulaloglou and Tavlarides kernel:

$$P_B = \exp\left(-\frac{12c_f\sigma}{\beta\rho\varepsilon^{\frac{2}{3}}d^{\frac{5}{3}}\xi^{\frac{11}{3}}}\right) \tag{2.43}$$

where $\beta = \frac{6}{5}\text{gamma}\left(\frac{1}{3}\right)$, and cf is the increase coefficient of surface area:

$$cf = {f_{BV}}^{\frac{2}{3}} + \left(1 - {f_{BV}}^{\frac{2}{3}}\right) - 1 \tag{2.44}$$

Finally the Luo and Svendsen kernel reads:

$$\frac{\Gamma(v{:}vf_{BV})}{(1-\phi)n} = c_4\left(\frac{\varepsilon}{d^2}\right)^{\frac{1}{3}}\int_{\xi_{min}}^{1}\frac{(1+\xi)^2}{\xi^{\frac{11}{3}}}\exp\left(-\frac{12c_f\sigma}{\beta\rho_c\varepsilon^{\frac{2}{3}}d^{\frac{5}{3}}\xi^{\frac{11}{3}}}\right)d\xi \tag{2.45}$$

Note first that this kernel gives directly the breakage frequence as well as the sizes of the daughter droplets. Integrating Eq. 2.45 in the entire domain of. the volume fraction of daughter droplets leads to the following expression of the breakage rate of a droplet of volume v:

$$\Gamma(v) = \frac{1}{2}\int_0^1 \Gamma(v{:}vf_{BV})df_{BV} \tag{2.46}$$

2.4.4. The Baldyga and Podgorska model

Baldyga and Podgorska [48] proposed a kernel which accounts for the intermittency of turbulence. The Kolmogorov theory states that, at high Reynolds number, the flow properties are uniquely determined by the turbulent kinetic energy dissipation rate, ε, which has a constant value. This is not true, especially at very high Reynolds numbers, where ε shows important

fluctuations with respect to the mean time value. Based on the intermittent turbulence theory, Baldyga and Podgorska proposed the following breakage kernel:

$$\Gamma(d) = C_g \sqrt{ln\left(\frac{L}{d}\right)} \langle\varepsilon\rangle^{\frac{1}{3}} d^{-\frac{2}{3}} \int_{\alpha_{min}}^{\alpha} \left(\frac{d}{L}\right)^{\frac{[\alpha+2-3f(\alpha)]}{3}} d\alpha \tag{2.47}$$

where α_{min} and C_g are adjustable parameters and α, the scaling multifractal exponent, reads:

$$\alpha = n\left\{2\left[\frac{B_\mu C_x^{\frac{5}{3}} \mu_d}{\rho_c \langle\varepsilon\rangle^{\frac{1}{3}} L^{\frac{1}{3}} d} + \sqrt{\left(\frac{B_\mu C_x^{\frac{5}{3}} \mu_d}{\rho_c \langle\varepsilon\rangle^{\frac{1}{3}} L^{\frac{1}{3}} d}\right)^2 + \frac{4C_x^{\frac{5}{3}} \sigma}{\rho_c \langle\varepsilon\rangle^{\frac{2}{3}} L^{\frac{2}{3}} d}}\right]^{-1} - \frac{L}{d}\right\} \tag{2.48}$$

where C_x, and B_μ are constants of universal character. More details, especially on the turbulence intermittency, are presented in the original paper [48].

2.4.5. Daughter size distribution functions

The source term which characterizes birth due to droplet breakage in the population balance equation Eq. 2.4 is expressed as:

$$S_{B,b} = \int_v^\infty p(v')\beta(v|v')\Gamma(\boldsymbol{x}, v')n(v', t)dv'$$

In order to compute it, and besides the breakage kernel, two additional terms have to be defined: $p(v')$ and $\beta(v|v')$. $p(v')$ is the number of daughter droplets which are created from the mother drop breakage. Binary breakage is generally assumed, based on the experiments of Hesketh [47], who observed that breakage leads to the formation of two "main" daughter droplets and a satellite one, whose dimension is small and can be neglected. $\beta(v|v')$ is the daughter size distribution function (DDF). It represents the probability that a mother droplet of volume v breaks into a daughter droplet of volume $vf_{BV,}$, and a second one of volume equal to $v(1 - f_{BV})$. To ensure mass conservation the DDF must obey the following relations:

$$\int_0^\infty \beta(v|v')\,dv' = 1$$

$$\int_0^\infty v'\beta(v|v')\,dv' = v$$

where v stands for the volume of the mother droplet and v' for the daughter droplet.

Different DDF have been proposed in the literature. The first class of functions to be employed were the normal distributions, as proposed by Valentas [49]. For these functions, the highest probability corresponds to the formation of two equi-sized droplets (see **Erreur ! Source du renvoi introuvable.**1).

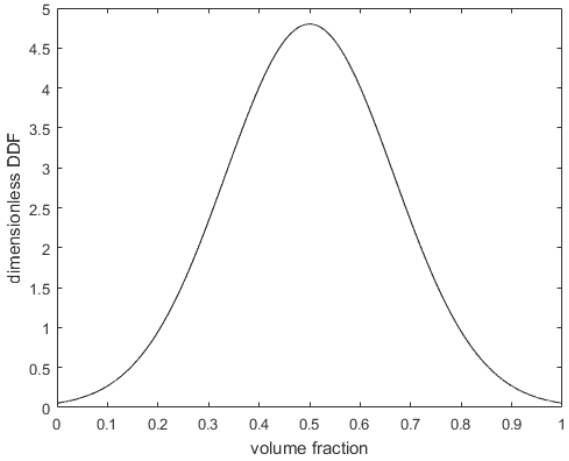


Figure 2.1: Representation of the daughter size distribution function proposed by Valentas and implemented by Coulaloglou and Tavlarides

Nambiar [13], in contrast, highlighted that the formation of two equi-sized droplets is the most energetic event among the possible ones, and should therefore be the least probable one. Indeed, as already seen in the Luo and Svendsen model, the surface energy increase is related to the volume (fraction) of the daughter droplet according to:

$$\Delta e_i(f_{BV}, d) = \left({f_{BV}}^{\frac{2}{3}} + (1 - f_{BV})^{\frac{2}{3}} - 1\right)\pi d^2\sigma = c_f \pi d^2 \sigma$$

which, as illustrated in Figure 2.2, is minimum when f_{BV} equals 1 (or 0), meaning that no breakage occurs, and maximum when f_{BV} is 0.5, *i.e.* in the case of the formation of two equisized daughter droplets.

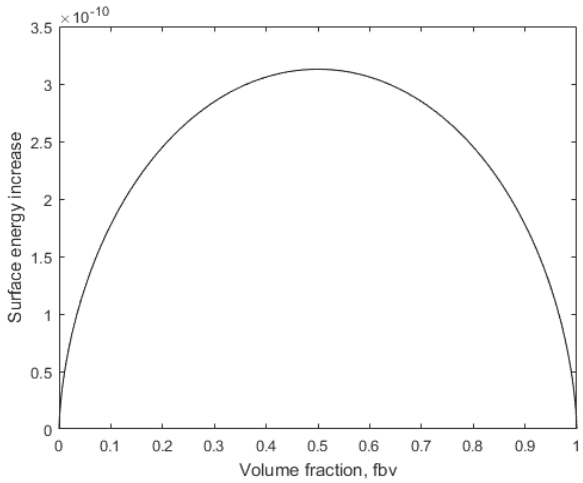


Figure 2.2: Surface energy increase as function of the volume fraction of the daughter droplet

Based on this energy constraint, some authors employed a U-shaped DDF in their model (Fig. 2.3, left). Wang, besides the energy constraint, considered also a pressure constraint, and therefore assumed a M-shaped distribution [11] (Fig 2.3, right).

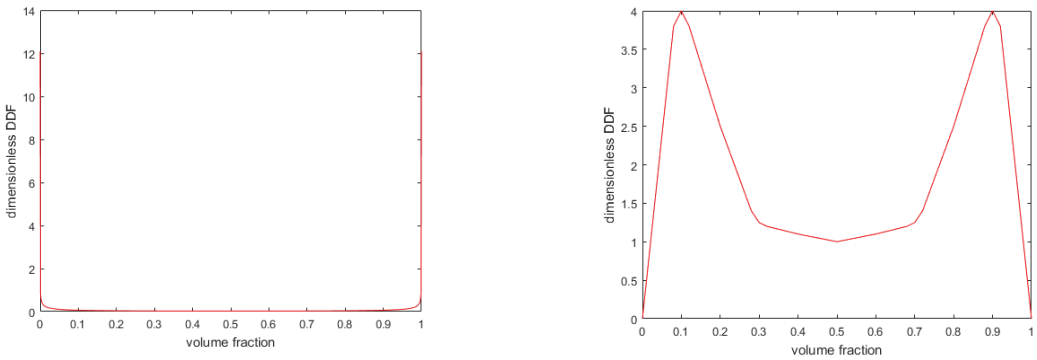


Figure 2.3: Examples of U-shaped (left) and M-shaped (right) daughter size distribution functions

In this work, in accordance with the Coulaloglou and Tavlarides model and the experimental observations reported in the literature [50], a normal distribution is adopted.

2.5. Coalescence kernels

2.5.1. The Coulaloglou and Tavlarides model

The Coulaloglou and Tavlarides coalescence kernel [10] is based on the film drainage theory of Shinnar and Church [51]. This theory states that when two particles collide, a film of liquid is retained between them. In order to achieve droplet coalescence, the droplet adhesive forces have to be strong enough to drain the liquid film between them.

Coulaloglou and Tavlairdes considered the coalescence frequency as the product of a collision frequency and a collision efficiency:

$$Q(v,v') = h(v,v')\lambda(v,v') \tag{2.49}$$

The expression of the collision frequency, $h(v,v')$, is based on the kinetic theory of gases:

$$h(v,v') = \left(\frac{9\pi}{2}\right)^{\frac{1}{3}}\left(v^{\frac{2}{3}} + v'^{\frac{2}{3}}\right)\left(\langle[\Delta u(v)]^2\rangle + \langle[\Delta u(v')]^2\rangle\right) \tag{2.50}$$

As in the case of breakage, the authors considered the flow to be fully turbulent and the droplets to have dimensions in the inertial subrange which leads to:

$$h(v,v') = C_3\varepsilon^{1/3}\left(v^{\frac{2}{3}} + v'^{\frac{2}{3}}\right)\left(v^{\frac{2}{9}} + v'^{\frac{2}{9}}\right)^{1/2} \tag{2.51}$$

In order for coalescence to occur, the droplet contact time, $\bar{t}$, which depends on the adhesive forces, has to be higher than the coalescence time, $\bar{\tau}$, which is the time required to drain the liquid film. The contact time of two droplets in a turbulent field was expressed as:

$$\bar{t} \approx \frac{(d+d')^{\frac{2}{3}}}{\varepsilon^{\frac{1}{3}}} \tag{2.52}$$

while the coalescence time, $\bar{\tau}$, as:

$$\bar{\tau} \approx \frac{\mu_c \rho_c \varepsilon^{\frac{2}{3}} (d+d')^{\frac{2}{3}}}{\sigma^2} \left(\frac{1}{h^2} - \frac{1}{h_0^2}\right) \left(\frac{dd'}{d+d'}\right)^2 \tag{2.53}$$

where h_0 and h are the film thicknesses at the initial and the draining time.

Considering Eq. 2.52 and 2.53 for $\bar{t}$ and $\bar{\tau}$, Coulaloglou and Tavlarides expressed the collision efficiency as:

$$\lambda(v,v') = \exp\left(-\frac{c_4 \mu_c \rho_c \varepsilon}{\sigma^2} \left(\frac{v^{\frac{1}{3}} v'^{\frac{1}{3}}}{v^{\frac{1}{3}} + v'^{\frac{1}{3}}}\right)^4\right) \tag{2.54}$$

Finally, the coalescence kernel reads:

$$Q(v,v') = c_3 \left(v^{\frac{2}{3}} + v'^{\frac{2}{3}}\right)\left(v^{\frac{2}{9}} + v'^{\frac{2}{9}}\right)\varepsilon^{\frac{1}{3}} \exp\left(-\frac{c_4 \mu_c \rho_c \varepsilon}{\sigma^2} \left(\frac{v^{\frac{1}{3}} v'^{\frac{1}{3}}}{v^{\frac{1}{3}} + v'^{\frac{1}{3}}}\right)^4\right) \tag{2.55}$$

2.5.2. The Sovova model

Sovova [52] developed a coalescence kernel based on the Howarth theory [53]. Unlike Shinnar [51], who assumed that coalescence could take place if the adhesive forces between the colliding droplets are strong enough to break the retained film of liquid, Howarth stated that the latter are too weak. The author, instead, assumed that the liquid film breaks due to the energy transferred during the droplet collisions. As in the case of the previous model, Sovova expressed the coalescence kernel as the product of a collision frequency and a collision efficiency (see Eq. 2.49). While the collision frequency has the same expression as in the Coulaloglou and Tavlarides one, the collision efficiency is defined as:

$$\lambda(v,v') = \exp\left(-\frac{c_8\sigma\left(v^{\frac{2}{3}}+v'^{\frac{2}{3}}\right)(v+v')}{\rho_c\varepsilon^{\frac{2}{3}}vv'\left(v^{\frac{2}{9}}+v'^{\frac{2}{9}}\right)}\right) \quad (2.56)$$

which, combined with Eq. 2.50, gives:

$$Q(v,v') = c_3\left(v^{\frac{2}{3}}+v'^{\frac{2}{3}}\right)\left(v^{\frac{2}{9}}+v'^{\frac{2}{9}}\right)\varepsilon^{\frac{1}{3}} \times \exp\left(-\frac{c_4\sigma\left(v^{\frac{2}{3}}+v'^{\frac{2}{3}}\right)(v+v')}{\rho_c\varepsilon^{\frac{2}{3}}vv'\left(v^{\frac{2}{9}}+v'^{\frac{2}{9}}\right)}\right) \quad (2.57)$$

Sovova lastly considered that the mechanism proposed by Shinnar (the drops are attracted by a force proportional to their surfaces during their collision) and Howarth (i.e. adhesion forces are weak compared to the collision forces) could both be involved in the coalescence. Therefore, he proposed to consider the collision efficiency as the resulting force of both the adhesive forces, and of the turbulent collisions:

$$\lambda'(v,v') = \lambda_{SOVOVA}(v,v') + \lambda_{COULALOGLOU}(v,v') - \lambda_{SOVOVA}(v,v')\lambda_{COULALOGLOU}(v,v') \quad (2.58)$$

In this work, the models proposed by Coulaloglou and Tavlarides have been considered, since they were found to reproduce well enough the experimental data of turbulent liquid-liquid dispersions [10,17,54]. Anyway, this PhD thesis aimed at improving these models with regards to:

- the assumption, solving a 0D PBE model, of a uniform turbulent dissipation rate in the liquid-liquid contactor, which is a rough approximation of the physics of the systems
- the assumption of droplets having dimension in the inertial subrange of turbulence which permits to approximate the second-order structure function according to Eq. (2.32). Indeed, it will be shown, that in a turbulent liquid-liquid dispersion the majority of the droplets have dimensions in the dissipation subrange of turbulence

In order to overcome the first assumption, a model based on the probability density function (PDF) of ε that accounts for the ε inhomogeneities is discussed and validated. Then, regarding the second assumption, a generalization of the Coulaloglou and Tavlarides kernels

based on a more refined second-order structure function is proposed. The exploitation of these two models requires the PDF of ε, which are obtained running CFD simulations. Their validation is carried out on turbulent liquid-liquid experiments performed in a stirred tank reactor and a pulsed column. The CFD simulations and of the performed experiments are detailed in the next chapter.

3. Materials and methods

This chapter is divided in a first section presenting the liquid-liquid dispersion experiments and a second one where the CFD simulations are detailed.

Turbulent liquid-liquid dispersion experiments have been carried out in order to validate the proposed improvements of the breakage and coalescence models. Due to the interest in the PUREX process, the experiments were performed in liquid-liquid extractors which are relevant for solvent extraction: the stirred tank reactor and the pulsed column. The dispersions were constituted of an aqueous and an organic phase. The final aim of these experiments was the determination of some fundamental parameters in the mass transfer-process, as the Sauter mean diameter of the droplet population and the dispersed phase volume fraction.

Complementing the experiments, the CFD simulations have been run in order to obtain the ε spatial distribution in the liquid-liquid contactors (stirred tank reactor and pulsed column). The PDFs of ε have later been implemented in the MATLAB routines solving the PBE model.

3.1. Experiments

3.1.1. Aqueous and organic phases

In this section, the properties of the liquids employed in the experiments are detailed. A dispersion is characterized by the presence of two immiscible phases where one is dispersed in the form of droplets in the second continuous one. The non-miscibility of the two phases highly simplifies the solute transfer process. Indeed, the two phases are intimately contacted to increase the interfacial area and the mass-transfer rates. Once the extraction is complete, the two phases can be separated in a decanter.

Three important liquid properties characterize the liquid-liquid extraction process: the surface tension, the density and the viscosity. The surface tension, σ, is defined as the force per unit length which must be applied to the border of a bended membrane to keep it flat. While in one hand, high values of σ have the drawback to increase the energy demand to create small droplets (which leads to higher interfacial areas), on the other hand, high surface tensions lead

to a faster separation of the two phases in the decanter. The density difference between the two phases is also an important parameter. Indeed, the higher this difference, the lower the settling time. The viscosity of the dispersed phase also influences the breakage rate. Indeed, this property tends to counterbalance the turbulent stresses, which cause the droplet breakage, to restore the initial droplet form [16]. Finally, the continuous viscosity affects the film-draining process during coalescence in both the mixing and the settling part of the contactor.

Due to the polarity of the aqueous phase and the non-polarity of the organic phase, which lead to the non-miscibility of the two phases, the systems employed in liquid-liquid extraction often consist in mixture of water and oil. Indeed, water molecules which are polar due to the different electronegativity of oxygen and hydrogen tend to stick together, while long hydrocarbon chains are repulsed by these electrical charges. In this work, therefore, aqueous and organic phases will be contacted to create the dispersions. While oil-in-water dispersion are the most common in solvent extraction, both oil-in-water and water-in-oil dispersions are considered in this study, since the two configurations are encountered in the nuclear fuel reprocessing process. Surfactants were not added to the dispersion, since they are not used in the PUREX process.

For the experiments, pure de-ionized water was considered, whose properties are listed in Table 3.1, together with "chemically inert" organic phases. Most of the tests implemented Isane 175-in-water and water-in-Isane 175 dispersions. Isane 175 is an isoparaffanic mixture of hydrocarbon chains with 12 to 14 carbon atoms employed in the hand-soaps, resins and alkyd paints production. The reason why this compound was employed is due to its similar properties to the solvent employed in the PUREX process, the Tetra-Propylene Hydrogeneized. Isane 175 is characterized by a low viscosity, close to the water one, and exhibits a lower density.

Focusing on the modeling of the dispersed phase properties evolution at higher continuous phase viscosities, experiments implementing a more viscous organic continuous phase were performed. In order to increase the latter, Marcol 82 was added to Isane 175. Marcol 82 is a purified mixture of saturated hydrocarbons and it is employed in the production of cosmetic products as gels, body lotions and cream and shampoos. Marcol 82 has a high viscosity (Table 3.1) and it is completely miscible in Isane 175.

Table 3.1: Physico-chemical properties of the liquids employed in the turbulent liquid-liquid dispersions

Marcol (%)	Isane (%)	Water (%)	μ [cP]	ρ [kg/m^3]	σ [mN/m]
0	0	100	1.01	997.8	---
0	100	0	1.22	757.4	38.3
100	0	0	12.00	829.7	40.3
30	70	0	2.43	783.4	38.2
45	55	0	4.10	799.9	39.8

3.1.2. Liquid-liquid contactors

3.1.2.1. The Stirred Tank Reactor

The turbulent liquid-liquid dispersion experiments were carried out in a stirred tank reactor. This equipment is heavily used in the chemical, pharmaceutical, food, nuclear industry either for running chemical reactions or for separation processes.

The stirred tank reactor (STR) is a cylindrical vessel equipped with one or more impellers and baffles. The impeller, which represents the core of the mixing operation, can have different geometries according to the operation it must accomplish. For low to medium viscosities, turbines and propellers are the most suitable impellers.

The turbines are radial flow impellers that lead to the formation of two convective cells in the vessel, which lower the mixing in the reactor. Turbines transmit more energy to the liquid than a propeller, inducing higher droplet breakage rates. The propellers, instead, are characterized by an axial flow which favors the formation of a unique convective cell, and, therefore, a better mixing than the radial flow impellers [55,56].

In the case of a turbulent flow, the STR is provided with baffles which prevent the formation of a vortex into the vessel. The baffles are vertical plates placed perpendicularly to the vessel walls.

An impeller can be characterized by non-dimensional numbers: the impeller Reynolds number (Re_t), the Froude number (Fr), the Power number (Np) and the pumping number (Nq) [57]. The impeller Reynolds number is useful to define the kind of flow achieved in the vessel:

$$Re_t = \frac{\rho N_r D^2}{\mu}$$

For $Re_t < 100$ the flow is laminar, while it is turbulent for $Re_t > 10{,}000$. In between these values a transitional flow characterized by temporary instabilities takes place. The limiting Re_t value for a turbulent flow must be considered with caution, since other authors proposed different values. Grenville [58], indeed, expressed the lower limit for turbulent flows as:

$$Re_t = \frac{6370}{N_p{}^{\frac{1}{3}}}$$

where N_p is the Power number. This non-dimensional number is proportional to the kinetic energy transmitted by the impeller to the liquid. It strongly depends on the shape of the impeller. The Power number is defined as:

$$N_p = \frac{P}{\rho {N_r}^3 D^5}$$

Where P is the power provided by the impeller to the liquid, and it is equal to $P = \bar{\varepsilon} m$. Therefore:

$$\bar{\varepsilon} = \frac{N_p {N_r}^3 D^5}{V}$$

where $\bar{\varepsilon}$ is the volume-averaged turbulent dissipation rate. This equation is of fundamental importance in this work since the results of the performed CFD simulations of the STR (see

Sec. 4.1) will be compared to this value. The Power number is constant in the region of turbulent Reynolds numbers for most of the impellers in STR with geometrical similarity (Fig. 3.1)

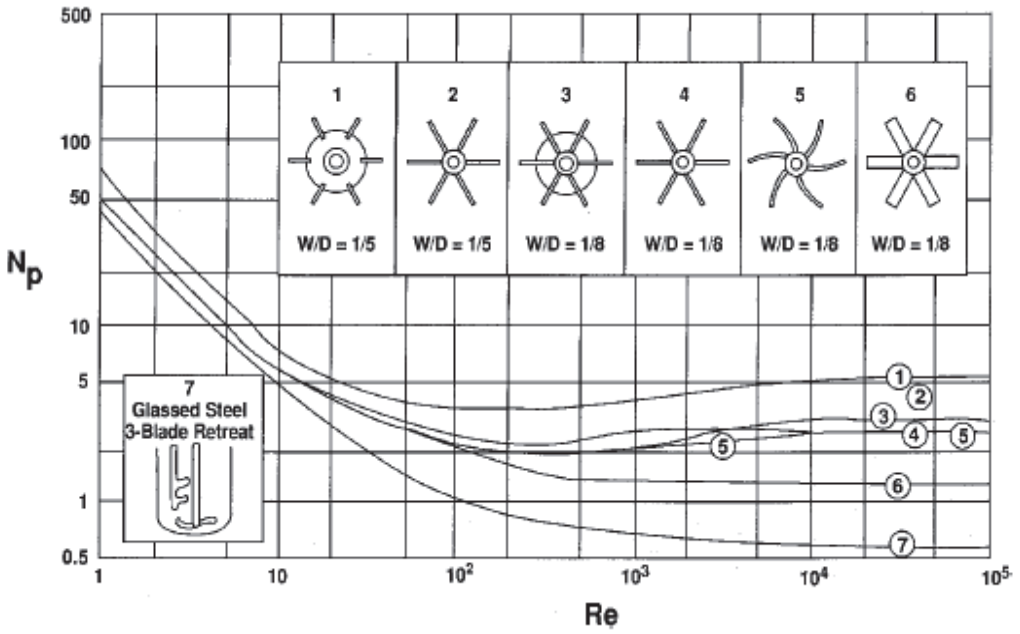


Figure 3.1: Power number N_p for different impellers taken from [55]

In the case of an unbaffled vessel, the power transmitted by the impeller to the liquid could be influenced by the Froude number, which represents the ratio between centrifugal and gravitational forces:

$$Fr = \frac{{N_r}^2 D}{g}$$

Since the STR used in the experiments is equipped with four baffles, the Froude number is not considered.

Finally, a mechanically agitated vessel is characterized by the pumping number N_q. This non-dimensional number is proportional to the volumetric flow rate leaving the discharge side of the impeller and is expressed as:

$$N_q = \frac{Q}{N_r D^3}$$

Since this work focuses on droplet breakage and coalescence, which are not influenced by the volumetric flow rate discharged by the impeller, this non-dimensional number is not considered.

All the experiments dedicated to the kernel development were carried out in a STR equipped with a Mixel-TT impeller and four baffles. The STR has a height of H =120 mm, and a diameter of the same size ($T = H$). The impeller diameter, D, is half of the tank one ($D = T/2$). It is located at $H/3$ = 40 mm from the bottom of the reactor. The baffles have a width of 15 mm ($T/8$) and a thickness of 5 mm (Fig. 3.2).

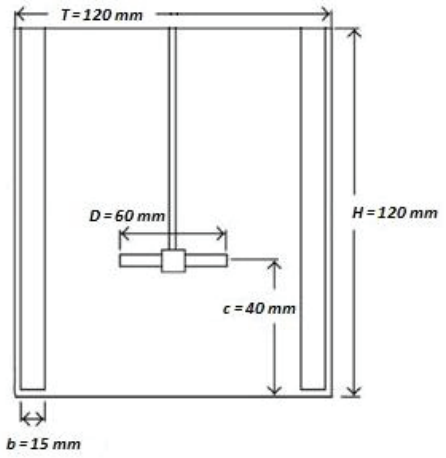


Figure 3.2: Geometry of the stirred tank reactor

The Mixel-TT (Fig. 3.3) is a 3-blade propeller characterized by a power number $N_p = 0.81$ in the turbulent domain. This impeller guarantees good recirculation of the fluid inside the vessel and moderate shear rate.



Figure 3.3: Interior of the stirred tank reactor

3.1.2.2. The pulsed column

Additional experiments were performed in a pneumatic pulsed column. This liquid-liquid extractor is employed in the nuclear recycle industry mainly because it does not present any rotating or mechanical parts that could need maintenance in a radiotoxic environment.

The pulsed column is constituted of a cylindrical shell in which the water/oil dispersion is created. In order to achieve counter-current flow, and according to their density difference, the aqueous and the organic phases are fed respectively at the top and at the bottom of the column. In the case of water-in-oil configuration, phase separation is achieved at the bottom of the column, in the lower settler, where the dispersed aqueous phase is collected. Alternately, for the oil-in-water configuration, phase separation occurs in the upper settler. An auxiliary "leg" connects the base of the pulsed column to a three-way valve with one way periodically exposed to pressurized air. This system generates a periodic movement of the air in the leg and consecutively of the fluid in the column, which can be characterized by an amplitude (A) and a frequency (f). The amplitude represents the distance travelled by the liquid in the column due to the pulsation, while the frequency represents the inverse of the duration of a pulsation cycle. In order to enhance the formation of smaller droplets, the pulsed column used in this study was packed with a series of disks and rings.

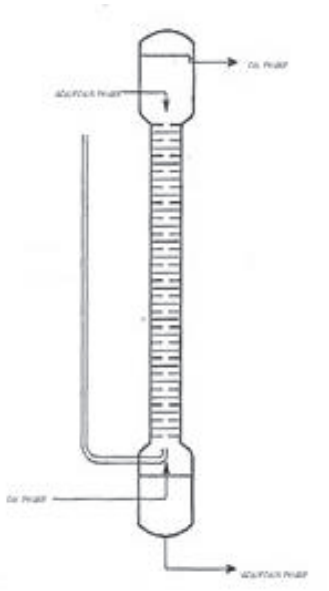


Figure 3.4: Scheme of a pulsed column

With a diameter of 25 mm and a height of 2 m, it is similar to the one used in previous studies [17,54]. It is composed of 20 compartments, where a compartment is defined as the volume enclosed between two disks (or two doughnuts). The disks and rings are 1 mm thick and 24 mm distant. The disks have a diameter of 21.22 mm, while the doughnuts are 12.75 mm inner diameter and 25 mm external. For this specific column, no gap exists between the doughnut and the shell.

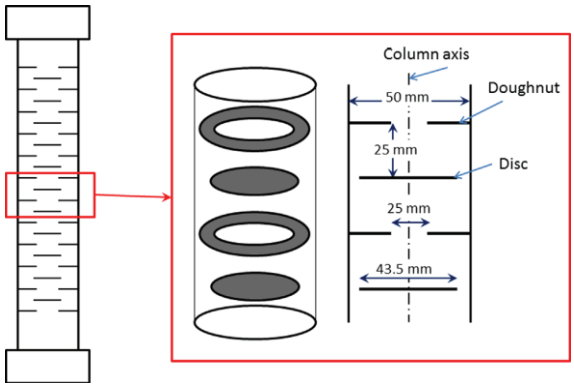


Figure 3.5: Packing of the lab-scale column employed for the experiments [17]

The experiments in the pulsed column were carried on in a water-in-oil configuration. The column is connected to three pumps. Two pumps are employed to aliment the aqueous and the organic phases. The last pump is used to withdraw the water collected in the decanter in order to stabilize the position of the water/oil interface.



Figure 3.6: Lab-scale pulsed column

3.1.3. The SOPAT probe and software

In order to determine the time evolution of the droplet size distribution and the Sauter mean diameter for the turbulent liquid-liquid dispersions in the stirred tank reactor and the in the pulsed column, the SOPAT probe has been employed [22,54,59–62].

The SOPAT probe (Fig. 3.7) is an endoscopic photo-optical device which permits to acquire images of the droplets with size between 20 μm and 3 mm in the liquid-liquid contactor.

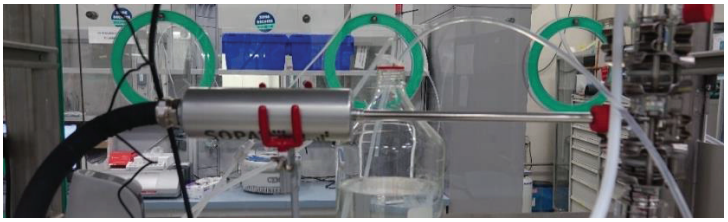


Figure 3.7: SOPAT endoscopic probe

The probe is provided with an optic fiber which generates light flashes. These latter are differently reflected according to the refraction index of the two phases. The objects generated by the different light reflection are captured by a 6 mega-pixel CCD high-speed camera. The acquired images are processed through the software provided by SOPAT (Annex I). Useful information is thereby obtained on the droplet population, as its number and volume distribution functions and the Sauter mean diameter. In order to obtain accurate values of these properties, an important number of pictures is acquired. In this way, a representative number (at least 3000) of droplets present in the liquid-liquid dispersion is analyzed. More details on the SOPAT probe are provided in Chap. 4-5 and Annex I.

3.2. Numerical models

3.2.1. CFD simulations

In order to determine the flow properties needed for the breakage and coalescence kernel computation, Computational Fluid Dynamics simulations were run.

CFD has been strongly developed in the last years to solve, by means of computers, the transport equations for momentum, heat and mass [63,64]. Among the transport equations, the continuity and the momentum equations (together known as the Navier-Stokes (NS) equations) cover a fundamental role:

$$\frac{d(\rho u_j)}{dx_j} = 0$$

$$\frac{d(\rho u_i)}{dt} + \frac{d(\rho u_i u_j)}{dx_j} = \frac{d}{dx_j}\left(\mu \frac{du_i}{dx_j}\right) - \frac{dp}{dx_i} \tag{3.26}$$

Solving this set of equations provides details about the flow turbulent properties that influence the breakage and coalescence kernels. Although being of extreme usefulness, the NS equations present the drawback of being hard to solve. Many approaches have been proposed for their solutions. The simplest to understand, but also the most complicated to apply due to

the demanded computational resources, is the Direct Numerical Simulation (DNS). This approach is based on the solution of the discretized NS equations (finite differences, volumes or elements) on a proper time and space meshes to represent each scale of the involved phenomena. The problem resides in the fact that the turbulence is characterized by length and velocity scales of a spread order of magnitudes which, in order to be simulated, require computational resources that are still far beyond the ones of the modern supercomputers.

Another approach that is more and more used in the solution of NS equations for industrial applications is the Large Eddy Simulation (LES) method. Since a turbulent flow is characterized by big anisotropic eddies and by smaller eddies which have a universal behavior, a filtering operation is carried out in the NS equations in order to solve directly the length and velocity scales of the bigger eddies and model the behavior of the smaller ones:

$$\tilde{u}(\boldsymbol{x},t) = \int_{-\infty}^{\infty}\int_{-\infty}^{\infty}\int_{-\infty}^{\infty} G(\boldsymbol{x},\boldsymbol{x}',\Delta)u(\boldsymbol{x}',t)d\boldsymbol{x}'$$

where $\tilde{u}(\boldsymbol{x},t)$ is the filtered function, $G(\boldsymbol{x},\boldsymbol{x}',\Delta)$ the filter function, whose cutoff Δ represents the smallest length scale solved in the equations, and $u(\boldsymbol{x}',t)$ the unfiltered function. Since in this work, the LES method has not been used, it will not be further described.

The most employed approach for the solution of the NS equations is the Reynolds-Averaged Navier-Stokes (RANS) method. Since this method is implemented in the CFD solver employed in the simulations of the liquid-liquid extractors (ANSYS Fluent), it will be detailed in the following sections.

3.2.1.1. RANS method

In this work, single-phase CFD simulations are performed (water, Isane, mixture Isane/Marcol). Therefore, the NS equations can be written as:

$$\frac{du_j}{dx_j} = 0 \tag{3.27}$$

$$\rho\frac{du_i}{dt}+\rho\frac{d(u_iu_j)}{dx_j}=\frac{d\tau_{ij}}{dx_j}-\frac{dp}{dx_i}$$

where $\tau_{ij}=2\mu s_{ij}$ and:

$$s_{ij}=\frac{1}{2}\left(\frac{du_i}{dx_j}+\frac{du_j}{dx_i}\right)$$

The RANS approach is based on the decomposition of the instantaneous velocity u_i and the pressure p as the sum of the average $(\overline{u_\iota},\bar{p})$ and fluctuating components (u_i',p'):

$$\begin{aligned}u_i&=\overline{u_\iota}+u_i{}'\\p&=\bar{p}+p'\end{aligned}\tag{3.28}$$

by substituting Eq. 3.28 in Eq. 3.27, the following expression is obtained:

$$\rho\frac{d(\overline{u_\iota}+u_i')}{dt}+\rho\frac{d[(\overline{u_J}+u_j')(\overline{u_\iota}+u_i')]}{dx_j}=\frac{d}{dx_j}\left(2\mu\frac{d(\overline{s_{IJ}}+s_{ij}{}')}{dx_j}\right)-\frac{d(\bar{p}+p')}{dx_i}\tag{3.29}$$

Then, a time-average procedure must be applied to Eq. 3.29:

$$\frac{1}{\Delta t}\int_t^{\Delta t}\left\{\rho\frac{d(\overline{u_\iota}+u_i')}{dt}+\rho\frac{d[(\overline{u_J}+u_j')(\overline{u_\iota}+u_i')]}{dx_j}\right\}dt=\frac{1}{\Delta t}\int_t^{\Delta t}\left\{\frac{d}{dx_j}\left(2\mu\frac{d(\overline{s_{IJ}}+s_{ij}{}')}{dx_j}\right)-\frac{d(\bar{p}+p')}{dx_i}\right\}dt\tag{3.30}$$

Knowing that (the same relations are valid for the pressure):

$$\frac{1}{\Delta t}\int_t^{\Delta t}u_i\,dt=\langle\overline{u_\iota}\rangle$$

$$\frac{1}{\Delta t}\int_t^{\Delta t}\overline{u_\iota}\,dt=\langle\overline{u_\iota}\rangle$$

$$\frac{1}{\Delta t}\int_{t}^{\Delta t} u_i' dt = 0$$

Inverting the order of the integral and derivative operators, applying time-average procedure properties and rearranging, the RANS formulation reads:

$$\rho\frac{d\langle\overline{u_\iota}\rangle}{dt} + \rho\frac{d\langle\overline{u_\iota u_j}\rangle}{dx_j} = \frac{d}{dx_j}\left(2\mu\frac{d\langle\overline{s_{ij}}\rangle}{dx_j} - \rho\langle u_i' u_j'\rangle\right) - \frac{d\langle\bar{p}\rangle}{dx_i} \tag{3.31}$$

The final equation differs from the instantaneous variables NS formulation by the presence of the Reynolds stress tensor, $-\rho\langle u_i' u_j'\rangle$. Unfortunately, since the velocity fluctuation components in a turbulent flow are correlated, this term is not null and has to be modeled.

Boussinesq [64] expressed the Reynolds stress tensor in a similar way to the viscous stresses tensor, since the flow turbulence is proportional to the mean deformation rate:

$$\tau_{REYNOLDS,ij} = -\rho\langle u_i' u_j'\rangle = \mu_t\left(\frac{d\overline{u}_\iota}{dx_j} + \frac{d\overline{u}_J}{dx_i}\right) - \frac{2}{3}\rho k\delta_{ij} \tag{3.32}$$

Where k, the turbulent kinetic energy, is expressed as:

$$k = \frac{1}{2}\left(\overline{u'^2} + \overline{v'^2} + \overline{w'^2}\right)$$

In order to determine the Reynolds stress tensor, the turbulent viscosity μ_t must be computed. Many models have been proposed in literature in order to accomplish this task. According to the additional differential equation that will be solved, the models will be called algebraic (no additional differential equations), one-equation or two-equation models. Since in this work the $k-\varepsilon$ model is going to be used, it will be discussed in the next section.

3.2.1.1.1 The $\boldsymbol{k-\varepsilon}$ two-equation model

The two-equation turbulence models are characterized by the solution of two additional partial differential equations. Generally, one of the two equations solve the time and spatial

evolution for the turbulent kinetic energy k. The k-equation can be obtained by multiplying the fluctuating velocity u_i' times the NS and the RANS equations, and by subtracting the former obtained equation from the latter. After algebraic rearrangement, the k-equation reads:

$$\rho\frac{dk}{dt}+\rho\frac{d(\overline{u_j}k)}{dx_j}=\frac{d}{dx_j}\left(-\overline{u_j'p'}+\mu\frac{dk}{dx_j}-\rho\frac{1}{2}\overline{u_\iota'u_\iota'u_j'}\right)-2\mu\overline{s_{\iota J}'s_{\iota J}'}+\rho\overline{u_\iota'u_\iota'}s_{ij} \quad (3.38)$$

The k-equation is characterized by an accumulation and an advection term. The first left hand-side term represents the transport of k due to pressure, viscous and Reynolds stresses. $-2\mu\overline{s_{\iota J}'s_{\iota J}'}$ represents the turbulent kinetic dissipated energy. Dividing this term by ρ, the turbulent kinetic energy dissipation rate is obtained:

$$\varepsilon=2\nu\overline{s_{\iota J}'s_{\iota J}'}$$

Finally, the last term represents the generation of turbulent kinetic energy in the flow. The transport of k due to pressure and the Reynolds stresses is simplified according to the following relation:

$$\overline{u_j'p'}+\rho\frac{1}{2}\overline{u_\iota'u_\iota'u_J'}=\rho\frac{\nu_t}{\sigma_k}\frac{dk}{dx_j} \quad (3.39)$$

Where σ_k is a non-dimensional parameter. The final k-equation reads:

$$\rho\frac{dk}{dt}+\rho\frac{d(\overline{u_j}k)}{dx_j}=\frac{d}{dx_j}\left[\left(\mu+\rho\frac{\nu_t}{\sigma_k}\right)\frac{dk}{dx_j}\right]-\rho\varepsilon+\rho\overline{u_\iota'u_\iota'}s_{ij} \quad (3.40)$$

The $k-\varepsilon$ model considers a second differential equation for the turbulent kinetic energy dissipation rate ε. The solution of this equation allows the calculation of the turbulent diffusivity as follows:

$$\mu_t = \rho C_\mu \frac{k^2}{\varepsilon} \tag{3.41}$$

An exact equation for ε may be obtained by applying the following operator to the NS equation:

$$2\nu \overline{\frac{du_\iota'}{dx_J}\frac{d}{dx_\iota}[NS(u_\iota)]} = 0 \tag{3.42}$$

The problem of the resulting equation is its complexity. Therefore, by analogy with the equation of the turbulent kinetic energy (Eq. 3.40), an easier ε-equation has been proposed [63,64]:

$$\rho\frac{d\varepsilon}{dt} + \rho\frac{d(\overline{u_j}\varepsilon)}{dx_j} = \frac{d}{dx_j}\left[\left(\mu + \rho\frac{\nu_t}{\sigma_k}\right)\frac{d\varepsilon}{dx_j}\right] - \rho C_{\varepsilon 2}\frac{\varepsilon^2}{k} + \rho C_{\varepsilon 1}\frac{\varepsilon}{k}\overline{u_\iota' u_\iota'} s_{ij} \tag{3.43}$$

The solution of the two additional equations allow the determination of the turbulent viscosity and consecutively of the RANS equations. In this work, the $Standard\ k-\varepsilon$ model is employed in the CFD simulations of the liquid-liquid contactors.

3.2.1.2. CFD simulation of the stirred tank reactor

CFD simulations of the experimental stirred tank reactor have been performed in order to determine the turbulent kinetic energy rate dissipation ε. Indeed, as already discussed in the previous sections, ε is of crucial importance in the computation of the breakage and coalescence kernels.

The mesh of the reactor has been realized with the ANSYS Meshing software. Due to the particular geometry of the impeller (Fig 3.8), an unstructured tetrahedral mesh was built.

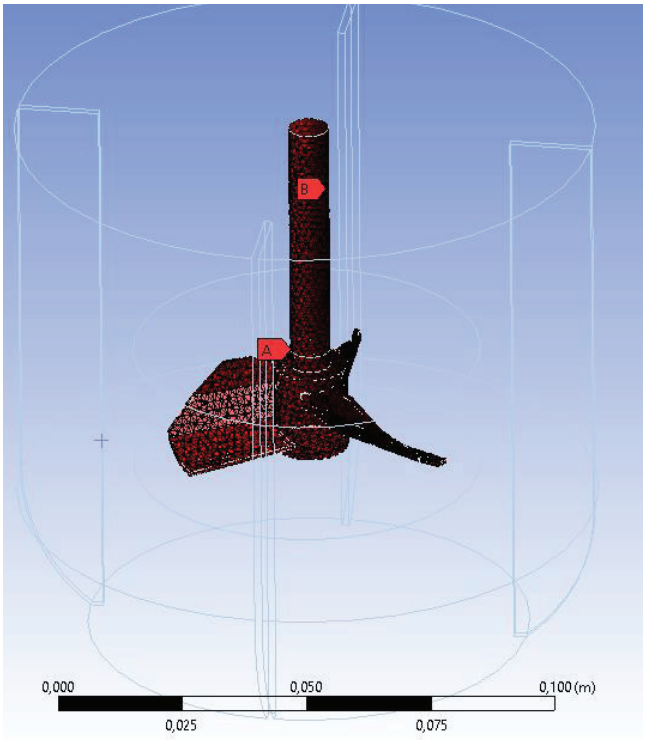


Figure 3.8: Surface mesh of the Mixel TT impeller

The quality of a mesh can be assessed by its orthogonal quality and skewness. For each cell, the orthogonal quality is given by [65]:

$$orthogonal\ quality = \min\left(\frac{\overrightarrow{A_i}.\overrightarrow{f_i}}{|\overrightarrow{A_i}|.|\overrightarrow{f_i}|}, \frac{\overrightarrow{A_i}.\overrightarrow{c_i}}{|\overrightarrow{A_i}|.|\overrightarrow{c_i}|}\right)$$

Where $\overrightarrow{A_i}$ represents the normal vector to the i^{th} face of the cell, $\overrightarrow{f_i}$ the vector connecting the cell centroid to the centroid of the i^{th} face and $|\overrightarrow{c_i}|$ the vector connecting the centroids of the two cells which share the i^{th} face. The orthogonal quality can have values between 0 and 1, which represent respectively the worst and best quality achievable.

The skewness, instead, determines how far from ideal geometrical shapes (equilateral or equiangular) a cell face is. This quantity has values in between 0 and 1, where they respectively represent the best and the worst quality. The present mesh has an average skewness of 0.2, which corresponds to high quality.

A stirred tank reactor is characterized by the presence of a rotating part that must be treated with caution. Two possible approach can be employed: the sliding mesh technique and the Moving Reference Frame method, which will be detailed further.

The MRF [66,67], also called frozen-rotor approach, is a method which considers different coordinate systems for the rotating and fixed parts. According to this method, the impeller is assumed to be still with regards to the coordinate system that rotates at the speed of the moving part. In order to implement this approach, the rotating part must be enclosed in a fluid subdomain (Fig. 3.9) for which a moving coordinate system is considered.

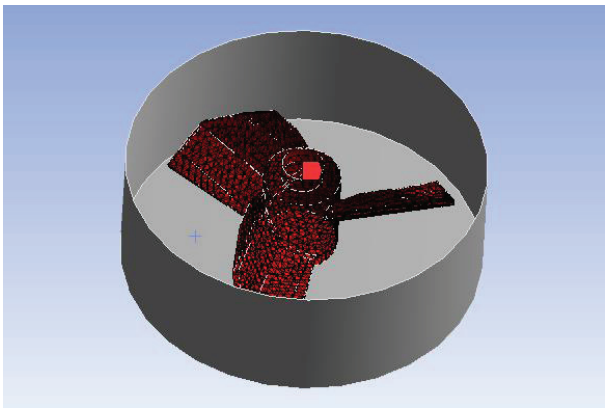


Figure 3.9: Section of the fluid subdomain where the MRF approach is applied

For the moving fluid subdomain, the momentum equations are modified including additional velocity and acceleration terms due to the non-inertiality of the coordinates system. Instead, in the rest of the fluid subdomain, an inertial coordinate system is assumed, and the usual momentum equations are solved. At the interface, a mathematical transformation is applied in order ensure mass and momentum fluxes continuity between the subdomains.

3D single-phase CFD simulations have been performed by employing the $k-\varepsilon$ model [66–68]. This model allows to get direct information of the turbulent kinetic energy dissipation rate which is the core of the breakage and coalescence kernel computation. As it will be discussed in the next chapter, the interest lies in the probability density function of ε. An enhanced wall treatment law implemented in ANSYS Fluent has been adopted. Indeed, since the turbulence is generated by the rotation of the impeller, it is fundamental to have an accurate

description of the velocity field in the proximity of the pale surfaces. A second-order upwind method was selected to discretize the mass and momentum equations in the solver. Indeed, this latter does not present numerical diffusion as in the case of a first-order upwind or overshoots as in the case of pure third-order schemes (MUSCLE). The simulations were run in transient since the convergence criteria were not achieved with steady simulations. The simulations were stopped once the volume-average turbulent dissipation rate was constant. Other details will be furnished in the Chap. 4.

3.2.1.3. CFD simulation of the pulsed column

Differently from the stirred tank reactor, the single-phase CFD simulations of the pulsed column are performed in a 2D frame, since the flow can be assumed to be axisymmetric [69–71].

Three compartments of the column were meshed (Fig. 3.10) in quadrilateral cells and the NS equations simulated in ANSYS Fluent. The time-averaged probability density function of ε has been extracted from the central compartment (Annex II), in order to dampen the inlet/outlet disturbances.

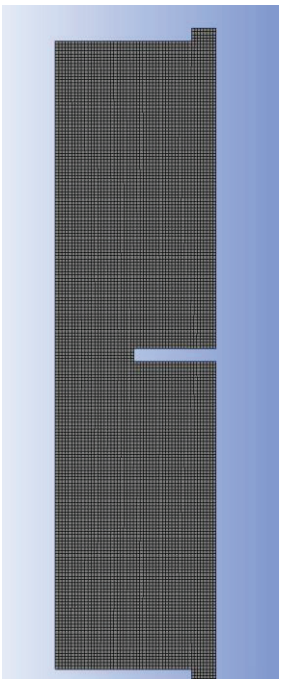


Figure 3.10: 2D mesh of 1 compartment of the pulsed column

As for the STR, the $Standard\ k-\varepsilon$ model was employed [17,70,71], along with an enhanced wall-function. The second-order upwind method has been selected to solve the mass and momentum equations. The simulations, due to the periodic flow behavior inside the column due to pulsations, have been run in transient. The inlet velocity has been modeled as:

$$v(t) = \pi A f \sin(2\pi f t)$$

where A and f are, respectively, the pulsation amplitude and frequency. An outlet pressure boundary condition was implemented at the exit of the column, assuming a gauge pressure equal to zero.

This function was used as boundary condition for the simulation and implemented in ANSYS Fluent through a User Defined Function (UDF). The simulation was stopped once 5 periods had been realized. Anyway, already from the second period on, the obtained results were periodic.

3.2.2. Note on the single-phase assumption

Single-phase CFD simulations have been run both for the STR and the pulsed column. This means that the turbulent properties of the two-phase flow have been assumed to be equal to the ones of the continuous phase considered alone, and that the effect of the dispersed phase on turbulence is negligible.

In order to evaluate the validity of these assumptions, two-phase CFD simulations of the stirred tank reactor were run and compared to the results obtained for the single-phase case. The simulations considering 1% of water-in-Isane at 700 rpm and 2% of water-in Isane at 800 rpm are discussed.

The flow was simulated through the Eulerian-Eulerian approach (EEM) present in ANSYS Fluent. Among the multiphase-flow model, the EEM is the more complex, since it solves a set of NS equations for each phase. These equations present additive terms to account for the phase interactions. To simulate the turbulence in the STR, the "Mixture Standard $k-\varepsilon$" model was employed. This approach assumes the two phases to form a mixture to which $k-\varepsilon$ equations are applied.

For both cases, it was found that the volume-averaged turbulent dissipation rates $\bar{\varepsilon}$ have similar values. Indeed, while for the two-phase cases $\bar{\varepsilon}$ is equal to 1.01 $\frac{m^2}{s^3}$ (1%, 700rpm) and 1.50 $\frac{m^2}{s^3}$ (2%, 800rpm), for the single-phase ones $\bar{\varepsilon}$ is equal to 0.99 $\frac{m^2}{s^3}$ (700rpm) and 1.49$\frac{m^2}{s^3}$ (800rpm). Also the probability density functions of the turbulent dissipation rate ε follow a similar trend:

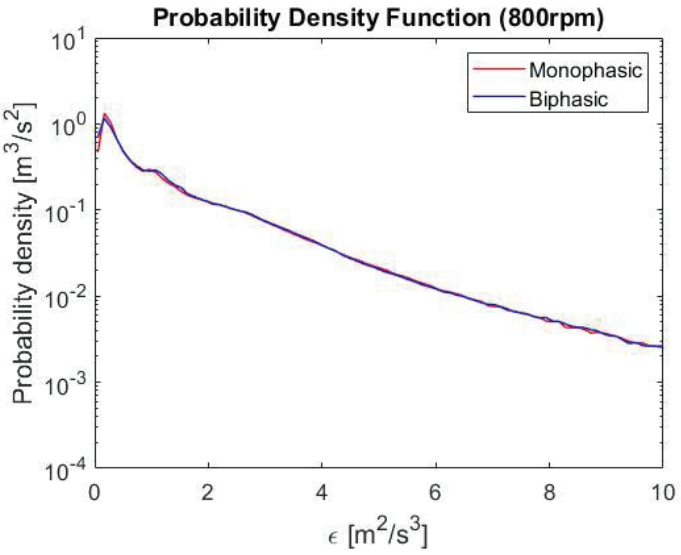


Figure 3.11: Example of the probability density functions of ε obtained through a single (red) and a two (blue)-phase simulation of the STR at 800rpm.

For this reason, it was assumed that at relatively low dispersed phase volume fraction, the turbulence of the two-phase flow could be approximated by running single-phase CFD simulations. Since, as it will be shown in the next chapter, the experiments both for the STR and the pulsed column were performed at low dispersed phase volume fractions, single-phase CFD simulations were run to extract the probability density functions of ε. Nevertheless, why this assumption seems valid at low dispersed-phase volume fractions, it would be necessary to evaluate if at higher ones the approximation still holds.

4. Turbulence inhomogeneity

4.1. Volume-averaged turbulent dissipation rate ε

The breakage and coalescence rates are estimated by models which are functions of the fluid properties (surface tension, density, sometimes viscosity) and of the flow regime, generally according to fully turbulence assumption. Hence, the kernels strongly depend on the turbulent kinetic energy dissipation rate, ε. Many authors [8–11], in the solution of a 0D PBE model (Eq. 2.5), assumed the turbulence to be uniform in liquid-liquid contactors and employed a uniform, *mean* value of ε in their calculations. Unfortunately, the reality is not as simple. Indeed, large variations of ε generally prevail in a given liquid-liquid contactor, with zones where the dissipation is elevated (promoting higher breakage than predicted by the average value) and others where it is null. For the sake of illustration, the ε distributions in a stirred tank reactor provided by a Mixel TT impeller and in a compartement of the pulsed column are compared in Fig. 4.1.

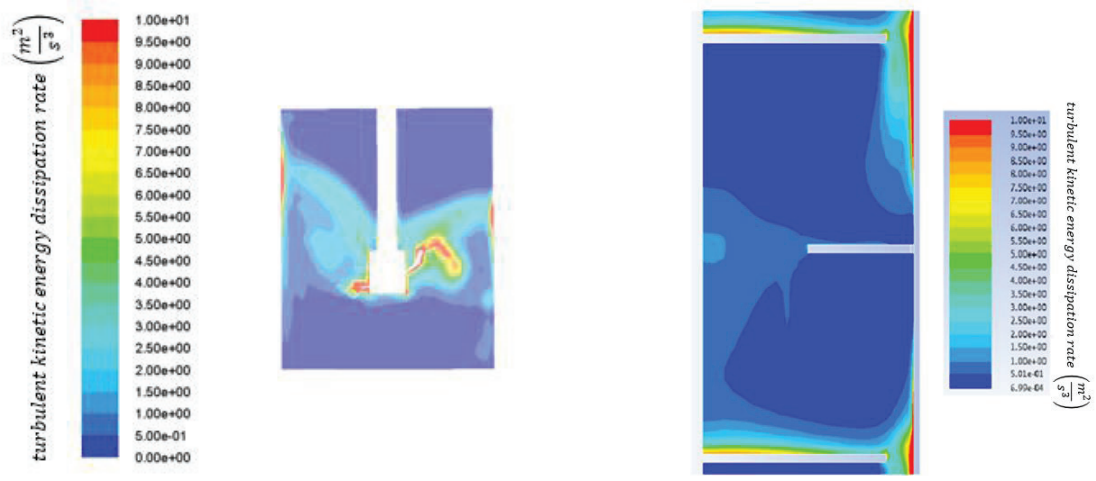


Figure 4.1: Turbulent kinetic energy dissipation rate distribution (same volume-average value, i.e. ε = 1) in a stirred tank reactor employing a Mixel TT impeller and in a pulsed column

In the stirred tank (Fig. 4.1, left), ε is high near the impeller and the walls, while it is almost zero everywhere else. In the pulsed column (Fig. 4.1, right), the highest values of ε are observed in the gap between the wall and the packing elements.

The difficulty in considering the ε inhomogeneities in a 0D PBE model are caused by the three-dimensionality of turbulence. The methods proposed in the literature to overcome this problem are detailed and discussed.

4.2. Compartment method

A simplified hydrodynamic description in the PBE has been implemented by Alopaeus [72], who divided the domain of the liquid-liquid contactor in subdomains where the value of ε can be considered to be uniform, and solved the population balance equation for each of these subdomains. While this method allows to account for the turbulence inhomogenities in a 0D model, its drawbacks reside in the definition of the subdomains and in the computation of the droplet fluxes among the latter.

In the case of a stirred tank reactor employing a Rushton turbine, where the turbulence inhomogeneities are concentrated in the proximity of the stirrer, the subdomains can be easily defined to account for zones with similar values of ε (Fig. 4.2).

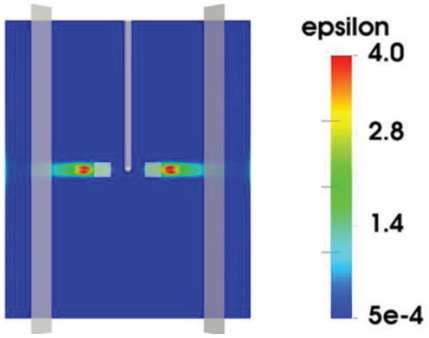


Figure 4.2: Turbulent kinetic energy rate dissipation distribution in a stirred tank reactor employing a Rushton turbine (ε=0.5)

However, for more complex configurations, as in the case of the pulsed column or a stirred tank reactor employing a helix, the subdomain definition is more tedious due to the spread distribution of turbulence. Moreover, the subdomains exchange droplet fluxes, whose quantification is not trivial and requires to model the droplets motion in the liquid-liquid contactor.

4.3. Volume-averaged kernels

4.3.1. Population Balance Modelling

As discussed in Sec. (2.1), the approach proposed by Buffo et al. [20,22] was applied to the general 3D PBE to get a simplified 0D PBE model:

$$\frac{\partial \bar{n}(v,t)}{\partial t} = \int_v^{\infty} \beta(v|v') \frac{1}{V} \int_{\boldsymbol{x}} \Gamma(\boldsymbol{x},v) d\boldsymbol{x}\, \bar{n}(v',t) dv' - \bar{n}(v,t) \int_0^{\infty} \frac{1}{V} \int_{\boldsymbol{x}} \mathrm{Q}(\boldsymbol{x},v,v') d\boldsymbol{x} \bar{n}(v',t)\, dv'$$
$$-\bar{n}(v,t) \frac{1}{V} \int_{\boldsymbol{x}} \Gamma(\boldsymbol{x},v) d\boldsymbol{x} + \frac{1}{2} \int_0^{v} \frac{1}{V} \int_{\boldsymbol{x}} \mathrm{Q}(\boldsymbol{x},v-v',v') d\boldsymbol{x}\, \bar{n}(v-v',t) \bar{n}(v',t) dv' \tag{2.4}$$

In order to account for the turbulent inhomogeneities in the 0D PBE model of Eq. 2.4, Buffo et al. proposed to compute the volume-averaged kernels through the probability density function of the turbulent dissipation rate, $f(\varepsilon)$, as follows:

$$\bar{\Gamma}(v) = \frac{1}{V} \int_V \Gamma(\boldsymbol{x},v) d\boldsymbol{x} = \int_0^{\infty} \Gamma(\varepsilon,v) f(\varepsilon) d\varepsilon, \tag{4.1}$$

$$\bar{Q}(v,v') = \frac{1}{V} \int_V Q(\boldsymbol{x},v,v') d\boldsymbol{x} = \int_0^{\infty} Q(\varepsilon,v,v') f(\varepsilon) d\varepsilon. \tag{4.2}$$

where $f(\varepsilon)$ can be evaluated through a detailed CFD simulation.

The reader should note that this 0D model presents the advantage of accounting for the influence the turbulent non-uniformities have on the breakage and coalescence rates in a 0-dimensional frame, with significant reduction of the computational time, compared to fully coupled CFD-PBM simulations. However, it is worth remarking that this method is applicable only when the NDF is spatially uniform, namely in dilute systems at low volume fractions of the disperse phase and at high stirring rates [20].

Moreover, it is important to mention that the most widely adopted approach in the literature considers instead a volume-averaged turbulent kinetic energy dissipation rate, $\bar{\varepsilon}$, as

done by Coulaloglou and Tavlarides [10] to determine the parameters of their model. The reader should note that this approach, unlike the 0D method using the PDF of ε adopted in this work, does not account for the turbulent inhomogeneities in the apparatus. This means that, for example, experiments performed in different vessels, characterized by a completely different flow and turbulent fields and giving rise to very different DSDs, but resulting in the same volume-averaged turbulent dissipation rates, would result in identical predicted DSD evolutions.

4.3.1.1. Breakage and Coalescence kernels

Many models for breakage and coalescence kernels have been proposed in literature [12,14]. The Coulaloglou and Tavlarides kernels [10] remain the most widely used due to their simplicity and fundamental basis. Amokrane et al. [17] showed that Coulaloglou and Tavlarides kernels allow quite good fits to experimental data on emulsions performed in stirred tank reactors and pulsed columns, though with a need to refit the four parameters (when changing the apparatus or the emulsion itself (which is usually the case for other kernels too). For this reason, Coulaloglou and Tavlarides models are considered in this work. These kernels have been discussed in Sec. (2.4.1).

4.3.1.2. Numerical solution of PBE

The Fixed Pivot method, detailed in Sec. (2.2.1.1), was selected to solve the 0D PBE model and implemented in a Matlab routine. The set of ordinary differential equations were solved using the ode15s function. The parameter identification was carried out using the pattern-search function (Global optimization toolbox of MATLAB). It took approximately 15 minutes on an Intel Xeon dual-core machine (3.20 GHz) with 64GB of RAM. Instead, to reproduce the evolution in time of the Sauter mean diameters for an emulsification experiment, once the parameters had been identified and the probability density function of ε had been implemented, the Matlab simulation took approximately 1 minute.

4.3.2. Materials and methods

4.3.2.1. Materials

Distilled water and Isane 175, provided by TOTAL, were used to prepare the emulsions. Isane 175 is a mixture of aliphatic and aromatic compounds with 12 to 14 carbon atoms. The physical properties of the liquids are given in Table 4.1.

Table 4.1: properties of water and Isane employed in the emulsification experiments

Product \ property	density (ρ, kg/m^3)	viscosity (μ, Pa.s)	surface tension (N/m)
Water	997.8	0.001	0.0383
Isane	762	0.0012192	

No surfactant was used to stabilize the emulsion; therefore, the surface tension is quite high. Both oil-in-water, at 1-2% volume fraction of Isane hold-up, and water-in-oil, at 1% volume fraction of water hold-up, dispersions were considered.

The emulsification experiments were performed in the 1-L stirred tank reactor, whose characteristics have been described in Chap. 3. A 3-blade Mixel TT impeller has been employed (impeller diameter, D = 60 mm), located at 40 mm from the bottom of the reactor (H/3) characterized by a power number of Np = 0.81 for high Reynolds numbers [57].

4.3.2.2. Experimental procedure

The experiments were carried out at different impeller rotational speeds (600-700-800 rpm) and hold-ups (1-2%). Both oil-in-water and water-in-oil dispersions were considered.

The experimental protocol consisted in filling the reactor with the required amounts of Isane and water (according to the required hold-up) and starting to stir at the required agitation speed. To monitor the droplet size distribution in the reactor, an endoscopic photo-optical device was employed (SOPAT® system). For each experiment, after 10 minutes from the start of the stirring, a first set of images was acquired to determine the initial drop size distribution.

Then, the acquisition was repeated at different instants to obtain the DSD time evolution. The determination of the droplet size distributions from the acquired images was performed through image-processing software provided by SOPAT® (Fig. 4.3).

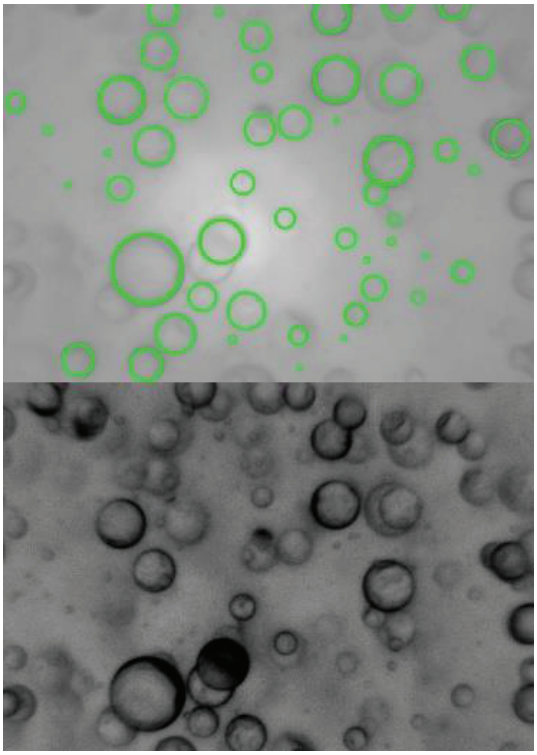


Figure 4.3: Example of image treated through the SOPAT software. The half bottom image represents the photographed droplets. The half upper, the detected ones, enlightened by green circles.

For each acquisition, which lasted 60 s, with 5 images captured per second, the consistency of the number of the detected particles was checked, with regard to statistical relevance of the DSD [73]. From the DSD, the droplet Sauter mean diameter was computed as follows:

$$d_{32} = \frac{\int_0^\infty d^3 n(d) d(d)}{\int_0^\infty d^2 n(d) d(d)} \tag{4.3}$$

The Sauter mean diameter is expressed as the ratio between a term proportional to the total droplet volume (third moment of the distribution), which is constant, and a term proportional to the interfacial area (second moment of the droplet size distribution), which

changes continuously as a result of droplet breakage and coalescence. Therefore, the higher the Sauter mean diameter, the lower will be the interfacial area between the two phases. This parameter is thus of great importance because it allows computation of the interfacial area, which is particularly useful when mass transfer occurs between the phases.

4.3.2.3. CFD model

The probability density function of the turbulent kinetic energy dissipation rate, ε, was obtained through CFD simulations using Ansys FLUENT®. Single phase simulations were run, assuming the effect of the dispersed diluted phase (1-2%) on the flow to be negligible.

The full 3D stirred tank reactor was meshed using Ansys Meshing. The mesh is unstructured and constituted of approximatively 2,000,000 tetrahedral cells, with an average orthogonal quality of 0.89 and a minimum of 0.25.

In the simulations, the Multiple Reference Frame (MRF) technique was used to model the stirrer motion. The 3D stirred tank reactor was then divided into two cell zones: the first zone enclosing the fluid domain near the impeller, which directly experiences the stirrer motion (whose rotational speed is imposed as cell-zone condition); the second zone enclosing the remaining part of the fluid domain. At the interface between the two cell zones, the momentum fluxes are computed through appropriate mathematical transformation [65]. The MRF technique represents a good compromise between accuracy and computational costs, compared with other detailed methods such as the Sliding Mesh method [67].

As far as the turbulence modeling is concerned, the RANS approach was used. In particular, the standard k-epsilon model with enhanced wall treatment function was employed.

From preliminary steady–state CFD simulations, the convergence criteria, based on the absolute residual for each solved equation (set at 10^{-6}), were not reached. Therefore, transient simulations were run to obtain the probability density function of the turbulent dissipation rate. These simulations were run until the volume-averaged value of the turbulent dissipation rate was constant. This operation took approximately 5 hours on an Intel Xeon dual-core machine (3.20 GHz) with 64GB of RAM: this time is considerably lower than the one required to perform a CFD-PBE simulation of the stirred tank reactor. Indeed, a CFD-PBE simulation

requires the solution of additional equations, whose number depends on the method adopted for the PBE solution. Therefore, the CFD-PBE simulation may take several days to fully reproduce an emulsification experiment.

The time was discretized through a second order implicit method. The time step was set between 0.0002 s and 0.00025 s, according to the rotation speed of the moving cell zone. This time step allowed the convergence criteria to be reached in 15-20 iterations. Pressure, momentum, turbulent kinetic energy and turbulence dissipation rate were discretized through a second order upwind method. Pressure-velocity coupling was treated through the SIMPLE scheme.

4.3.3. Results and discussions

4.3.3.1. CFD simulation results

The probability density functions of the turbulent dissipation rate were determined through single-phase CFD simulations, employing either water or Isane alone at different rotation speeds. As expressed in Sec. 4.3.2.3, the transient simulations were run until a constant value of the volume-averaged turbulent dissipation rate was reached.

The probability density functions obtained for each operating condition at different rotational speeds were compared (Fig. 4.4).

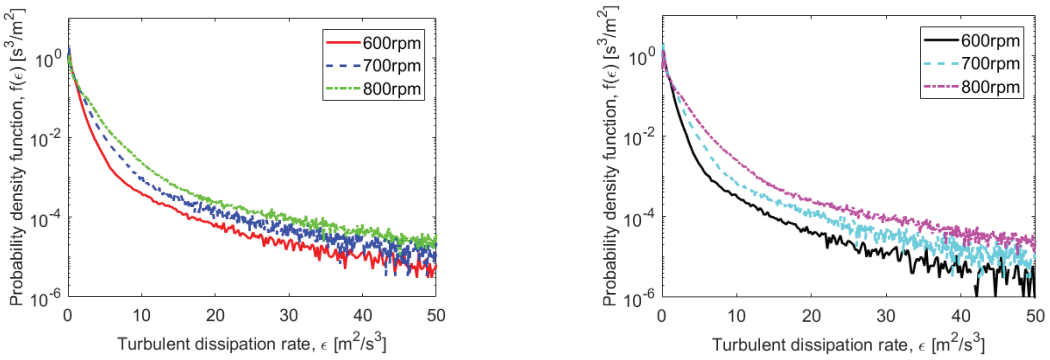


Figure 4.4: Probability density functions, f(ε) for water (left) and Isane (right) at different impeller rotational speeds (600-700-800rpm).

As expected, for both phases, higher impeller rotational speeds lead to higher probability that several fluid elements experience higher values of the turbulent dissipation rate. Indeed, it can be seen for instance that while stirring at 600 rpm, the probability of high turbulent energy dissipations is relatively low. Also, the probability density functions obtained for water and the ones obtained for Isane are similar (Fig. 4.5).

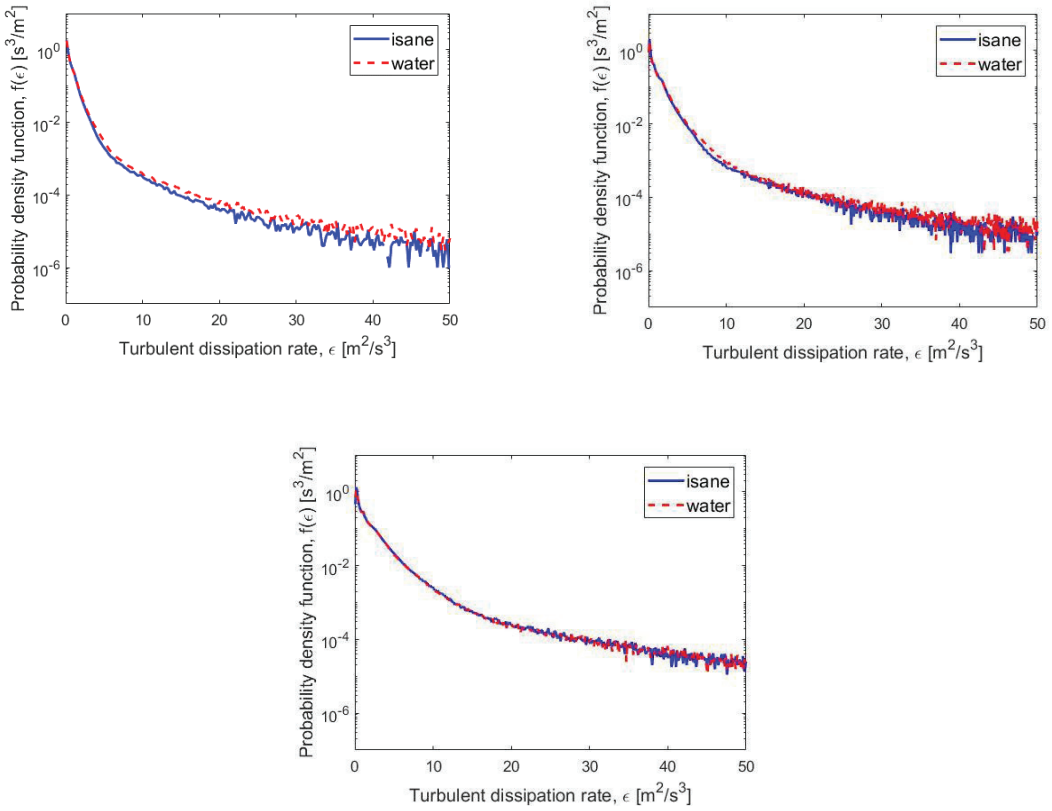


Figure 4.5: Comparison of the probability density functions for Isane and water at 600rpm (top-left), 700rpm (top-right), 800rpm (bottom).

This is because these products have quite similar viscosities, but differ in density, thus leading to similar dissipation of turbulent kinetic energy. Slight differences are present in the two functions at 600 rpm and 700 rpm, but at 800 rpm are almost identical. Both the functions obtained with water and those obtained with Isane will be used in parameter identification and model validation at the different conditions.

The volume average value of the turbulent dissipation rate in a stirred tank reactor can be computed as function of the power number (N_p) and geometrical and operating conditions:

$$\bar{\varepsilon} = \frac{P}{m_r} = \frac{N_p N^3 D^5}{V_r} \tag{4.5}$$

According to Eq. 4.5, the volume-averaged value of the turbulent dissipation rate depends on the volume of fluid present in the reactor, but not on the properties of the liquid (i.e. viscosity and density), provided that the power number (N_p) of the impeller is constant.

The final volume-averaged values of the turbulent dissipation rates reached in the CFD simulations were found to be very similar to the ones computed using Eq. 4.5 (see Tab. 4.2).

Table 4.2: Averaged turbulent dissipation rates $\bar{\varepsilon}$ (m^2/s^3) according to correlation (eq. 4.5) and by CFD simulations (water-isane)

Method \ stirring rate	**$\bar{\varepsilon}$ at 600 rpm**	**$\bar{\varepsilon}$ at 700 rpm**	**$\bar{\varepsilon}$ at 800 rpm**
Averaged $\bar{\varepsilon}$ (Eq. 4.5)	0.63	1.01	1.47
CFD (using water as continuous phase)	0.64	1.01	1.50
CFD (using Isane as continuous phase)	0.61	0.99	1.49

However, slightly different turbulent dissipation rates were predicted employing water or Isane. The small differences may be explained considering changes in the power number, which is proportional to the turbulent dissipation rate. Indeed, the power number of an impeller is constant for high Reynolds numbers (more than 10^5), but it varies at lower Reynolds numbers [55]. Since both Isane and water continuous-phase experiments are characterized by Reynolds numbers lower than 10^5 (Tab. 4.3), the predicted turbulent dissipation rates may differ.

Table 4.3: Reynolds numbers for Isane continuous-phase experiments (first row) and water continuous-phase experiments (second row) at different rotational speeds of the impeller.

Phase \ Reynolds number	600 rpm	700 rpm	800 rpm
Isane	22500	26500	30000
Water	36000	42000	48000

This supposition is also confirmed by the fact that, as the rotational speed of the impeller increases (and consequently the Reynolds number), the volume-averaged turbulent dissipation rates tend to the same values (Tab. 4.2). Nevertheless, it is important to point out that the spatial distribution of the turbulent dissipation rate is far from being uniform in the reactor (Fig. 4.6).

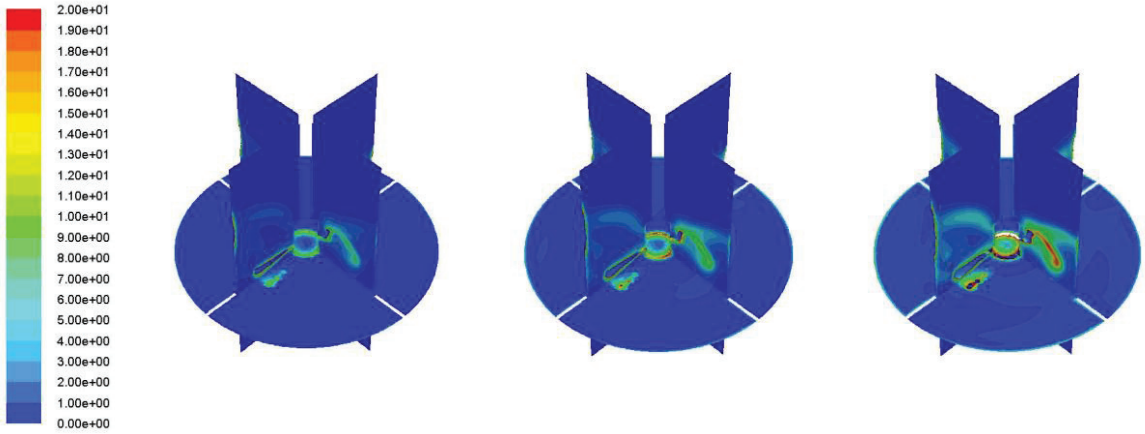


Figure 4.6: Space distributions of the turbulent dissipation rate, ε (m^2/s^3), at 600 rpm (left), 700rpm (center), 800 rpm (right) according to water-phase CFD simulation.

This property has high values in the proximity of the impeller, while it is lower in the recirculation zone. According to the division of the reactor in two different cell zones as reported in Sec. 4.2.3.2, the volume-averaged turbulent dissipation rate experienced by the fluid in the cell zone enclosing the impeller is 4-5 times the one experienced by the fluid in the rest of the reactor (Tab. 4.4).

Table 4.4: Volume-averaged turbulent dissipation rates $\bar{\varepsilon}$ (m^2/s^3) in the recirculation zone, in the impeller zone and in the total volume for water-phase CFD simulations.

Stirring rate \ zone	$\bar{\varepsilon}$ in the impeller zone	$\bar{\varepsilon}$ in the recirculation zone	$\bar{\varepsilon}$ in the reactor
600 rpm	2.17	0.51	0.64
700 rpm	3.37	0.83	1.01
800 rpm	5.19	1.21	1.51

4.3.3.2. Oil in water emulsions

As reported in Sec. 4.3.2.2, several emulsification experiments were performed changing the impeller rotational speed (600 to 800 rpm), the hold-up (1-2%) and inverting the continuous and disperse phases (Isane and water).

The experiments performed with water as continuous phase and 1-2% Isane hold-up showed that higher impeller rotational speeds lead to the generation of smaller droplets (Fig. 4.7). This is due to the higher input energy fed to turbulent eddies which causes higher velocity and pressure fluctuations that lead to the droplet breakage. However, while the difference between the droplet sizes obtained with 600 and 700 rpm stirring rate is quite high, the difference between 700 and 800 rpm stirring rate is much lower, indicating a hydrodynamic equilibrium between breakup and coalescence.

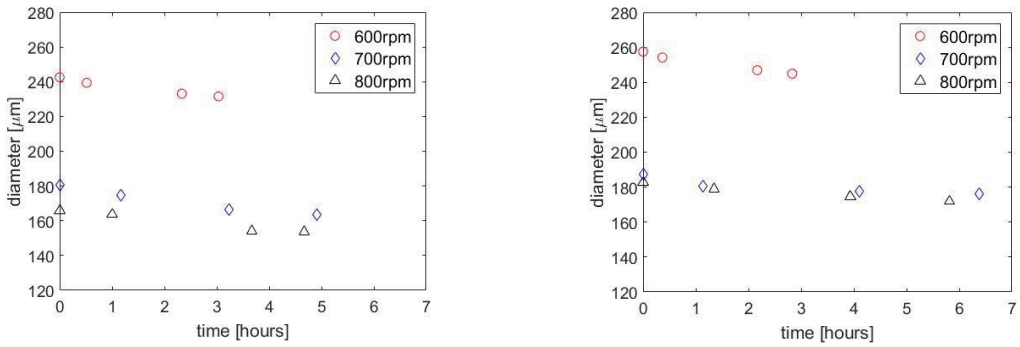


Figure 4.7: Time evolution of the droplet Sauter mean diameters for oil-in-water experiments at 1% (left) and 2% (right) volume fraction of Isane hold-up and 600rpm, 700rpm and 800rpm.

It is also interesting to point out that the higher the hold-up of the dispersed phase, the bigger the Sauter mean diameter at the same impeller rotational speed. Indeed, higher Isane volume fraction increases the number of droplets present in the reactor, and therefore enhances the probability that two droplets collide and coalesce.

4.3.3.3. Water in Isane emulsion

The second set of experiments was performed employing Isane as continuous phase and 1% water hold-up. As in the previous case, smaller droplets were formed when the agitation in the reactor was higher (Fig. 4.8).

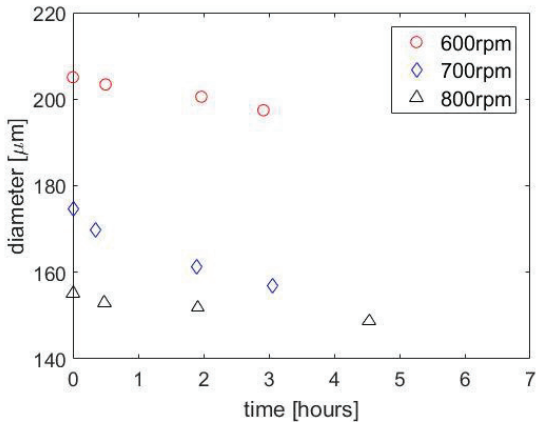


Figure 4.8: Time evolutions of the droplet Sauter mean diameters for the water-in-oil experiments at 1 % volume fraction of water hold-up and 600rpm, 700rpm and 800rpm.

A comparison between the direct oil-in-water emulsion with the inverse emulsion is shown in Fig. (4.9). Under the same stirring rate, water droplets were smaller than Isane droplets for stirring rates of 600 and 700 rpm. However, at 800 rpm stirring rate, both the direct and inverse emulsion led to similar droplet sizes of the disperse phase.

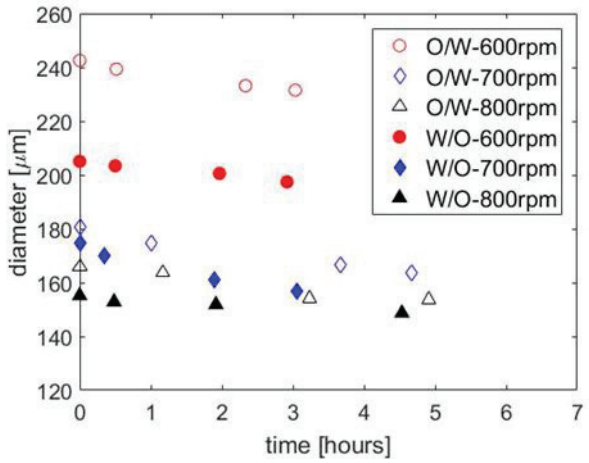


Figure 4.9: Time evolutions of droplet Sauter mean diameters for oil-in-water (empty) and water-in-oil (plain) experiments at 1% dispersephase hold-up and at 600rpm (red) 700rpm (blue) and 800rpm (black) rotational speeds.

4.3.3.4. Identification of parameter values

The identification of the Coulaloglou and Tavlarides model parameters [10] was performed through the oil in water experiments at 600 rpm and 1-2 % volume fraction of Isane hold-up. The parameters were determined implementing the probability density functions of the turbulent dissipation rate obtained at 600 rpm and water as continuous phase. The volume-averaged kernels were computed approximating the integrals of Eq. 4.1 and Eq. 4.2 by a classical numerical integration method:

$$\bar{\Gamma}(v) = \int_0^\infty \Gamma(\varepsilon, v) f(\varepsilon) d\varepsilon \approx \sum_{i=1}^{\infty} \Gamma(\varepsilon_i, v) f(\varepsilon_i) \left(\varepsilon_{\frac{i+1}{2}} - \varepsilon_{\frac{i}{2}} \right) \tag{4.6}$$

$$\bar{Q}(v, v') = \int_0^\infty Q(\varepsilon, v, v') f(\varepsilon) d\varepsilon \approx \sum_{i=1}^{\infty} Q(\varepsilon_i, v, v') f(\varepsilon_i) \left(\varepsilon_{\frac{i+1}{2}} - \varepsilon_{\frac{i}{2}} \right) \tag{4.7}$$

where $\Gamma(\varepsilon_i, v)$ and $Q(\varepsilon_i, v, v')$ are the breakage and coalescence kernels evaluated for $\varepsilon = \varepsilon_i$ and $f(\varepsilon_i)$ is the probability density value of ε_i extracted from the single-phase CFD simulation. Then, for the sake of comparison, these parameters were identified assuming a uniform value of the turbulent dissipation rate (0D PBE based on $\bar{\varepsilon}$ from Eq. 4.22).

The identification was carried out through a Matlab routine employing a global optimization procedure (*patternsearch* function). For each experiment, the function to be optimized was the sum of the square differences between the simulated Sauter mean diameters, computed with a certain set of parameters, and the values obtained experimentally. A good fitting of the experimental data was reached with both methods (see Fig. 4.10).

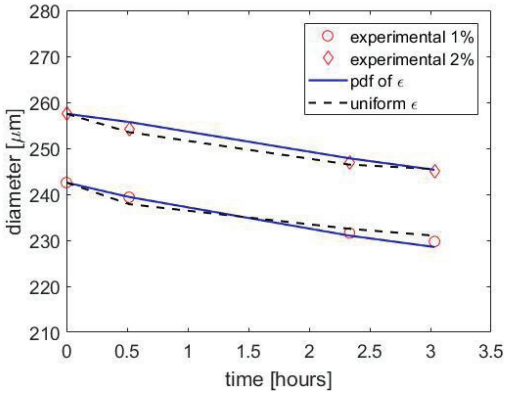


Figure 4.10: Parameters identification on oil in water experiments at 1% (circles) and 2% (rhombus) of Isane hold-up employing the pdf (blue) or assuming a uniform value (black) of ε.

However, the two sets of identified parameters differ (Tab. 4.5). It can be seen that when a uniform turbulent dissipation rate, $\bar{\varepsilon}$, is used, the identified breakage and coalescence parameters are respectively higher and lower than those obtained when employing the probability density function of ε. Indeed, this latter method accounts for the high values of the turbulent dissipation rate, which causes high breakage frequency, thus requiring lower values of the corresponding parameters.

Table 4.5: Identified parameters for the Coulaloglou and Tavlarides kernel employing the pdf of ε or assuming a uniform value.

	Breakup		**Coalescence**	
	C_1	**C_2**	**C_3**	**C_4**
PDF of ε	1.20×10^{-3}	7.11×10^{-1}	1.95×10^{-2}	2.05×10^{14}
Uniform ε	7.84×10^{-2}	3.06×10^{-1}	3.75×10^{-4}	8.23×10^{18}

4.3.3.5. Validation of parameter values

The two sets of identified parameters (using the pdf of ε, and volume-averaged $\bar{\varepsilon}$) in the selected experiments of Sec. 4.3.3.3 (at 600 rpm and using water as continuous phase, with different isane hold-ups) were tested with the experiments performed at higher impeller rotation speeds (700-800 rpm) as well as when inverting the phases (water-in-oil emulsion). The objective is to evaluate the accuracy of the model in cases of different turbulent conditions and breakage and coalescence rates (being these latter function of densities and viscosities of continuous and disperse phases), and to determine which set of parameters is more adequate, thus to decide which method between the one based on the pdf of ε and the one using $\bar{\varepsilon}$ is more generalizable to other apparatus or emulsification systems.

The first simulations dealt with the fitting of the experimental data at 700-800 rpm and 1-2 % volume fraction of Isane hold-up. For the four experiments (Fig. 4.11), the droplet Sauter diameters predicted employing the parameters identified with the homogeneous model with the probability density functions of the turbulent dissipation rate, are very similar to the experimental ones.

This is not the case for the model results obtained using the parameters identified assuming the turbulent dissipation rate to be uniform (traditional method). The error obtained with this method seems to increase when the turbulence and the hold-up are higher. Indeed, the better hydrodynamic description given by the new model allows the transposition of the parameters for different turbulent conditions.

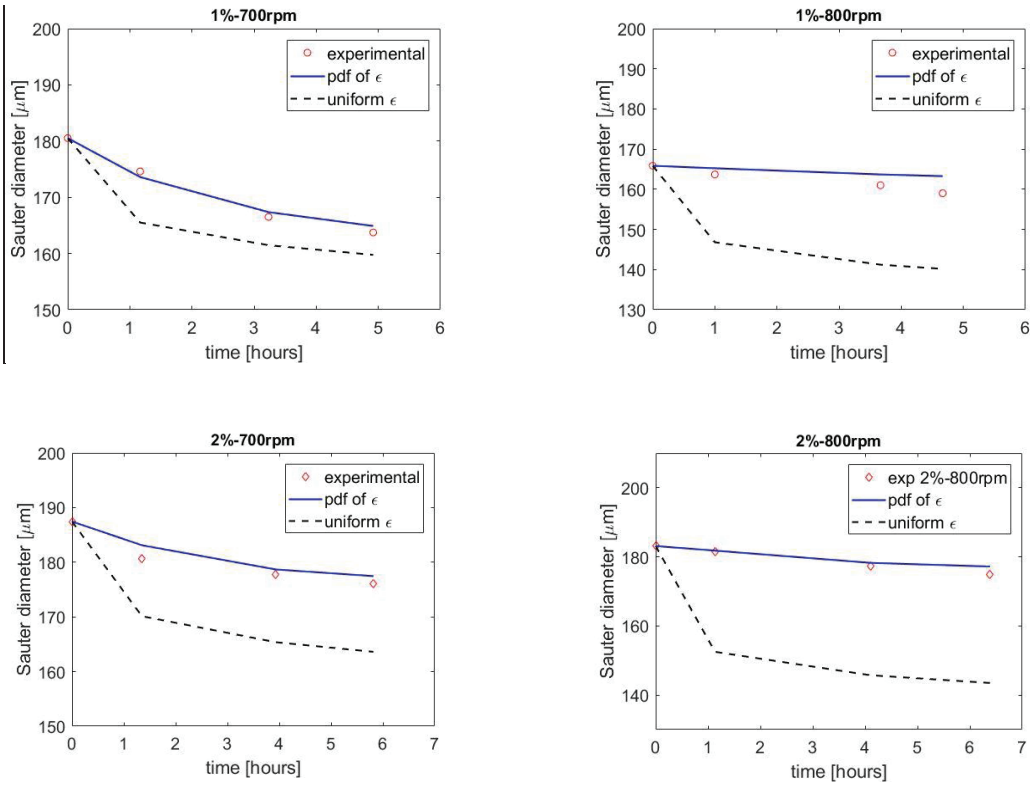


Figure 4.11: Parameters testing on oil-in-water experiments at 1-2 % of Isane hold-ups employing the pdf or assuming a uniform value of ε.

The second part of the parameter validation dealt with the experimental data obtained for the inverse emulsion, with water hold-up of 1%. As in the previous case, the parameters identified with the new method along with the probability density functions of the turbulent dissipation rate gave better predictions than with the traditional method (Fig. 4.12). This demonstrates that the parameters obtained with the new model are generalizable to different hydrodynamic and chemical-physical conditions.

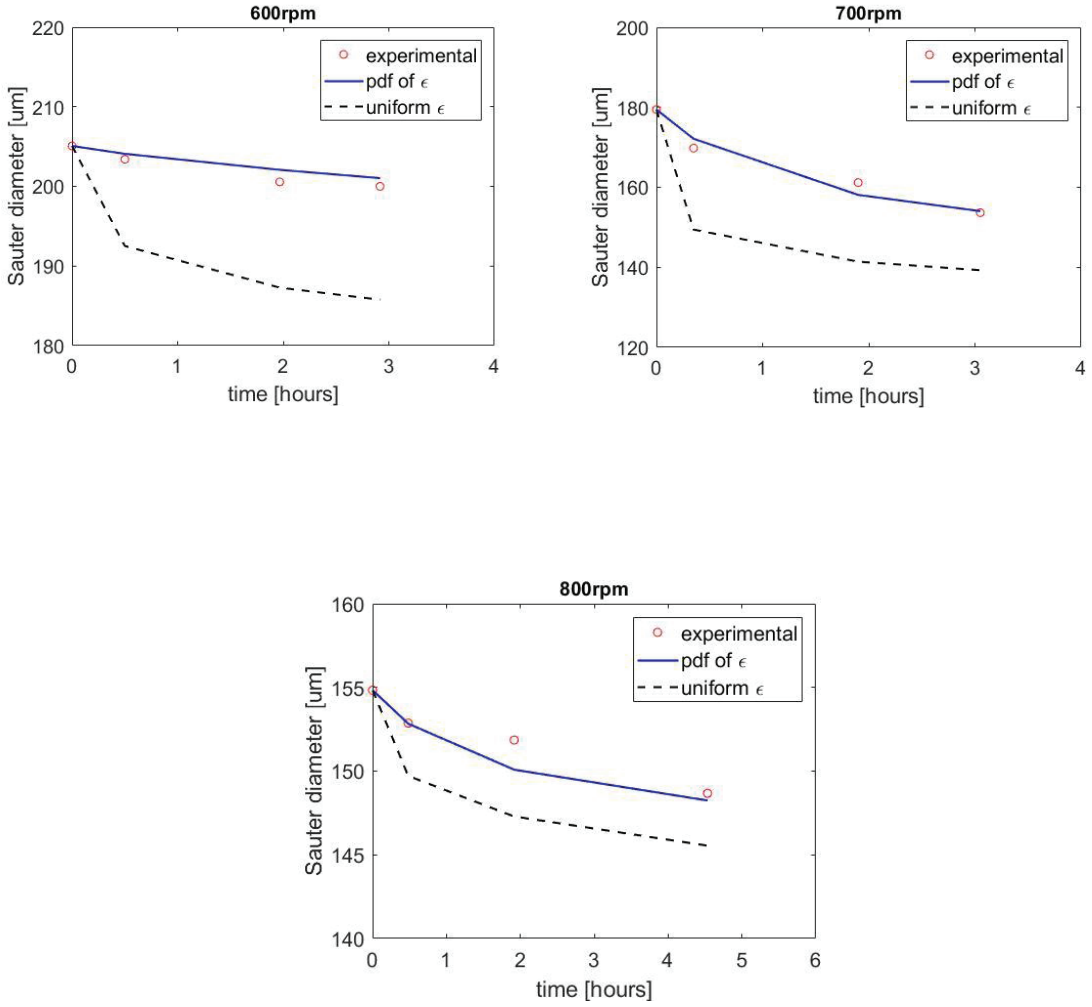


Figure 4.12: Parameters testing on oil-in-water experiments at 1% volume fraction of water hold-up employing the pdf or assuming a uniform value of ε.

4.3.4. Conclusions

A 0D homogenous method that takes into account the non-uniformity of the turbulent kinetic energy dissipation rate, without employing a 3D description of the hydrodynamic (nor CFD-PBE coupling, or compartmentalization), was used for predicting the behavior of the Sauter mean diameter in a real liquid-liquid experiment. This method is based on the use of the probability density function of the dissipation rate ε into the population balance model, allowing the computation of a volume-averaged kernel, rather than using a volume-averaged value of this property as usually done in traditional 0D methods. With this methodology it was possible

to evaluate the model parameters for the droplet coalescence and breakage models to be used to reproduce the experimental data under a wide range of operating condition.

The method (based on the pdf of ε) appeared to be more accurate than the traditional method (based on $\bar{\varepsilon}$). Indeed, the traditional 0D method represented a rough approximation of the real energy dissipation, since this property is far from being uniform in the apparatus.

Parameters identification was performed using the experiments at 600 rpm and 1-2 % volume fraction of Isane in water, by employing both methods, through a global optimization algorithm. Later, the identified parameters for the two models were tested for new experimental data obtained at higher rotational speeds (700-800 rpm, 1-2 % volume fraction hold-up) as well as considering phase inversion (water-in-Isane, 1 % volume fraction hold-up). The model assuming a uniform turbulent dissipation rate failed to predict the Sauter mean diameters when the operating conditions were modified. The non-uniformity in the apparatus is indeed important and cannot be approximated through a uniform value of the turbulent dissipation energy. Instead, the model based on the computation of the volume-averaged kernel predicted the values of the Sauter diameter which fit accurately the experimental data, even when the hydrodynamic conditions were varied and when the emulsion was inversed. This indicates that the obtained parameters would be more generalizable to different geometries of the system, stirring rates and disperse phase volume fraction.

5. Improved kernel turbulence

The previous part of the work allowed the validation of a model which permitted to account for the turbulence inhomogeneities in a 0D PBE through the computation of volume-averaged kernels. Since, during the PUREX process, the transfer of uranium and plutonium oxides to the organic phase leads to an increase of the viscosity of the latter, experiments at higher viscosity were performed. The obtained experimental data were not well represented through the validated model, indicating the necessity to adapt the kernel to a wider range of turbulence.

One of the most important assumption in the kernels proposed in the literature is that the droplets have dimensions in the inertial subrange of turbulence, where the results of the Kolmogorov theory are valid. Therefore, in this section, it is shown that at higher viscosity, the droplets have dimensions which are mainly in the dissipation subrange of turbulence, where the continuous phase viscosity is not negligible. The kernels are therefore modified in this chapter to account for the entire turbulence spectrum, through the implementation of a generalized second order structure function and of complete energy spectrum.

5.1. Generalized second-order structure function

Most of the kernels proposed in the literature address the coalescence and breakage of droplets having dimensions in the inertial subrange of turbulence (Sec 2.3). This means that the size of the droplets involved in the turbulent liquid-liquid dispersion must obey: $d > l_{DI}$ (the limit boundary between the inertial and the dissipation subrange), where [44]:

$$l_{DI} \approx 60\eta. \tag{5.1}$$

However, it is possible that a significant number of the dispersed droplets do not have size in this subrange, and that the turbulent stresses to which they are subjected depend both on ε and ν. If so, the assumption of a second-order structure function according to Eq. 2.32 in the breakage definition could lead to erroneous breakage and coalescence rates. Indeed, when this function is applied to the dissipation subrange, it overestimates the eddy energy, since this latter tends to zero due to viscosity dissipation effects (Fig. 5.1).

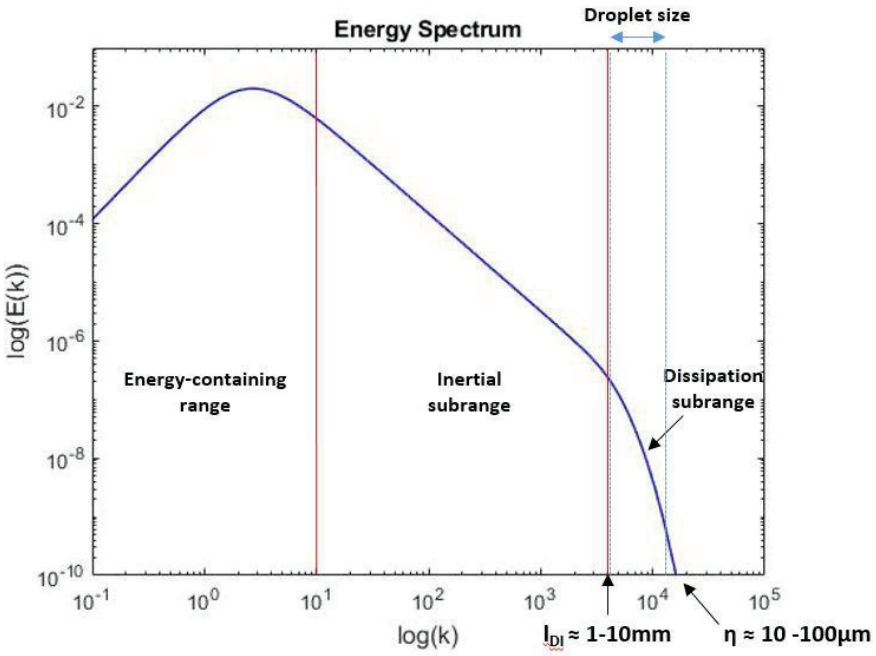


Figure 5.1: Energy spectrum representation of the eddies according to their wavelength in the energy-containing range and the inertial and dissipation subranges of turbulence.

As a result, a refined formulation for the second-order structure function is needed to predict correctly the droplet breakage and coalescence. Davidson [43] proposed a second-order structure function $\langle[\Delta u(r)]^2\rangle$ which is based on the cumulative contribution of the turbulent kinetic energy of the eddies of size smaller than r and of the enstrophy of eddies of size bigger than r:

$$\langle[\Delta u(r)]^2\rangle = (turbulent\ kinetic\ energy\ of\ eddies\ with\ size < r) + (enstrophy\ of\ eddies\ with\ size > r)$$

The author expressed this function as [43,74,75]:

$$\langle[\Delta u(r)]^2\rangle = \frac{4}{3}\int_0^\infty E(\kappa) + 3E(\kappa)\left[\frac{\cos(\kappa r)}{(\kappa r)^2} - \frac{\sin(\kappa r)}{(\kappa r)^3}\right]d\kappa \qquad (5.2)$$

Eq. 5.2 requires the knowledge of the energy spectrum $E(\kappa)$, which gives the distribution of the turbulent kinetic energy across eddies of different sizes. In this work, the model proposed by Pope [44], for the whole energy spectrum, was employed:

$$E(\kappa) = C\varepsilon^{\frac{2}{3}}\kappa^{-\frac{5}{3}}\left(\frac{\kappa L}{[(\kappa L)^2 + c_L]^{\frac{1}{2}}}\right)^{\frac{11}{3}} \exp\left(-\beta\left\{\left[(\kappa\eta)^4 + c_\eta^4\right]^{\frac{1}{4}} - c_\eta\right\}\right) \tag{5.3}$$

where the parameters $C = 1.5$, $\beta = 5.2$ have been experimentally determined [2,21] and c_η, c_L are retrieved by enforcing the following definitions:

$$\begin{cases} \varepsilon - \int_0^\infty 2\upsilon\kappa^2 E(\kappa, c_L, c_\eta)d\kappa = 0 \\ k - \int_0^\infty E(\kappa, c_L, c_\eta)d\kappa = 0 \end{cases} \tag{5.4}$$

The Pope energy spectrum function accounts for both the energy-containing range, where the turbulence is anisotropic, and the universal range (that combines the inertial and dissipation subranges).

5.1.1. Breakage and Coalescence kernels

Following the definition of a more general expression for the second-order structure function in Sec. 5.1, the Coulaloglou and Tavlarides kernels [77] can be modified computing $\langle[\Delta u(d)]^2\rangle$ according to Eq. 5.2. The general expressions for the breakage and coalescence kernels are:

$$\Gamma(d) = C_1\frac{\sqrt{\langle[\Delta u(d)]^2\rangle}}{d}\exp\left(-C_2\frac{\sigma}{\rho_d d\langle[\Delta u(d)]^2\rangle}\right) \tag{5.5}$$

and:

$$Q(v,v') = C_3\sqrt{\langle[\Delta u(d)]^2\rangle + \langle[\Delta u(d')]^2\rangle}\left(v^{\frac{2}{3}} + v'^{\frac{2}{3}}\right)\left(v^{\frac{2}{9}} + v'^{\frac{2}{9}}\right)^{1/2}\exp\left(-\frac{C_4\mu_c\rho_c\langle[\Delta u(d+d')]^2\rangle^{\frac{3}{2}}}{\sigma^2}\left(\frac{v^{\frac{1}{3}}v'^{\frac{1}{3}}}{v^{\frac{1}{3}} + v'^{\frac{1}{3}}}\right)^4\right) \tag{5.6}$$

In this work, the second-order structure function is computed according to Eq. 5.2, in which the adopted energy spectrum expression is the one proposed by Pope (Eq. 5.3). It is worth remarking that, as in the original derivation of Coulaloglou and Tavlarides, the proposed generalized model presents four constant parameters (C_1, C_2, C_3, C_4) that are experimentally determined since they include all the modeling uncertainties [10,17,78].

5.2. Materials and methods

5.2.1. Materials

To validate the proposed model, liquid-liquid dispersion experiments were carried out at different dispersed phase volume fractions, and, more important, at different continuous phase viscosities. The increase in the viscosity leads to a bigger Kolmogorov microscale, and therefore, to a wider dissipation range.

Distilled water was employed as the dispersed phase, while the continuous phase was composed of different mixtures of Isane 175 and Marcol 82. Marcol 82 is a mixture of liquid saturated hydrocarbons provided by ExxonMobil. Isane 175 and water have similar viscosities, whereas Marcol 82 has a much higher viscosity. Therefore, the two oils were mixed at different volume fractions in order to achieve various continuous phase viscosities (Table 5.1). The experiments were performed in a stirred tank reactor (STR) of 1L volume described in Chap. 3, equipped with a 3-blades Mixel TT impeller, and 4 baffles to avoid vortex formation.

Table 5.1: Properties of Isane 175/Marcol 82 mixtures employed as solvents in the emulsification experiments.

Solvents		Physical-chemical properties		
Isane [%]	**Marcol [%]**	**μ (mPa.s)**	**ρ (kg/m^3)**	**σ (mN/m)**
100	0	1.219	757.4	38.30
0	100	12.347	850.8	41.20
70	30	2.249	783.4	38.21
55	45	4.102	799.9	39.81

In order to monitor the time evolution of the droplet size distribution (DSD), the Sopat® probe was inserted in the reactor. The collected images were then treated (Fig. 5.2) and analyzed through the software provided by the vendor to obtain the DSD and the Sauter mean diameter.

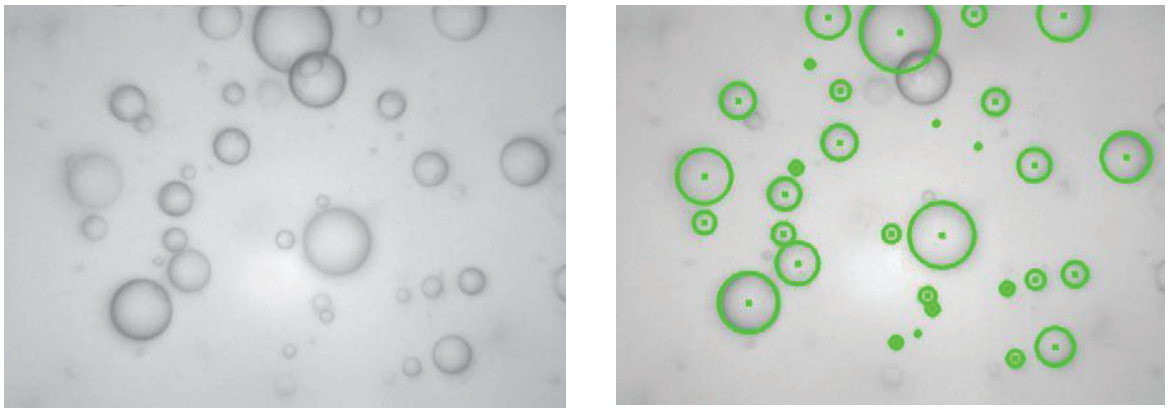


Figure 5.2: Droplet caption with the SOPAT® probe (left) and detection (right, green circles).

5.2.2. Experimental procedure

The experiments were performed at different oil viscosities (Table 5.1), dispersed phase volume fractions (1-2%), and impeller rotation speeds (600, 700 and 800 rpm).

The experimental procedure consists in filling the reactor with the desired fraction of the organic mixture and water. Then, stirring is started and the water-in-organic phase dispersion is created. After ten minutes of stirring, a first set of images is collected, representing the initial distribution of the experiment. Then, other sets of images are acquired, at regular time intervals, in order to assess the evolution of the DSD. Each acquisition lasted 60 seconds, with an image capturing rate of 5 Hz, for a total of 300 images. In average, each picture presented 10 droplets.

Since the interfacial area is the property of interest, the Sauter mean diameter was determined for each experimental DSD. The Sauter mean diameter of the droplet distribution decreases by a few tens of micrometers per hour in each experiment. Therefore, during the sixty seconds of the acquisition procedure, the droplet size distribution was considered in a quasi-steady state and the Sauter mean diameter constant.

5.2.3. 0D Population Balance Model

The 0D PBE model proposed by Buffo et al. [20], which considers a homogeneous NDF, was employed (Sec. 2.1):

$$\frac{\partial \bar{n}(v,t)}{\partial t} = \int_{v}^{\infty} \beta(v|v') \frac{1}{V} \int_{x} \Gamma(\boldsymbol{x},v) d\boldsymbol{x}\, \bar{n}(v',t) dv' - \bar{n}(v,t) \int_{0}^{\infty} \frac{1}{V} \int_{x} \mathrm{Q}(\boldsymbol{x},v,v') d\boldsymbol{x} \bar{n}(v',t)\, dv'$$
$$-\bar{n}(v,t) \frac{1}{V} \int_{x} \Gamma(\boldsymbol{x},v) d\boldsymbol{x} + \frac{1}{2} \int_{0}^{v} \frac{1}{V} \int_{x} \mathrm{Q}(\boldsymbol{x},v-v',v') d\boldsymbol{x}\, \bar{n}(v-v',t) \bar{n}(v',t) dv' \tag{2.4}$$

The volume-averaged kernels were computed through the probability density function of the turbulent dissipation rate ε as (Sec. 4.3.3.4):

$$\bar{\Gamma}(v) = \frac{1}{V} \int_{V} \Gamma(\boldsymbol{x},v) d\boldsymbol{x} = \int_{0}^{\infty} \Gamma(\varepsilon,v) f(\varepsilon) d\varepsilon \tag{4.1}$$

$$\bar{Q}(v,v') = \frac{1}{V} \int_{V} Q(\boldsymbol{x},v,v') d\boldsymbol{x} = \int_{0}^{\infty} Q(\varepsilon,v,v') f(\varepsilon) d\varepsilon \tag{4.2}$$

The Fixed Pivot Method, proposed by Kumar and Ramkrishna [24], was employed to solve the 0D PBE. The size domain is discretized in 40 arithmetic intervals $[v_i, v_{i+1}]$ in order to have a good compromise between computation time and convergence.

5.2.4. Numerical details

While the consideration of the entire energy spectrum of the turbulence allows a more refined description of the physics of the breakage and coalescence events, the volume-average kernel formulation [20] permits to better account for the turbulent inhomogeneity than using a volume-averaged turbulent dissipation rate [22]. The coupling of the two methods, therefore, allows to tackle two of the most insidious problems in the PBE model, with acceptable computation time.

Single-phase CFD simulations of the experimental stirred tank reactor were carried out for each experimental impeller rotation speed and each continuous phase viscosity. The $k-\varepsilon$ two-equation turbulence model was employed with an enhanced wall-treatment function. More information on the reactor mesh and the adopted discretization schemes have been reported in a previous work [22]. Each simulation took averagely 4 to 5 hours on an Intel Xeon dual-core machine (3.20 GHz) with 64GB of RAM. From each simulation, the probability density function of ε was extracted as a histogram constituted by 10000 bins. Each bin represented the probability of having a value of ε in the stirred tank reactor between ε_i and ε_{i+1}. For each interval $[\varepsilon_i, \varepsilon_{i+1}]$, the average ε was computed and employed in Eq. (5.3), which was later substituted in Eq. 5.2 to compute the second-order structure as a function of the droplet diameter. The integral of Eq. 5.2 was computed through the MATLAB function *integral*. This operation was repeated for each pivot of the PBE discretization (40 intervals) and the computed values were saved for later use in the PBE solution ("generalized model"). For each ε, the constants the Pope energy spectrum were found by solving the non-linear system of equations Eq. (5.4) with the MATLAB function fsolve, based on the Trust-Region Dogleg method. This first computation was run in MATLAB and took 15-20 minutes on an Intel Xeon dual-core machine (3.20 GHz) with 64GB of RAM. Finally, through the second-order structure functions computed previously, the MATLAB routine took approximately 1 minute to solve the PBE for

simulating 4 hours of real time. A schematic representation of the numerical procedure is given in Fig. 5.3.

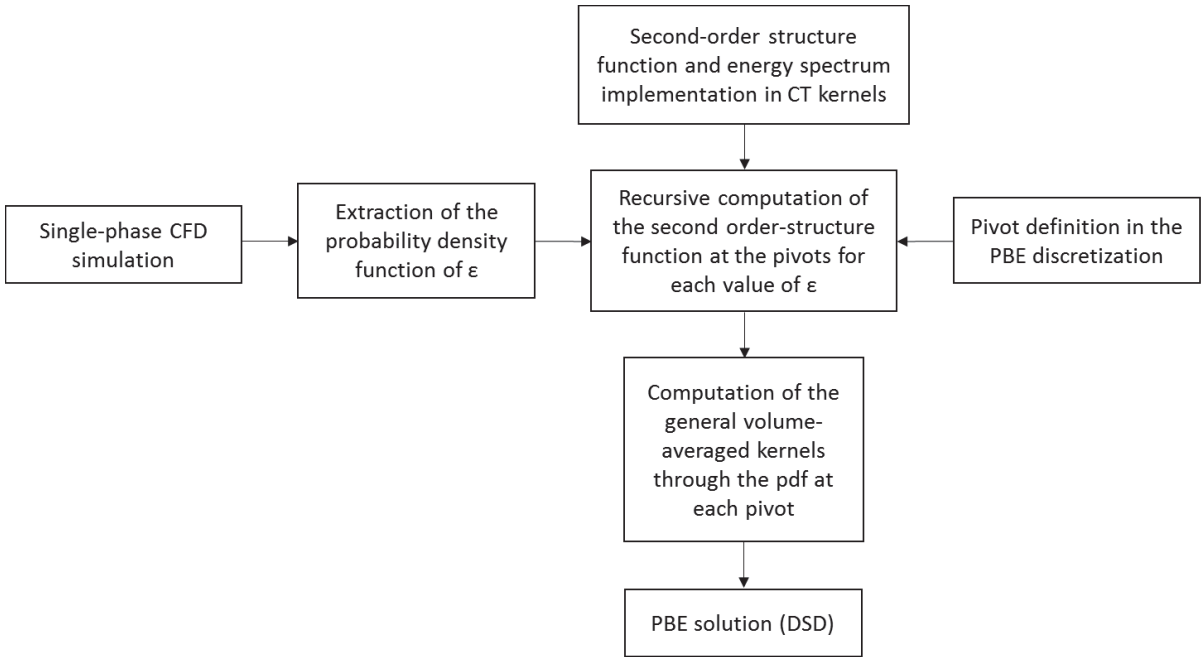


Figure 5.3: Main steps and sequence of the numerical procedure.

5.3. Results and discussions

As previously mentioned, the four constants of the proposed coalescence and breakage kernels need to be found for the system under investigation. Therefore, parameters identification was first performed using a numerical optimization procedure, based on a given set of experimental data. Then, using these parameters, the "generalized" model has been tested using different experiments at increasing viscosity. The model performances were compared with the ones obtained with the Coulaloglou and Tavlarides kernels employed in Chapter 4 (the "initial" model), that consider the droplets size in the inertial subrange. In both cases, the turbulent inhomogeneity in the stirred tank reactor was accounted through the volumetric probability density function of the turbulent dissipation rate, which allowed the computation of volume-average kernels [20,22].

5.3.1. Parameters identification

The water-in-Isane experiments with 1% (Chapter 4, Fig. 4.7) and 2% (Fig. 5.4) of water volume fraction, and an impeller rotation speed of 600 rpm (red circles), were used to identify the parameters.

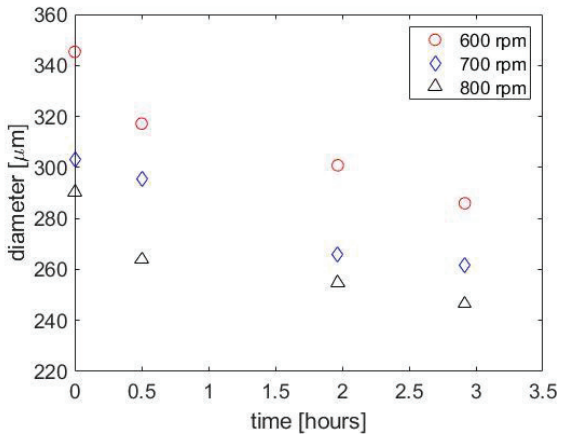


Figure 5.4: Time-evolution of the droplet Sauter mean diameters for water-in-oil experiments: continuous phase viscosity 1.2 cP, water volume fraction of 2%, stirring rate of 600, 700, and 800 rpm.

The optimization was performed in MATLAB using the patternsearch function (Global Optimization toolbox) to minimize the sum of the square of the differences between the experimental and simulated Sauter mean diameters (Fig. 5.5).

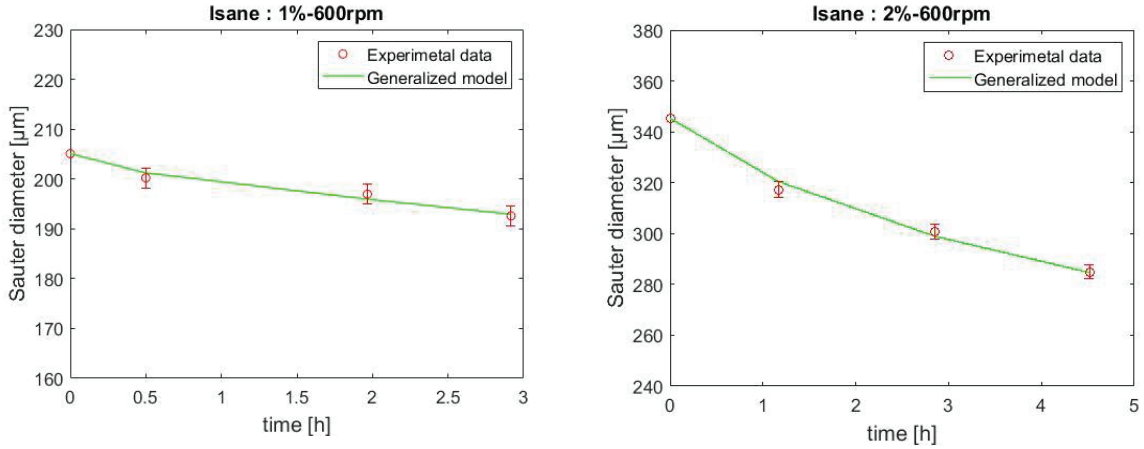


Figure 5.5: Parameters identification of the "generalized model" on water-in-Isane experiments (error bar: 1% of the experimental value): continuous phase viscosity 1.2 cP, water volume fraction of 1 (left) – 2 (right) %, stirring rate of 600 rpm.

The adjusted parameters (Table 5.2) were identified with an average relative error lower than 1% (Table 5.3).

Table 5.2: Identified parameters for the "generalized" model. Also the parameters for the "initial" model are reported [22].

	Breakup		**Coalescence**	
	C_1	C_2	C_3	C_4
"Generalized"	2.23×10^{-4}	7.08×10^{-1}	1.0073	1.68×10^{18}
"Initial"	1.20×10^{-3}	7.11×10^{-1}	1.95×10^{-2}	2.05×10^{14}

Table 5.3: Relative errors according to Eq. (5.7) in the determination of the adjusted parameters at an impeller rotation speed of 600 rpm

	1% water-in-Isane			**2% water-in-Isane**		
Experimental (µm)	200.5	197.6	193.9	318.2	300.8	285.9
Optimization (µm)	201.2	196.8	194.4	320.4	299.3	284.4
Relative error (%)	0.35	0.43	0.25	0.71	0.48	0.53
Average rel. err. (%)	0.46					

The relative errors were computed according to the following expression:

$$Relative\ Error\ (\%) = 100\frac{|experimental\ data\ (t) - simulated\ value\ (t)|}{experimental\ data(t)} \qquad (5.7)$$

5.3.2. Low continuous phase viscosity

The generalized model was tested with experiments at low continuous phase viscosity (1.2 cP), employing pure Isane (continuous phase) and water (dispersed phase, 1-2% volume fraction), at different impeller rotation speeds (700 and 800rpm).

As can be seen in Fig. 5.6, the "generalized model" is capable of well reproducing the time evolution of the Sauter mean diameters both for different stirring conditions (i.e., different turbulent conditions) and disperse phase volume fractions.

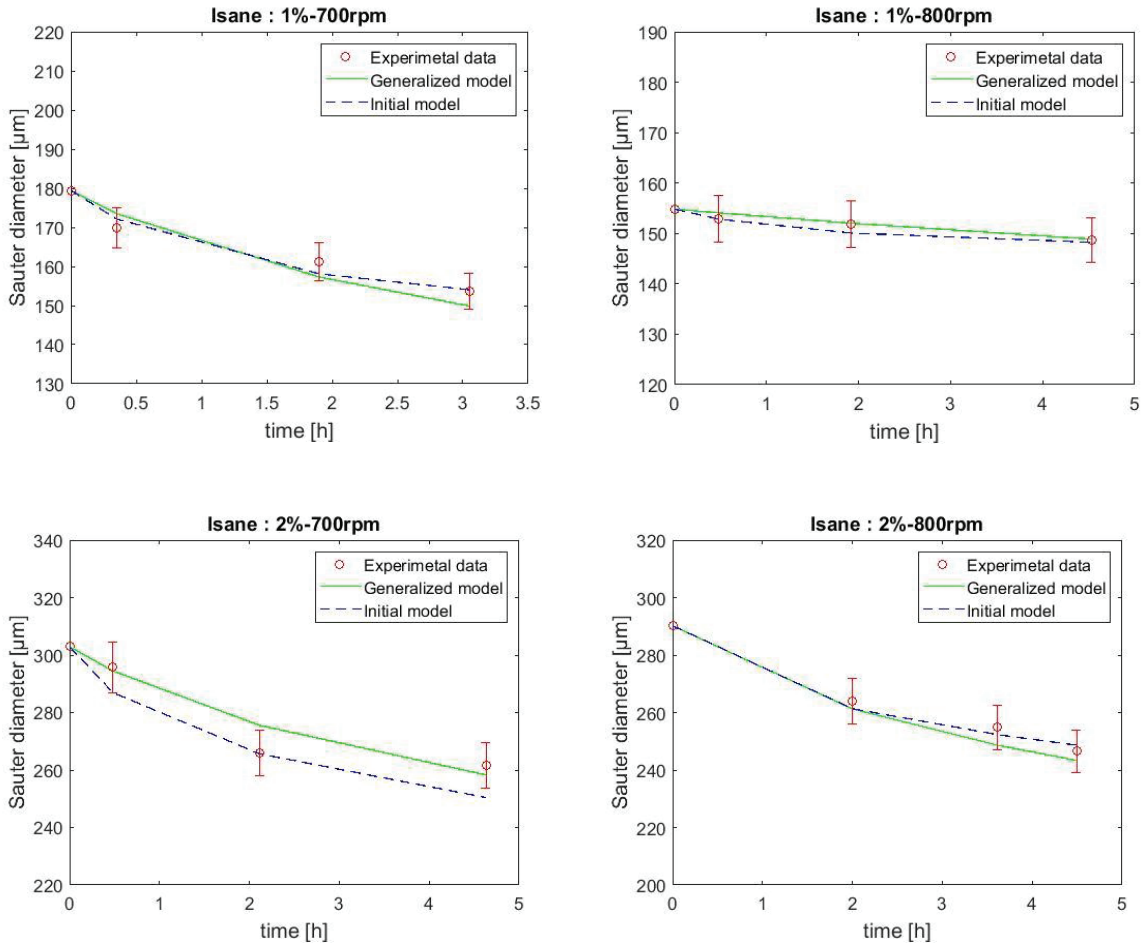


Figure 5.6: "Generalized model" testing on water-in-Isane experiments (error bar: 3% of the experimental value): continuous phase viscosity 1.2 cP, water volume fraction of 1 (top) – 2 (bottom) %, stirring rate of 700 (left) and 800 (right) rpm.

As already evidenced in our previous work [22], also the "initial model" can correctly reproduce the experimental d_{32} evolution. Indeed, the two models fit the experimental data with average relative errors below 3% (Table 5.4).

Table 5.4: Relative errors (Eq. 5.7) by fitting the 1-2% water-in-Isane experiments through the "generalized" and "initial" models

	1% water-in-Isane						**2% water-in-Isane**					
	700 rpm			**800 rpm**			**700 rpm**			**800 rpm**		
	"Generalized" model											
Rel err. (%)	2.18	2.42	2.47	0.78	0.07	0.13	0.41	3.57	1.26	0.95	2.43	1.34
Average (%)	2.36			0.33			1.75			1.57		
	"Initial" model											
Rel err. (%)	1.35	1.92	0.26	0.07	1.18	0.34	2.98	0.19	4.28	0.95	0.98	0.81
Average (%)	1.18			0.53			2.48			0.91		

It is interesting to remark that, in the considered continuous phase viscosity range, the boundaries between the inertial and dissipation subranges under moderated turbulent dissipation rates are in the order of few millimeters (as reported in Table 5.5).

Table 5.5: Kolmogorov microscale (η) and Inertial/Dissipation subranges boundary (l_{DI}) for the Isane/Marcol experiments at different viscosity and turbulent conditions

Viscosity (cP)	Turbulence scales	Speed [rpm] / Average ε [m^2/s^3]		
		600 / 0.62	**700 / 1.01**	**800 / 1.42**
1.2	η [μm]	50.92	45.07	41.39
	l_{DI} [mm]	3.05	2.70	2.48
2.4	η [μm]	82.94	73.89	67.1
	l_{DI} [mm]	4.98	4.43	4.03
4.1	η [μm]	120.96	107.76	97.87
	l_{DI} [mm]	7.26	6.47	5.87

Therefore, even in the system with the lowest value of continuous phase viscosity considered here, many droplets are contained in the dissipation range, since the majority of them have dimensions below 700 μm (Fig. 5.7).

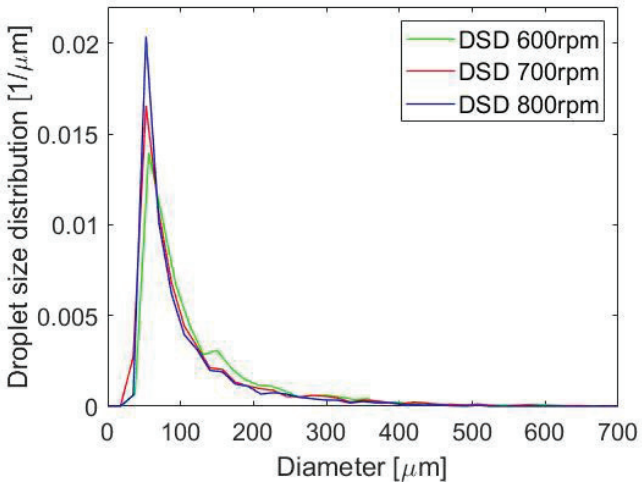


Figure 5.7: Examples of droplet number density function for water-in-Isane experiments: water volume fraction of 2%, stirring rate of 600 (green), 700 (red) and 800 (blue) rpm.

The reason why the "initial model" may however be able to predict the experimental behavior could be due to the summation of two errors canceling out: on one side, the overestimation of the eddy turbulent kinetic energy (as discussed in Sec. 5.1), and, on the other side, the neglecting of the enstrophy contribution. Indeed, the "initial model" is based on the Kolmogorov second-order structure function, which only considers the turbulent kinetic energy of eddies with size smaller than the droplet diameter, assuming they all belong to the inertial subrange. On the other hand, the refined second-order structure function proposed by Davidson [43] depends both on the turbulent kinetic energy of eddies with size smaller than the droplet diameter and on the enstrophy of the bigger ones. While the two expressions give similar results in the low viscosity system considered here, only the second one (*i.e.* the generalized model) is based on correct theoretical basis and gives proper predictions when the viscosity of the continuous phase increases, as will be shown in the following section.

5.3.3. High continuous phase viscosity

The results obtained with both the "generalized" and the "initial" models were compared with the experiments performed at higher continuous phase viscosities (2.4 cP, and 4.1 cP), obtained by increasing the proportion of Marcol 82 in the mixture (from 30 to 45%, Table 5.1). As it can be seen in Fig. 5.8 - 5.9, for these experiments, the observed dynamics of the droplet size evolution are slower than in the case of pure Isane (lower viscosity). Indeed, the higher the continuous phase viscosity, the wider the dissipation subrange (Table 5.5), and the subsequent reduction of the eddy energy. This lower energy leads to lower pressure and velocity fluctuations at the droplet surface, and hence to a decrease of the breakage rate.

The two models were first compared with the experiments at 1-2% volume fraction of the disperse phase (water) in the continuous phase (oil) at 2.4 cP viscosity. As illustrated in Fig. 5.8 and 5.9, for both concentrations, the "generalized model" correctly reproduces the time evolution of the Sauter mean diameter, regardless of the stirring rate (*i.e.* the turbulent conditions).

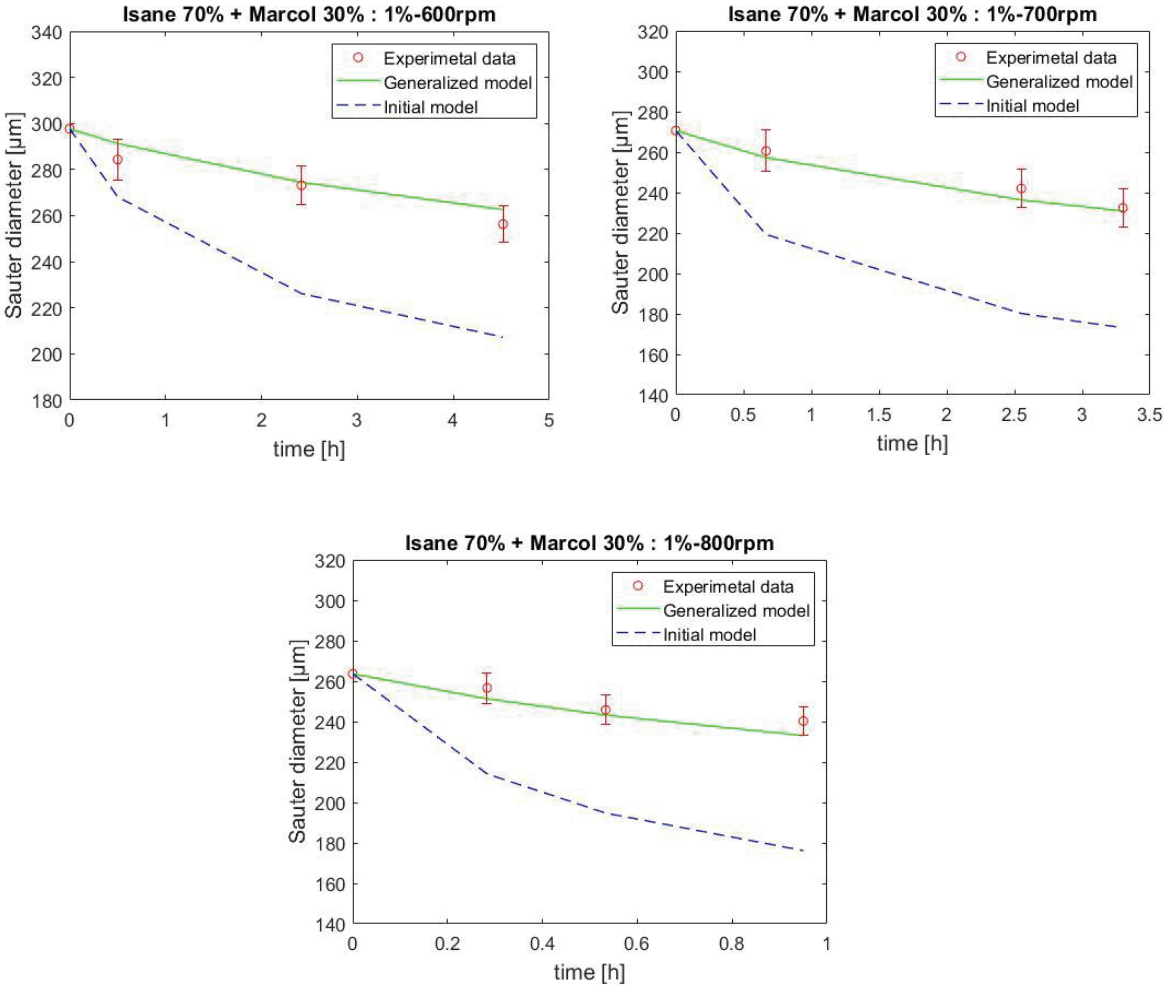


Figure 5.8: "Generalized model" testing on water-in-*Isane70%/Marcol30%* experiments (error bar: 3% of the experimental value): continuous phase viscosity 2.4 cP, water volume fraction of 1%, stirring rate of 600 (top-left), 700 (top-right), and 800 (bottom) rpm.

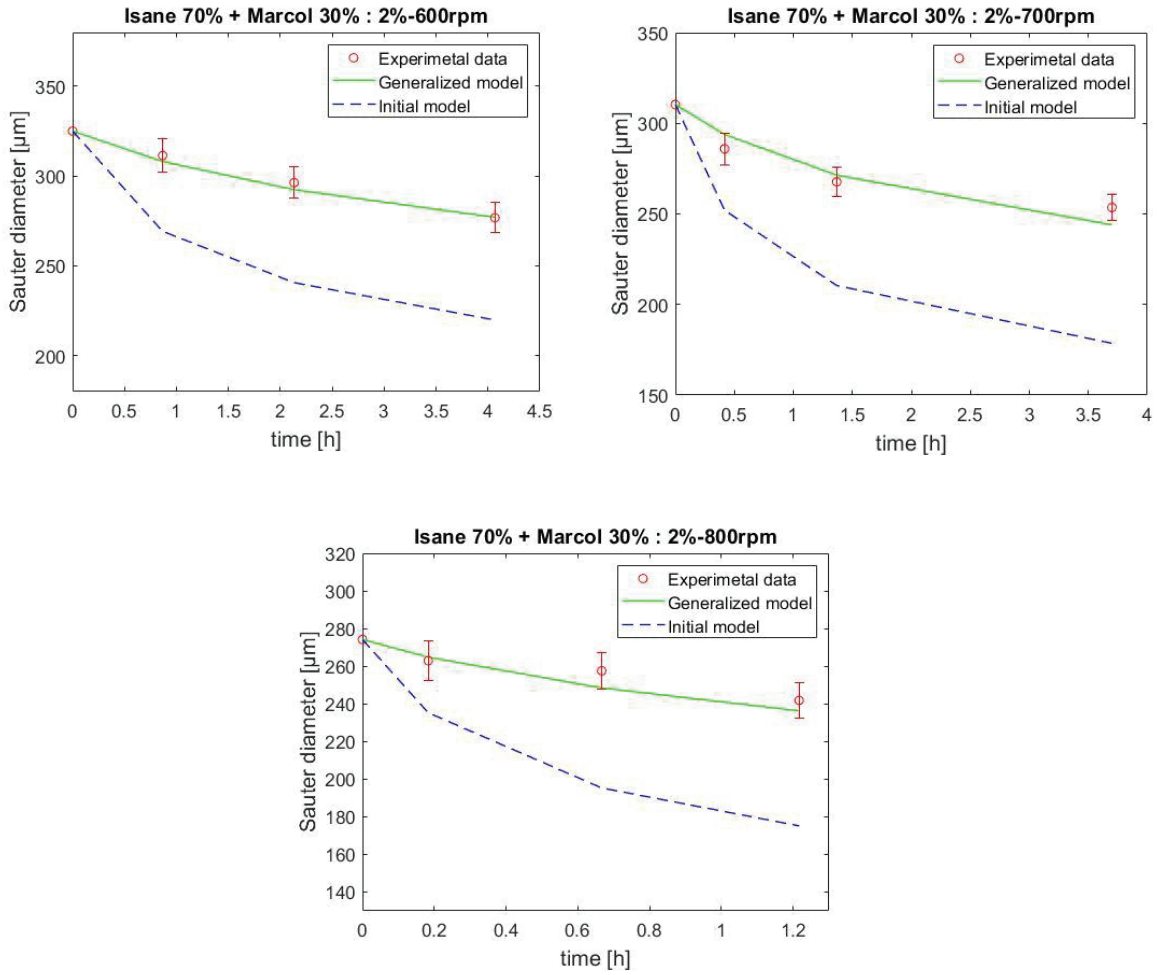


Figure 5.9: "Generalized model" testing on water-in-*Isane70%/Marcol30%* experiments (error bar: 3% of the experimental value): continuous phase viscosity 2.4 cP, water volume fraction of 2%, stirring rate of 600 (top-left), 700 (top-right), and 800 (bottom) rpm.

Indeed, the average relative error for each experiment is always below 3% (Table 5.6-5.7). On the other hand, the "initial model" predicts Sauter mean diameters that are always smaller than the experimental ones. For these cases, the average relative errors are almost 20% the experimental data (Table 5.6-5.7).

Table 5.6: Relative errors (Eq. 5.7) by fitting the 1% water-in-Isane70%Marcol30% experiments through the "generalized" and "initial" models:

	600 rpm			**700 rpm**			**800 rpm**		
	"Generalized" model								
Rel. err. (%)	2.46	0.48	2.46	1.27	2.35	0.65	2.07	1.06	3.00
Average (%)	1.80			1.42			2.04		
	"Initial" model								
Rel. err. (%)	5.66	17.17	19.12	15.85	25.57	25.52	16.56	20.79	26.67
Average (%)	13.98			22.31			21.34		

Table 5.7: Relative errors (Eq. 5.7) by fitting the 2% water-in-Isane70%Marcol30% experiments through the "generalized" and "initial" models:

	600 rpm			**700 rpm**			**800 rpm**		
	"Generalized" model								
Rel. err. (%)	1.06	1.32	0.11	2.76	1.38	3.75	0.72	3.53	2.32
Average (%)	0.83			2.63			2.19		
	"Initial" model								
Rel. err. (%)	13.55	18.76	20.59	11.86	21.40	29.55	10.50	24.16	27.58
Average (%)	17.63			20.94			20.74		

As previously discussed, using the Kolmogorov second-order structure function results in an overestimation of the eddy turbulent kinetic energy in the dissipation subrange, which leads to higher breakage rates. This is consistent with the observed prediction of smaller droplets by the initial model.

The models were finally tested with the experiments performed using the continuous phase with the higher viscosity (4.1 cP). Note that this was the maximum value of viscosity in order to achieve turbulent flow [55,56,66,79] at the lowest rotational speed experimentally investigated (Table 5.8).

Table 5.8: Impeller Reynolds numbers at different rotational speeds and viscosities

Rotational speed [rpm]	**Reynolds number**		
	μ = 1.2 cP	**μ = 2.4 cP**	**μ = 4.1 cP**
600	22368	11611	7020
700	26096	13546	8190
800	29824	15481	9360

Again, the "generalized model" appears very efficient to predict the time-evolution of the Sauter mean diameter (see Fig. 5.11), with average relative errors below 2%.

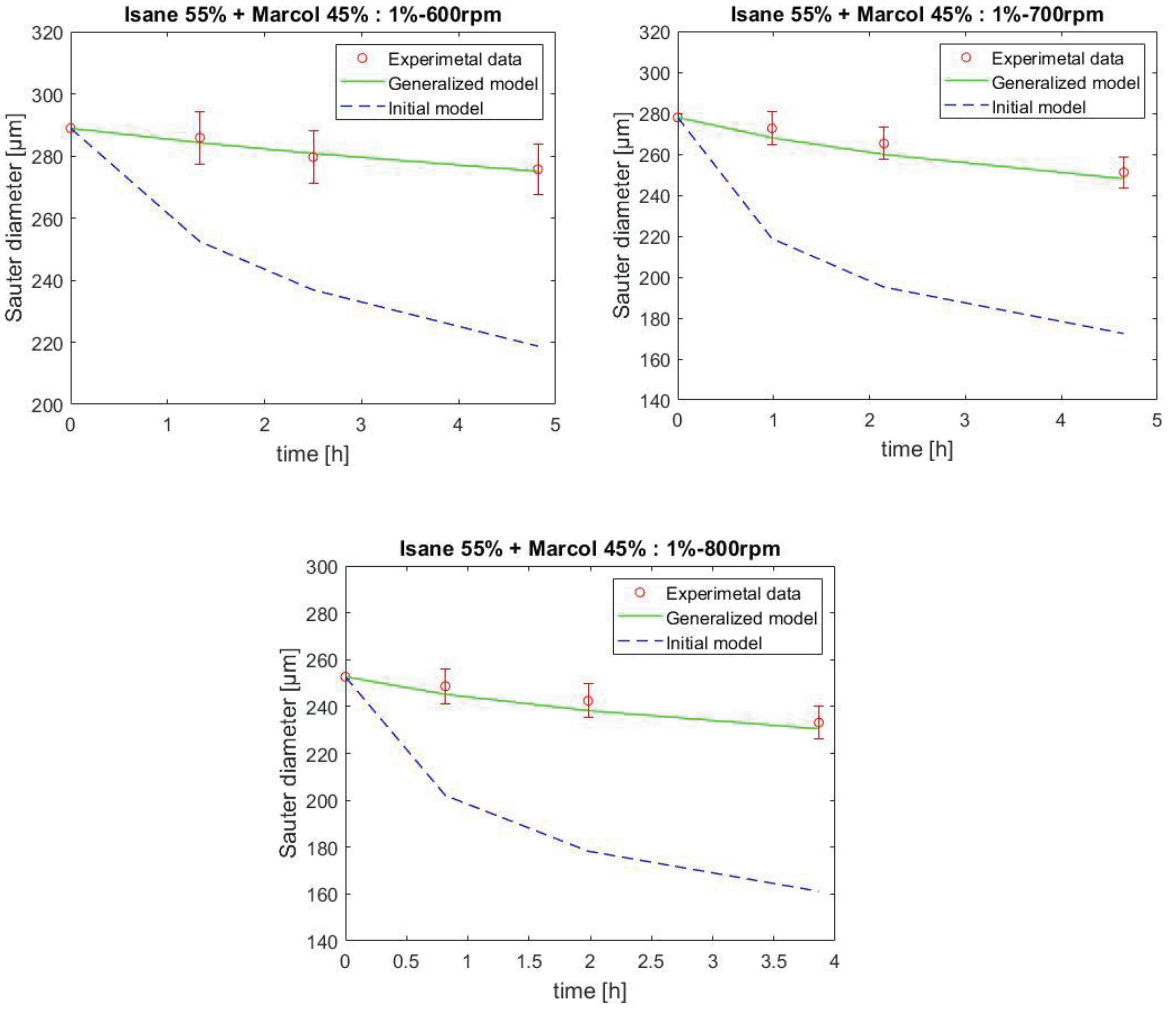


Figure 5.10: "Generalized model" testing on water-in-*Isane55%/Marcol45%* experiments (error bar: 3% of the experimental value): continuous phase viscosity 4.1 cP, water volume fraction of 1%, stirring rate of 600 (top-left), 700 (top-right), and 800 (bottom) rpm.

With the "initial" model the deviation between the measurements and the predictions is even larger than at 2.4 cP, since the average relative errors can go up to the 29% of the experimental data (Table 5.9).

Table 5.9: Relative errors (Eq. 5.7) by fitting the 1% water-in-Isane55%Marcol45% experiments through the "generalized" and "initial" models:

	600 rpm			700 rpm			800 rpm		
	"Generalized" model								
Rel. err. (%)	0.52	0.43	0.25	1.69	2.04	1.23	1.41	1.73	1.12
Average (%)	0.4			1.65			1.42		
	"Initial" model								
Rel. err. (%)	11.69	15.31	20.67	19.74	32.77	35.84	18.74	26.47	30.89
Average (%)	15.89			29.45			25.37		

Indeed, the viscosity dissipative effect in the dissipation subrange is more important at 4.1 cP than at 2.4 cP. This confirms the improvement provided by the generalized model, that implements a more appropriate and accurate calculation of the effective turbulent kinetic energy of eddies, and accounts for the effect of viscosity in the dissipation range.

5.4. Conclusions

In this work, we implemented an improved description of the turbulence spectrum in the breakage and coalescence kernels formulated by Coulaloglou and Tavlarides. The Coulaloglou and Tavlarides kernels, as most of the kernels available in the literature for liquid-liquid dispersions, assume that the droplets have dimensions in the same range of the characteristic eddy sizes belonging to the inertial subrange of turbulence. This assumption is generally not valid in liquid-liquid extractors that work at moderated Re, and for which the boundaries between the inertial and the dissipation subrange have dimensions of millimeters. This assumption leads to even larger errors as the viscosity of the continuous phase increases. In these cases, the majority of the droplet sizes lies in the dissipation range, and the most adopted second-order structure function included in the most popular coalescence and breakage kernels, proposed by Kolmogorov for the inertial subrange, is not valid.

To account for a wider range of turbulence, the Pope energy spectrum model [44] has been chosen to compute a generalized second-order structure function, valid in the whole turbulent energy spectrum [43,74,75]. The formulation proposed by Pope is indeed convenient, since it expresses 3 contributions, each one being predominant in a given energy range (*i.e.* the energy-containing, inertial, and dissipation subranges). Thanks to the inclusion of this generalized function, the breakage and coalescence rates of droplets having dimensions in the dissipation range can be taken into account, and this is particularly helpful for high viscosity systems.

To prove this last statement, a series of turbulent liquid-liquid dispersion experiments, considering increasing viscosity of the continuous phase (1.2, 2.1 and 4.2 cP), were performed in order to validate the proposed generalized kernels. The model was observed to perfectly reproduce the experimental evolution of the Sauter mean diameter, at low dispersed phase volume fraction, in the whole range of investigated viscosities and stirring rates.

Complementing previous works aimed at improving the description of the turbulent spectrum in liquid-liquid breakage kernels [74,80], these new results show that more accurate models can be derived. They rely on the combination of *i)* a refined description of the turbulence spectrum, using a proper second-order velocity structure function, and *ii)* the consideration of turbulent dissipation heterogeneity in the apparatus, using the pdf of the turbulent dissipation rate ε. Improving the description of turbulence in coalescence and breakage kernels, at both the droplet and the apparatus scales, is indeed a strong requirement for model-based industrial liquid-liquid process development.

6. A hydrodynamic model of the pulsed column

A model that allows to simulate the hydrodynamic behavior of a pulsed column is proposed and experimentally validated. The model is based on a 1D Population Balance Equation (PBE), whose source terms have been modeled through the generalized version of the Coulaloglou and Tavlarides kernels proposed and validated in Chapter 5. The turbulent inhomogeneities in the pulsed column have been accounted for through a time-averaged probability density function of the turbulent dissipation rate ε, as described in Chapter 4. This function was extracted from transient single-phase CFD simulations of the pulsed column. Turbulent liquid-liquid experiments at different dispersed and continuous phase flowrates and pulsation intensities in the pulsed column were performed and the Sauter mean diameters and the dispersed phase volume fractions were measured. The experimental data were employed in the validation of 1D PBE model based on the improvements on the breakage and coalescence kernels. The model was found to correctly reproduce the Sauter mean diameters and the dispersed phase volume fractions at the different operating conditions.

6.1. Experimental case study

6.1.1. Experimental setup

The liquid-liquid dispersion experiments have been performed in a lab-scale pulsed column (Fig. 6.1), characterized by a diameter D of 25 mm and a height H of 2 m. The column contains a packing of disks and doughnuts alternately arranged, of 1 mm thick and 24 mm distant. The extremities of the column present two settlers.

When the dispersed phase density (water) is higher than the continuous one (oil), it accumulates in the lower decanter, and *vice versa*. An air compressor, connected to the bottom decanter through a pulsation leg, provides a sinusoidal oscillating motion that is superimposed on the flow in the column. These oscillations facilitate the formation of a dispersion inside the column. The pulsed column presents two inlets and two outlets. The continuous phase inlet is placed in the bottom decanter, while the dispersed phase one in the top settler. Both phases are

fed to the column using pumps. For the considered water-in-oil configuration, the dispersed phase outlet is positioned in the bottom decanter, under the continuous phase inlet.



Figure 6.1: Lab-scale pulsed column with the SOPAT probe

The aqueous phase is extracted by mean of a pump. The continuous phase outlet is placed in the top decanter. The continuous phase is not pumped out of the column, but it leaves the column once it reaches the overflow. It is possible, therefore, to adjust separately the inlet and outlet mass flow rates of the dispersed phase, and the inlet mass flow rate of the continuous phase.

The droplet size distribution and the Sauter mean diameter have been determined thanks to an endoscopic probe (SOPAT®). The probe is inserted perpendicularly, in the middle of the column (Fig. 1), positioned as closed as possible to the column wall in order to reduce the flow perturbation. It is equipped with a high-speed camera which allows to capture images of the dispersion in the column. After the image-processing, the Sauter mean diameter is obtained.

On the other hand, dispersed phase volume fraction is determined by analyzing samples of the dispersion extracted from the column center. The sample is drawn with a syringe through the valve located on the column.

6.1.2. Tested phase system

In order to test and validate the proposed model based on a refined turbulence description of the droplet breakage and coalescence kernels, experiments have been carried out in the pulsed column. In this aim, distilled water was used as the dispersed phase, while Isane 175 as the continuous organic phase. Isane 175 is an isoparaffinic compound provided by Total, containing less than 1 ppm of benzene and 20 ppm of aromatic compounds. The properties of the two fluids are reported in Table 6.1.

Table 6.1: Physical-chemical properties of the tested phases

Product \ property	**density (ρ, kg/m^3)**	**viscosity (μ, Pa.s)**	**surface tension (N/m)**
water	997.8	0.001	0.0293
Isane	762	0.0012192	

6.1.3. Experimental procedure

The reported experiments are performed in the water-in-oil operating mode. In addition of being generally preferred conditions in solvent extraction using radioactive species (*e.g.*, phase separation at the floor level, reduction of solvent irradiation, etc.), they also make possible to investigate weakly turbulent regimes (due to the higher viscosity of the continuous phase in this mode). The experiments have been carried out in the pulsed column at different mass flowrates and pulsation intensities.

The column is first filled with the continuous (organic) phase. Then, the dispersed phase is introduced by mean of a pump in the bottom decanter. Once both phases are flowing in the column, the air compressor was switched on and the pulsation started. After the adjustment of the pulsation (according to the desired frequency f and amplitude A), the flowrates of the continuous and dispersed phases are regulated.

The flow in the pulsed column is characterized by a transient period, during which the dispersed phase accumulates all along the column. Following this phase, permanent flow is

achieved, where the macroscopic properties of interest, as the dispersed phase volume fraction and the Sauter mean diameter, are constant. For this reason, the image acquisition and collecting samples of the dispersion were done one hour after having adjusted the pulsation and the mass flowrates. It lasted 60 seconds, with a capture rate of 5 frames/s. The images were treated afterwards using the image-processing software provided with the probe, in order to get the Sauter mean diameter of the dispersed phase population. To obtain the dispersed phase volume fraction, the collected samples of the dispersion were centrifuged for 5 minutes at 5000 rpm, in order to separate the two phases.

6.1.4. CFD simulations

The computation of the volume-averaged breakage and coalescence kernels required the knowledge of the probability density function of the turbulent kinetic dissipation energy rate in the liquid-liquid contactor. This property was obtained through CFD simulations run using ANSYS Fluent 17.2.

As detailed in previous works [69–71], the single-phase flow in the pulsed column can be correctly represented in an axisymmetric framework. The flow is indeed much more developed along the radial and axial coordinates, while it can be approximated uniform along the tangential coordinate [71,81]. A half-section of the column, consisting of three compartments, was simulated. As each compartment of the column is assumed to undergo similar flow conditions far from the column ends, the pdf of ε was extracted from the "central" compartment of the computational domain.

An axisymmetric boundary condition was applied to the column axis, along with no-slip wall boundary conditions for the column internals. The inlet velocity, applied as boundary condition at the first compartment, is given by the superposition of the velocity related to the continuous phase flow rate and the oscillation velocity arising from the pulsation:

$$v(t) = A\pi f \cos(2\pi f t) + \frac{Q_c}{S_{inlet}} \tag{6.1}$$

This function was implemented by a User Defined Function (UDF). A pressure outlet boundary condition is applied in the opposite compartment considering a gauge pressure equal to zero.

Due to the periodic nature of the pulsation, transient simulations were carried out. A period of the flow was simulated considering 100 time steps, with 50 to 100 iteration per time step. This set-up allowed to reach the relative convergence criteria (10^{-6}) at each time step. The simulation of 5 periods was sufficient to confirm the periodicity of the flow. The time-averaged probability density function of ε, over a period, was obtained by the Data Sampling function available in ANSYS Fluent.

The *standard* k-ε model along with the enhanced wall-treatment function was employed to simulate the flow. The SIMPLE algorithm [64] was selected as pressure-velocity coupling method and the spatial derivatives of the equations were discretized by mean of a second order upwind method. Finally, the Bounded Second Order Implicit method was employed for discretizing the time derivatives.

Before each transient simulation, a steady state simulation was performed with an inlet velocity equal to the time-averaged velocity in the column over a period:

$$\bar{v} = 2Af + \frac{Q_c}{S_{inlet}} \tag{6.2}$$

The results of the steady-state simulation were used as initial condition for the transient simulation, in order to get a faster convergence.

A CFD simulation was performed for each value of amplitude A and continuous phase flowrate Q_c considered in the experimental study. In this way, a pdf of ε was obtained for each different experimental condition and stored in the database of the 1D PBE model of the column. Each CFD simulation took around 5 hours to be run on an Intel Xeon dual-core machine (3.20 GHz) with 64GB of RAM.

6.2. Model development

6.2.1. 1D PBE model

In order to account for the polydispersity of the droplet population, a PBE model is used to describe the droplet size of the dispersed phase. In the most general case, the 3D PBE model considers a number density function which is function of the internal coordinates $\boldsymbol{\varphi}$, the spatial coordinates $\boldsymbol{x}$ ($\boldsymbol{x} = [x, y, z]$) and the time t [6,7]. As we are here interested in tracking the interfacial area and the dispersed phase volume fraction, only the droplet volume v will be considered as internal coordinate ($\boldsymbol{\varphi} = v$). Therefore, the 3D PBE reduces to:

$$\frac{\partial}{\partial t}[n(\boldsymbol{x}, v, t)] + u(\boldsymbol{x}, v, t)\frac{\partial}{\partial x_i}[n(\boldsymbol{x}, v, t)] = s(\boldsymbol{x}, \boldsymbol{v}, t) \tag{6.3}$$

where the source term $s(\boldsymbol{x}, v, t)$ stands for:

$$\begin{aligned} s(\boldsymbol{x}, v, t) = & \int_v^{\infty} p(v')\,\beta(v|v')\Gamma(\boldsymbol{x}, v')n(\boldsymbol{x}, v', t)\,dv' - \Gamma(\boldsymbol{x}, v)n(\boldsymbol{x}, v, t) \\ & + \frac{1}{2}\int_0^{v} Q(\boldsymbol{x}, v - v', v')\,n(\boldsymbol{x}, v - v', t)n(\boldsymbol{x}, v', t)\,dv' \\ & - n(\boldsymbol{x}, v, t)\int_0^{\infty} Q(\boldsymbol{x}, v, v')n(\boldsymbol{x}, v', t). \end{aligned} \tag{6.4}$$

Γ and Q are the breakage and coalescence kernels and $\beta(v|v')$ is the daughter distribution function.

Since the flow in an extraction column is mainly along the axial direction, the PBE model can be simplified assuming a NDF dependent on one spatial coordinate (z) while being homogeneous in the column section:

$$\bar{n}(z,v,t) = \frac{1}{S}\int_S n(\boldsymbol{x},v,t)dS \tag{6.5}$$

Despite this assumption, the PBE model remains likely to be 3D-space dependent due to the breakage and coalescence kernels. Therefore, the volume-averaged kernels, introduced by Buffo et al. [20] and recently implemented by Castellano et al. [22] (Chapter 4), have been selected to better account for the turbulence inhomogeneities in the 1D hydrodynamic model:

$$\bar{\Gamma}(v) = \frac{1}{V}\int_V \Gamma(\boldsymbol{x},v)d\boldsymbol{x} = \int_0^\infty \Gamma(\varepsilon,v)f(\varepsilon)d\varepsilon \tag{4.1}$$

$$\bar{Q}(v,v') = \frac{1}{V}\int_V Q(\boldsymbol{x},v,v')d\boldsymbol{x} = \int_0^\infty Q(\varepsilon,v,v')f(\varepsilon)d\varepsilon \tag{4.2}$$

In these equations, $f(\varepsilon)$ represents the probability density function (PDF) of the turbulent kinetic energy dissipation rate ε, which defines the influence of the turbulent eddies in the droplet breakage and coalescence. As previously mentioned, the latter can be obtained by CFD simulations of the liquid-liquid extractor.

The final 1D PBE model reads:

$$\frac{\partial}{\partial t}[n(z,v,t)] + u(z,v,t)\frac{\partial}{\partial z}[n(z,v,t)]$$
$$= \int_{v}^{\infty} \beta(v|v')n(z,v',t)\int_{0}^{\infty} \Gamma(\varepsilon,v)f(\varepsilon)d\varepsilon\, dv'$$
$$- n(z,v,t)\int_{0}^{\infty} \Gamma(\varepsilon,v)f(\varepsilon)d\varepsilon \qquad (6.6)$$
$$+ \frac{1}{2}\int_{0}^{v} n(z,v-v',t)n(z,v',t)\int_{0}^{\infty} Q(\varepsilon,v,v')f(\varepsilon)d\varepsilon\, dv'$$
$$- n(z,v,t)\int_{0}^{\infty} n(z,v',t)\int_{0}^{\infty} Q(\varepsilon,v,v')f(\varepsilon)d\varepsilon\, dv'$$

6.2.2. Mass conservation

The 1D PBE model will be coupled with the mass conservation equation for the continuous phase. Since neither accumulation nor generation take place in the continuous phase, the mass flow rate, Q_c, is uniform in the column:

$$Q_c = const$$

In order to respect this constraint, the continuous phase velocity has to respect:

$$u_c(z) = \frac{F_c}{\rho_c S(1-\phi_d(z))} \qquad (6.7)$$

where the dispersed phase volume fraction $\phi_d(z)$ can be computed from the solution of the 1D PBE model.

6.2.3. Droplet velocity

The coupling of the PBE with the 1D counter-current flow model requires the knowledge of the droplet velocity $u(z,v)$. In the model adopted here, the latter is dependent on the droplet

diameter and the dispersed phase volume fraction, $\phi_d(z)$. The velocity of a droplet class is defined with respect to the fixed wall columns by the following kinematic relation [82]:

$$u(\phi_d(z), v) = u_r(\phi_d(z), v) + u_c\big(\phi_c(z)\big) \tag{6.8}$$

where $u_r(\phi_d(z), v)$ represents the velocity of a moving droplet of volume v with respect to the continuous phase, and $u_c\big(\phi(z)\big)$ is the continuous phase velocity. $u_r(\phi(z), v)$, the relative velocity, can be expressed as:

$$u_r(\phi(z), v) = k_v u_t(d)(1 - \phi_d) \tag{6.9}$$

where $u_t(d)$ represents the droplet terminal velocity in a stagnant fluid, k_v a factor accounting for the velocity dampening due to the column packing [83], and $(1 - \phi_d)$ the swarm or collective effect caused by the presence of the other droplets. The Klee and Treybal correlation for $u_t(d)$ has been employed [84]:

$$\begin{cases} u_t(d) = 38.3\rho_c^{-0.45}\Delta\rho^{0.58}\mu_c^{-0.11}d^{0.7} & for\ d < d_c \\ u_t(d) = 17.6\rho_c^{-0.55}\Delta\rho^{0.28}\mu_c^{0.1}\sigma^{0.18} & for\ d > d_c \end{cases} \tag{6.10}$$

where:

$$d_c = 0.33\rho_c^{-0.14}\Delta\rho^{-0.43}\mu_c^{0.3}\sigma^{0.24}$$

The slowing down factor k_v depends on the geometry of the extraction column which is considered. In the case of a pulsed column, the following values have been proposed [83]:

$$\begin{cases} k_v = 1 & if\ \dfrac{A}{H_{cp}} < 1 \\ k_v = 0.5 & if\ \dfrac{A}{H_{cp}} \approx 1 \end{cases}$$

Where A is the pulse amplitude and H_{cp} the distance between two consecutive packing elements. Since, as it will be discussed later, the experiments in the pulsed column have been performed with $\frac{A}{H_{cp}} \approx 1$, a factor $k_v = 0.5$ has been used.

6.2.4. Breakage and Coalescence kernels

The generalized Coulaloglou and Tavlarides kernels [61], presented in Chapter 5, were employed in the 1D PBE model to compute the breakage and coalescence rates:

$$\Gamma(d) = C_1 \frac{\sqrt{\langle [\Delta u(d)]^2 \rangle}}{d} exp\left(-C_2 \frac{\sigma}{\rho_d d \langle [\Delta u(d)]^2 \rangle}\right) \tag{5.5}$$

and:

$$Q(v,v') = C_3 \sqrt{\langle [\Delta u(d)]^2 \rangle + \langle [\Delta u(d')]^2 \rangle} \left(v^{\frac{2}{3}} + v'^{\frac{2}{3}}\right)\left(v^{\frac{2}{9}} + v'^{\frac{2}{9}}\right)^{1/2} \exp\left(-\frac{C_4 \mu_c \rho_c \langle [\Delta u(d+d')]^2 \rangle^{\frac{3}{2}}}{\sigma^2}\left(\frac{v^{\frac{1}{3}} v'^{\frac{1}{3}}}{v^{\frac{1}{3}} + v'^{\frac{1}{3}}}\right)^4\right) \tag{5.6}$$

where $\langle [\Delta u(d)]^2 \rangle$, the second-order structure function, reads:

$$\langle [\Delta u(r)]^2 \rangle = \frac{4}{3} \int_0^\infty E(\kappa) + 3E(\kappa) \left[\frac{\cos(\kappa r)}{(\kappa r)^2} - \frac{\sin(\kappa r)}{(\kappa r)^3}\right] d\kappa \tag{5.2}$$

6.2.5. Structure of the model

The model is composed of different units, each one performing a determined task (Fig. 6.2). The first unit contains the input data as the column geometry (diameter, height), the fluid physical-chemical properties (densities, viscosities) and the operating conditions (dispersed and continuous phase flowrates). The second unit is provided with the PDFs of ε, obtained by CFD simulations, and with the second-order structure function values previously computed for each droplet class. These properties are required for the computation of the breakage and coalescence

kernels. The kernels, along with the input data and the additional correlations (droplet terminal velocity, initial diameter) are used in the 1D-PBE solver unit in order to compute the various terms of the model (source and convective) for each droplet class and for each time and space discretization. The process is repeated until the simulation time is reached. Finally, the profiles of the droplet Sauter mean diameter and of the dispersed phase volume fraction in time and in space are obtained.

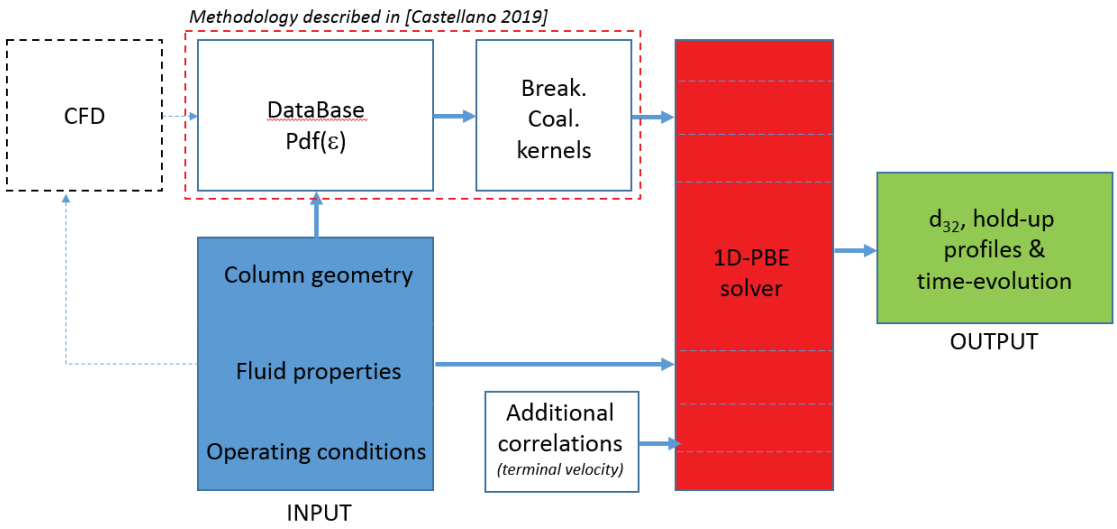


Figure 6.2: Schematic representation of the model structure

6.2.6. Numerical resolution

The 1D PBE model (Eq. 6.3) is solved by applying the Fixed Pivot Method proposed by Kumar and Ramkrishna [24]. This method is based on the discretization of the internal coordinate (the droplet volume, v) domain in intervals $[v_i, v_{i+1}]$ and the integration of the 1D PBE model in each interval as follows:

$$\int_{v_i}^{v_{i+1}} \frac{\partial}{\partial t}[n(z,v,t)] + \int_{v_i}^{v_{i+1}} u(z,v,t)\frac{\partial}{\partial z}[n(z,v,t)] = \int_{v_i}^{v_{i+1}} s(z,v,t) \qquad (6.11)$$

which leads to the following set of equations:

$$\frac{\partial}{\partial t}[N_i(z,t)] + \overline{u_i}(z,t)\frac{\partial}{\partial z}[N_i(z,t)] = S_i(z,t) \tag{6.12}$$

where $N_i(z,t)$ represents the number of droplets which have dimensions in the i^{th} interval $[v_i, v_{i+1}]$, $\overline{u_i}(z,t)$ is the velocity of a droplet with volume $\frac{v_i + v_{i+1}}{2}$ computed according to Eq. 6.9 and $S_i(z,t)$ is the source term due to breakage and coalescence events that becomes:

$$\begin{aligned} S_i(z,t) = & \sum_{\substack{j,k \\ p_{i-1} \le (p_j + p_k) \le p_{i+1}}}^{j \ge k} \left(1 - \frac{1}{2}\delta_{j,k}\right) \eta\, Q_{j,k} N_j(t) N_k(z,t) - \Gamma_i N_i(z,t) \\ & - N_i(z,t) \sum_{k=1}^{M} Q_{i,k} N_k(z,t) + \sum_{k=1}^{M} m_{i,k}\, \Gamma_k N_k(z,t) \end{aligned} \tag{6.13}$$

The set of Eq. 6.12 is solved by applying an explicit finite difference method. The accumulation term is discretized according to a first order approximation:

$$\frac{\partial N_i(z,t)}{\partial t} = \frac{N_{i,m}^{l+1} - N_{i,m}^{l}}{\Delta t} \tag{6.14}$$

where the suffix l indicates the l^{th} step in time and the suffix m the m^{th} step in space. Due to the hyperbolic nature of Eq. 6.12, a first order upwind scheme is implemented in the space discretization for stability purpose (under conditions discussed later). Since the velocity of the i^{th} class of droplets can be either negative or positive (indeed, depending on their size, the droplets can either flow counter-currently or be conveyed by the continuous flow), two different approximations have been implemented:

$$\overline{u_i} < 0 \qquad \overline{u_i}\frac{\partial N_i(z,t)}{\partial z} = \overline{u_i}\frac{N_{i,m+1}^{l} - N_{i,m}^{l}}{\Delta z} \tag{6.15}$$

$$\bar{u_\iota} > 0 \qquad \bar{u_\iota}\frac{\partial N_i(z,t)}{\partial z} = \bar{u_\iota}\frac{N_{i,m}^{l} - N_{i,m-1}^{l}}{\Delta z}$$

Finally, the $N_{i,m}^{l+1}$ can be computed as:

$$\begin{aligned} &\bar{u_\iota} < 0 \qquad N_{i,m}^{l+1} = N_{i,m}^{l} - \bar{u_\iota}\frac{\Delta t}{\Delta z}(N_{i,m+1}^{l} - N_{i,m}^{l}) + \Delta t S_i \\ &\bar{u_\iota} > 0 \qquad N_{i,m}^{l+1} = N_{i,m}^{l} - \bar{u_\iota}\frac{\Delta t}{\Delta z}(N_{i,m}^{l} - N_{i,m-1}^{l}) + \Delta t S_i \end{aligned} \tag{6.16}$$

According to the Courant-Friedich-Levy (CFL) criterion, that enables to assess the explicit scheme stability, the time and space steps must fulfill the following criteria [85]:

$$\begin{aligned} &\bar{u_\iota} < 0 \qquad 0 < \bar{u_\iota}\frac{\Delta t}{\Delta z} < 1 \\ &\bar{u_\iota} > 0 \qquad -1 < \bar{u_\iota}\frac{\Delta t}{\Delta z} < 0 \end{aligned} \tag{6.17}$$

Since the droplet velocity increases with its volume, the time and space discretization has been computed based on the velocity of the inlet droplets.

The solution of the set of partial differential equations requires initial and boundary conditions. At $t = 0$, the column is assumed to be filled only by the continuous phase. Therefore:

$$t = 0 \qquad N_{i,m}^{1} = 0 \tag{6.18}$$

where the suffix equal to 1 represents the first time step.

The boundary conditions were determined from the dispersed phase flowrate. A monodispersed droplet population is assumed at the inlet, whose size was computed according to the Scheele and Meister correlation [86]:

$$V_{drop,inlet} = F\left[\frac{\pi\sigma D_{or}}{g\Delta\rho} + \frac{20\mu_d Q_d D_{or}}{d_{drop,inlet} g\Delta\rho} - \frac{4\rho_d {Q_d}^2}{3g\Delta\rho S_{or}} + \left(\frac{{Q_d}^2 {D_{or}}^2 \rho_d \sigma}{(g\Delta\rho)^2}\right)^{\frac{1}{3}}\right] \tag{6.19}$$

where F is the Harkins-Brown factor, whose numerical value can be found in the work of Scheele and Meister. Hence, the total volume of dispersed phase entering the column at each time step is equal to:

$$V_{population} = Q_d \Delta t$$

The mass conservation implies that the droplet distribution at the opposite boundary ($z = H$) is:

$$z = H \qquad\qquad N_{i,end}^{l} = N_i$$

where N_i:

$$\begin{cases} N_i = 0 & V_i \neq V_{population} \\ N_i = \dfrac{V_{population}}{V_{drop,inlet}} & V_i = V_{population} \end{cases}$$

Once the initial and boundary conditions are set, the system can be solved for each droplet class *i* in order to obtain the instantaneous droplet distribution in the whole column, *i.e.* at each time step *l* and at each space step *m*.

In the simulations, 50 droplet classes were considered according to an arithmetic discretization. The smallest diameter was set equal to zero and the biggest was considered the droplet inlet diameter computed according to Eq. 6.19.

The column height was discretized in 30 parts. Indeed, it was remarked that a more refined discretization did not improve the accuracy of the results given by the model. To have a permanent flow in the column, a simulation time of 1 hour was enough. After having established the number of discretization for the column height, the time step was selected in order to respect the CFL criterion.

A simulation of 1 hour took around 2 minutes to be run on an Intel Xeon dual-core machine (3.20 GHz) with 64GB of RAM.

6.2.7. Kernel computation

Once a CFD simulation is completed, the probability density function of ε can be computed from the ε histogram extracted from the simulation:

$$f(\varepsilon_i) = \frac{Number\ of\ cell\ having\ \varepsilon_i\ \epsilon\ [\varepsilon_{i-1}, \varepsilon_{i+1}]}{Total\ number\ of\ cell * \Delta\varepsilon_i}$$

where $\Delta\varepsilon_i = \varepsilon_{i+1} - \varepsilon_{i-1}$. For each ε_i, a second-order structure function is computed according to Eq. (5.2). This computation is repeated for each diameter d_j considered in the discretization of the internal coordinate, in order to obtain the values for the second-order structure function at each ε_i for each diameter $d_j, \langle[\Delta u(\varepsilon_i, d_j)]^2\rangle$. For each second-order structure function value, the breakage and coalescence kernels are computed, $\Gamma(\varepsilon_i, d_j)$ and $Q(\varepsilon_i, d_j, d_k)$. Finally, the volume averaged kernels are computed by approximating Eq. 4.1-4.2 as:

$$\bar{\Gamma}(v_j) = \sum_i^I \Gamma(\varepsilon_i, v_j) f(\varepsilon_i) \Delta\varepsilon_i \tag{6.20}$$

$$\bar{Q}(v_j, v_k) = \sum_i^I Q(\varepsilon_i, v_j, v_k) f(\varepsilon_i) \Delta\varepsilon_i \tag{6.21}$$

6.3. Results and discussions

6.3.1. CFD simulation results

The CFD simulations were run in order to extract the probability density functions of ε in the pulsed column at the experimental operative conditions (pulsations and continuous phase flowrates).

The first simulation was performed considering the pulsed column subjected to a pulsation of 3.5 cm/s and a continuous phase flowrate equal to zero. The highest values of ε are localized in the proximity of the disks of the column, where the droplet breakage is likely to take place. High values are also observed next to the edges of the doughnuts. The time-averaged ε on the surface of a compartment was equal to $0.25\,\frac{W}{kg}$. Due to the periodicity of the flow, the time-averaged turbulent dissipation rate distribution was found to be symmetric with respect to the horizontal axis passing through the half of the height of the compartment (Fig. 6.3). The maximum surface-averaged ε, equal to $0.62\,\frac{W}{kg}$, was obtained at $t = 0.3 + \frac{kT}{2}$ $(k = 1,2,\dots,n)$. According to previous works [81], this maximum occurred slightly after the positive and negative peaks of the sinusoidal function employed to model the inlet velocity.

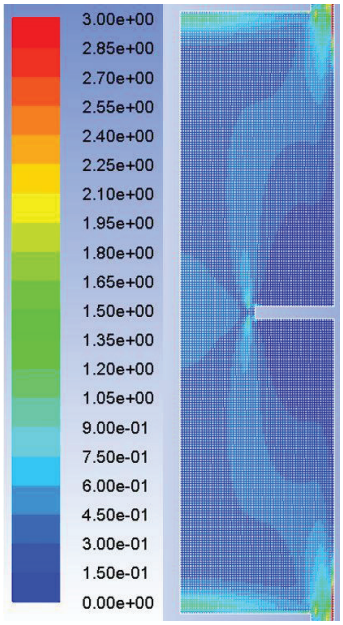


Figure 6.3: Time-averaged turbulent dissipation rate distribution in a compartment at a pulsation of 3.5 cm/s

Similar results were obtained for the simulations considering pulsations of 4.5 and 5.5 cm/s and continuous phase flowrates equal to zero (see Fig. 6.4). Indeed, the highest values of ε are predicted in the proximity of the disks and doughnuts. The time-averaged turbulent dissipation rate of a compartment was, respectively, equal to 0.60 $\frac{W}{kg}$ and 1.11 $\frac{W}{kg}$ for the pulsation intensities of 4.5 and 5.5 cm/s. As in the case of an intensity of 3.5 cm/s, the time-averaged distribution of the turbulent dissipation rate is observed to be symmetric in the compartment (Fig. 6.4). The maximum surface-averaged ε are respectively of 1.36 $\frac{W}{kg}$ and 2.52 $\frac{W}{kg}$, obtained at $t = 0.3 + \frac{kT}{2}$ $(k = 1,2, \dots, n)$. As expected, the higher the pulsation, the higher the turbulent intensity inside the pulsed column.

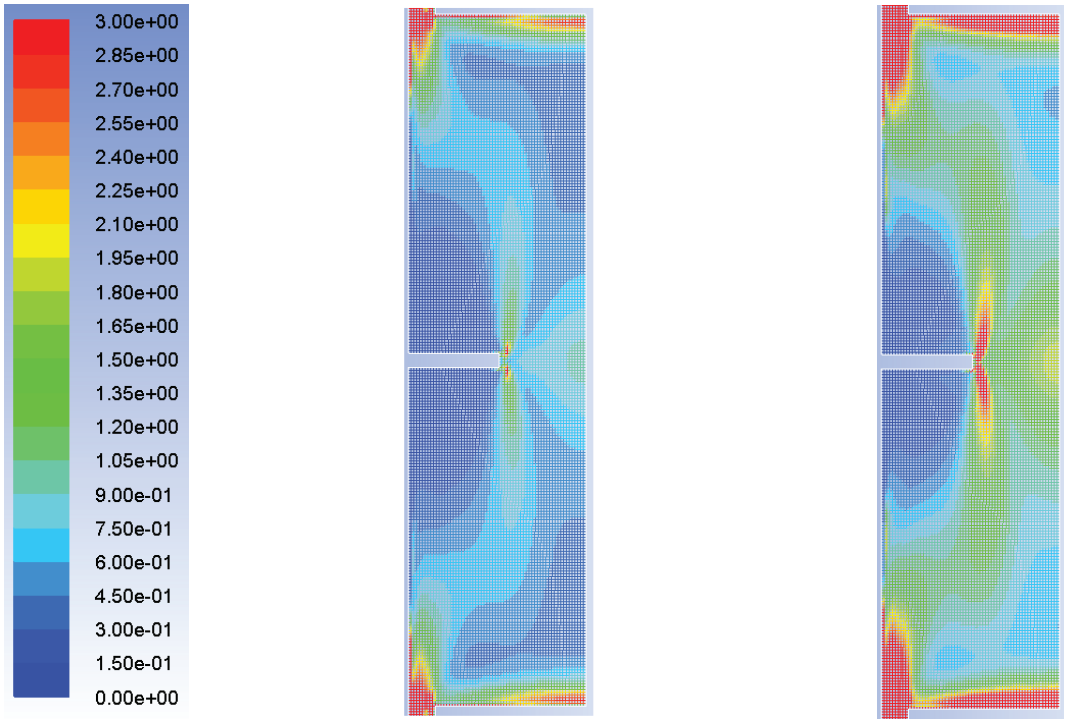


Figure 6.4: Time-averaged turbulent dissipation rate distribution in a compartment at pulsations of 4.5 cm/s (left) and 5.5 cm/s (right).

Additional CFD simulations were run to study the combined effect of the pulsation and the continuous phase flowrate on the turbulent intensity in the pulsed column. According to the performed experiments, the simulations were carried out considering continuous phase flowrates of 50 - 100 ml/min and pulsations of 3.5 - 4.5 - 5.5 cm/s.

At a continuous phase flowrate of 50 ml/min, the time-averaged turbulent dissipation rates for pulsations of 3.5 - 4.5 - 5.5 cm/s were respectively equal to 0.26 $\frac{W}{kg}$, 0.61 $\frac{W}{kg}$ and 1.12 $\frac{W}{kg}$ (Fig. 6.5), slightly higher than the ones previously computed for pure oscillating flow (i.e. continuous phase flowrate equal to 0). Therefore, the superposition of an axial velocity to the oscillating one leads to a higher turbulent intensity in the column.

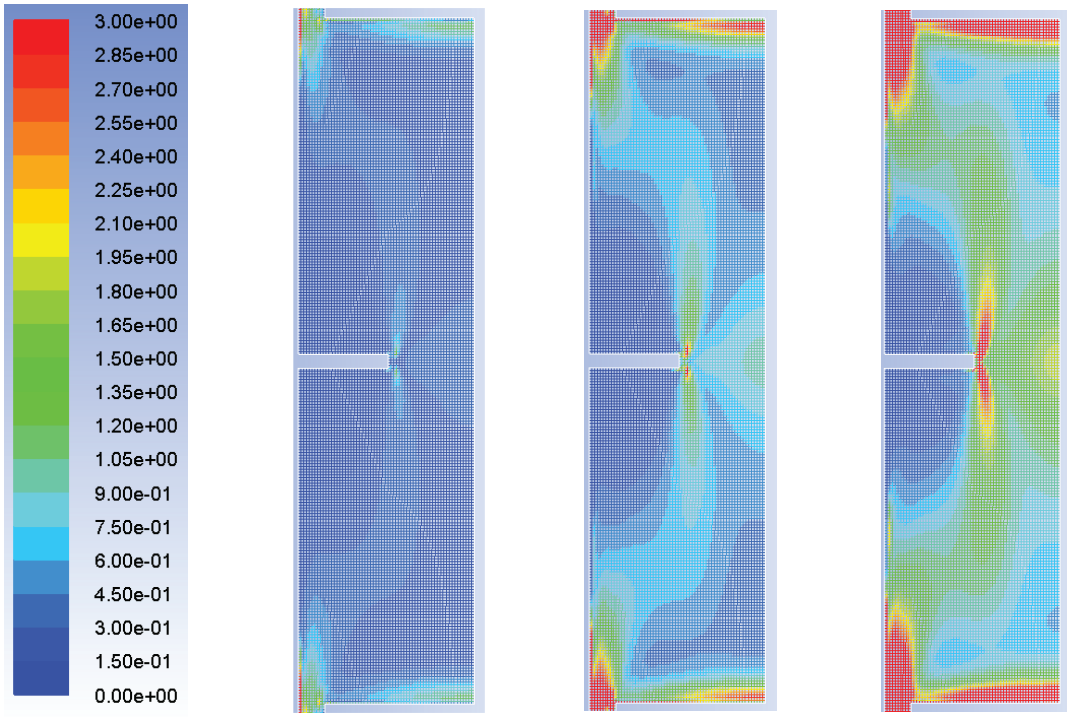


Figure 6.5: Time-averaged turbulent dissipation rate distribution in a compartment for a continuous phase flowrate of 50 ml/min and pulsations of 3.5 cm/s (left), 4.5 cm/s (centre) and 5.5 cm/s (right).

This result was confirmed by the simulations performed at a continuous phase flowrate of 100ml/min (Fig. 6.6). Indeed, in this case, the time-averaged turbulent dissipation rates were respectively equal to 0.27 $\frac{W}{kg}$, 0.63 $\frac{W}{kg}$ and 1.13 $\frac{W}{kg}$ for pulsations of 3.5 - 4.5 - 5.5 cm/s.

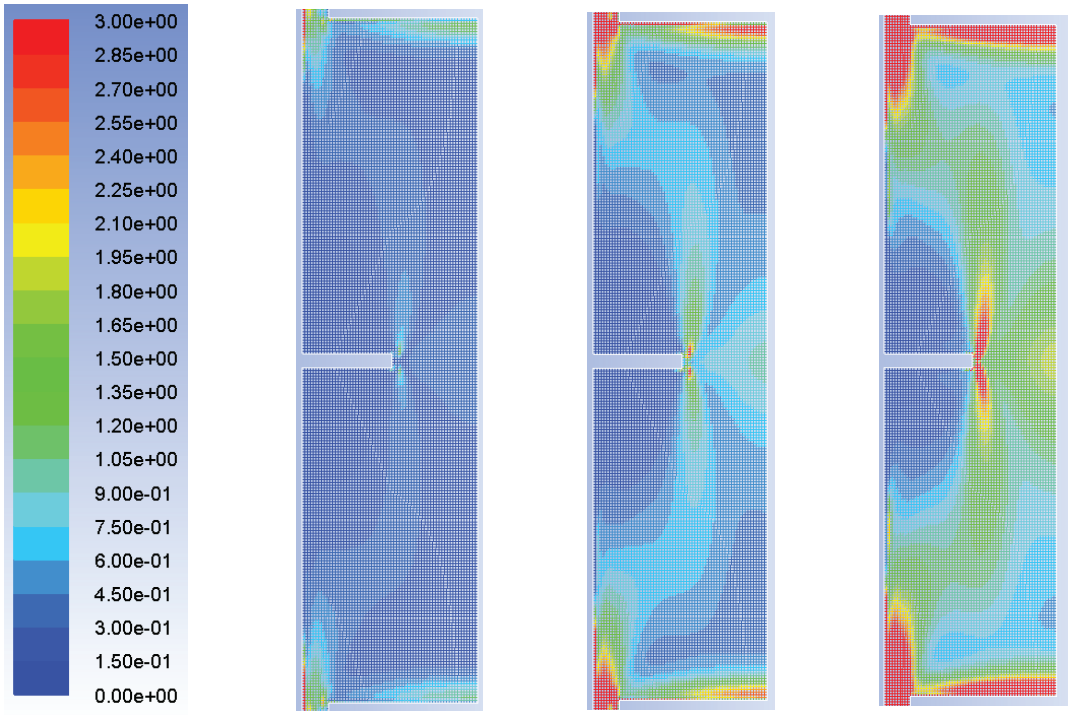


Figure 6.6: Time-averaged turbulent dissipation rate distribution in a compartment for a continuous phase flowrate of 100 ml/min and pulsations of 3.5 cm/s (left), 4.5 cm/s (centre) and 5.5 cm/s (right).

The time-averaged turbulent dissipation rates ε are reported as function of the experimental pulsations and continuous phase flowrates in Table 6.2.

Table 6.2: Time-averaged value of the turbulent dissipation rate in a compartment of the pulsed column as function of the experimental pulsations and continuous phase flowrates.

		Pulsation (cm/s)		
		3.5	**4.5**	**5.5**
Continuous-phase flowrate (ml/min)	**0**	0.25	0.6	1.11
	50	0.26	0.61	1.12
	100	0.27	0.63	1.13

Finally, the probability density functions of ε were extracted for the different pulsations and continuous phase flowrates (Fig. 6.7). These functions, as well as the value of the turbulent kinetic energy k, were implemented in the MATLAB program in order to compute the breakage and coalescence rates of the 1D PBE model.

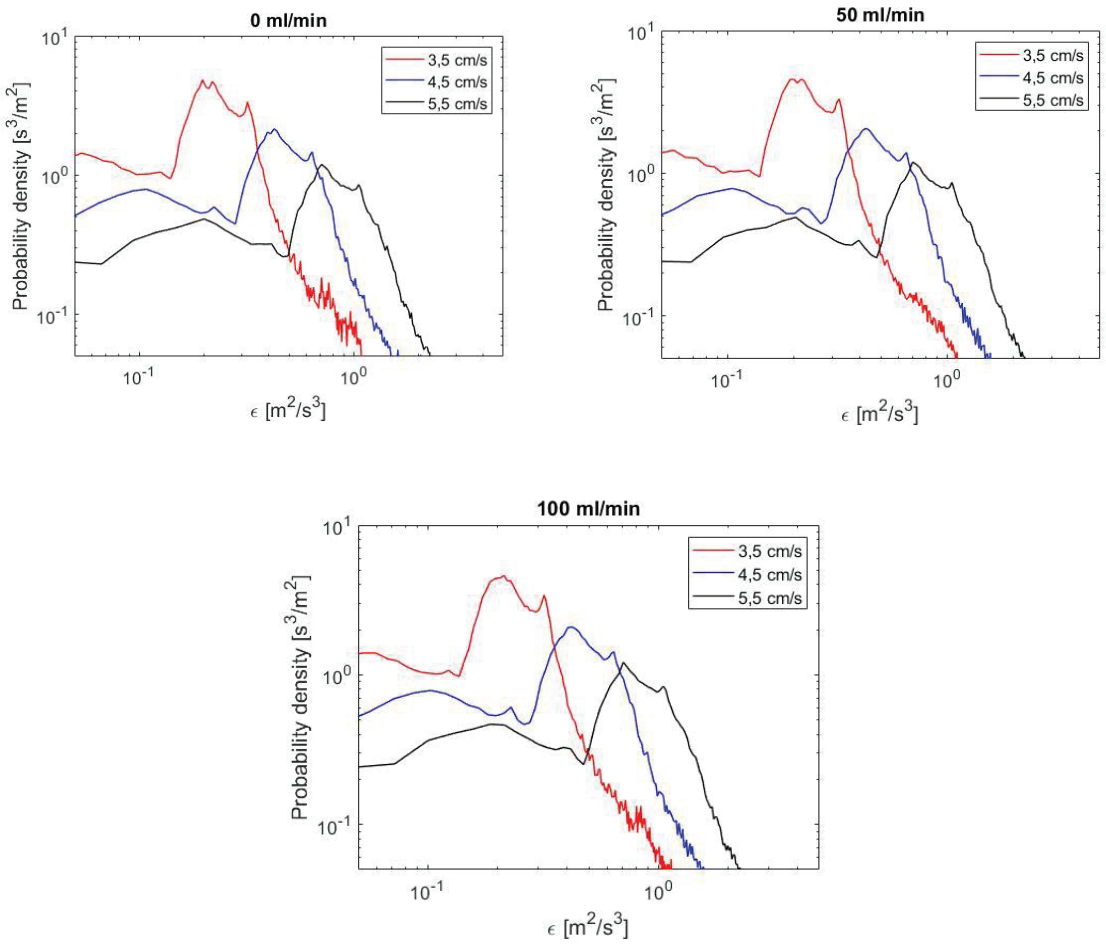


Figure 6.7: Probability density functions of ε for pulsations of 3.5, 4.5, 5.5 cm/s at continuous phase flowrates of 0 (top-left), 50 (top-right) and 100 (bottom) ml/min

6.3.2. Identification of the parameter values

Once the probability density functions of ε had been obtained, the parameter identification was performed. Although the kernel parameters were already identified in Chapter 5, the differences in the flow characteristics and in the geometry of the liquid-liquid contactor lead to

the need of a new parameter identification. Indeed, preliminary computations with the previously identified parameters did not allow to reproduce the experimental data.

The parameter identification was accomplished through the experiment characterized by a pulsation of 3.5 cm/s, a dispersed phase flowrate of 50 ml/min and a continuous phase flowrate equal to zero.

The parameter identification was performed in a MATLAB routine containing the 1D PBE pulsed column model, in which the probability density function corresponding to a pulsation of 3.5 cm/s was implemented. The *patternsearch* function (Global Optimization Toolbox) was employed in order to minimize the error of the target function, which was defined as:

$$J = \left(\frac{d_{32exp} - d_{32sim}}{d_{32exp}}\right)^2 + \left(\frac{\phi_{exp} - \phi_{sim}}{\phi_{exp}}\right)^2$$

An accurate fitting of the experimental data was obtained, with a relative error on the Sauter mean diameter of 1.4% and of 1.1% for the dispersed phase volume fraction (Tab. 6.3).

Table 6.3: Experimental and simulated Sauter mean diameters and dispersed phase volume fraction considering a dispersed phase flowrate of 50 ml/min, a pulsation of 3.5 cm/s and a continuous phase flowrate equal to zero.

	Experimental	**Simulation**	**Rel. error (%)**
$\boldsymbol{d_{32}}$ $[\boldsymbol{mm}]$	2.074	2.102	1.4
$\boldsymbol{\phi_d}$	2.6	2.63	1.2

The identified parameters are reported in Tab. 6.4. The procedure took 5 hours on an Intel Xeon dual-core machine (3.20 GHz) with 64GB of RAM.

Table 6.4: Parameters identified through the *patternsearch* function

C_1	C_2	C_3	C_4
6.10e-3	4.09e-2	9.99e2	5.32e20

6.3.3. Validation of the model

In order to validate the model together with the identified parameters, the 1D PBE pulsed column model was used to reproduce the experimental data obtained at different pulsations and dispersed and continuous phase flowrates.

The model was primarily tested on the experiments characterized by the same dispersed and continuous phase flowrates (respectively, 50 ml/min and 0ml/min) employed for the parameter identification, but at higher pulsations (4.5 and 5.5 cm/s). The simulations were run by implementing in the MATLAB routine the probability density functions of ε at the considered pulsations. The higher pulsation intensities caused a more intense turbulence inside the pulsed column, leading to smaller Sauter mean diameters and bigger dispersed phase volume fractions. In both cases, the model is capable to accurately reproduce the decrease in the Sauter mean diameters and the increase in the dispersed phase volume fractions (Tab. 6.5). Indeed, the simulated Sauter mean diameters presented average relative errors of, respectively, 7.3% and 3.1%, while the simulated dispersed phase volume fractions of 5.3% and 6.8%.

Table 6.5: Experimental and simulated Sauter mean diameters and dispersed phase volume fraction considering a dispersed phase flowrate of 50 ml/min, pulsations of 4.5 and 5.5 cm/s and a continuous phase flowrate equal to zero.

	Experimental	**Simulation**	
Pulsation $\left[\frac{cm}{s}\right]$	**4.5**		**Rel. error (%)**
d_{32} $[mm]$	1.219	1.183	3.0
ϕ_d**(%)**	3.20	3.08	3.8
Pulsation $\left[\frac{cm}{s}\right]$	**5.5**		**Rel. error (%)**
d_{32} $[mm]$	0.672	0.601	10.6
ϕ_d	3.90	3.81	2.3

The model was later tested on the experiments performed at dispersed phase flowrates of 60 ml/min (Tab. 6.6) and 70 ml/min (Tab. 6.7) and pulsation intensities of 3.5, 4.5 and 5.5 cm/s. The higher flowrates led to an increase in the dispersed phase volume fractions and to a higher number of droplets inside the column. In both cases, the model well reproduced the experimental data; indeed, the simulated Sauter mean diameters presented an average error lower than 15%, and the simulated dispersed phase volume fraction lower than 10%.

Table 6.6: Experimental and simulated Sauter mean diameters and dispersed phase volume fraction considering a dispersed phase flowrate of 60 ml/min, pulsations of 3.5, 4.5 and 5.5 cm/s and a continuous phase flowrate equal to zero.

	Experimental	**Simulation**	
Pulsation $\left[\frac{cm}{s}\right]$	**3.5**		**Rel. error (%)**
d_{32} $[mm]$	1.995	2.096	5.1
ϕ_d**(%)**	3.10	3.17	4.5
Pulsation $\left[\frac{cm}{s}\right]$	**4.5**		**Rel. error (%)**
d_{32} $[mm]$	1.109	1.177	8.2
ϕ_d	3.80	3.71	2.4
Pulsation $\left[\frac{cm}{s}\right]$	**5.5**		**Rel. error (%)**
d_{32} $[mm]$	0.665	0.597	10.2
ϕ_d	4.40	4.61	4.5

Table 6.7: Experimental and simulated Sauter mean diameters and dispersed phase volume fraction considering a dispersed phase flowrate of 70 ml/min, pulsations of 3.5, 4.5 and 5.5 cm/s and a continuous phase flowrate equal to zero.

	Experimental	**Simulation**	
Pulsation $\left[\frac{cm}{s}\right]$	**3.5**		**Rel. error (%)**
d_{32} $[mm]$	1.928	2.090	8.4
ϕ_d**(%)**	3.50	3.71	5.9
Pulsation $\left[\frac{cm}{s}\right]$	**4.5**		**Rel. error (%)**
d_{32} $[mm]$	1.048	1.170	11.6
ϕ_d	4.20	4.35	3.6
Pulsation $\left[\frac{cm}{s}\right]$	**5.5**		**Rel. error (%)**
d_{32} $[mm]$	0.649	0.593	8.6
ϕ_d	5.10	5.40	5.9

The second part of model validation dealt with experiments performed considering a non-zero counter-current continuous phase flow. The experiments consisted of continuous phase flow of 50 (Tab. 6.8) and 100 ml/min (Tab. 6.9), a dispersed phase flowrate of 50 ml/min and pulsation intensities of 3.5, 4.5 and 5.5 cm/s (Tab. 6.2).

Table 6.8: Experimental and simulated Sauter mean diameters and dispersed phase volume fraction considering a dispersed phase flowrate of 50 ml/min, pulsations of 3.5, 4.5 and 5.5 cm/s and a continuous phase flowrate equal to 50 ml/min.

	Experimental	**Simulation**	
Pulsation $\left[\frac{cm}{s}\right]$	**3.5**		**Rel. error (%)**
d_{32} $[mm]$	1.876	2.048	9.2
ϕ_d**(%)**	2.90	2.70	6.9
Pulsation $\left[\frac{cm}{s}\right]$	**4.5**		**Rel. error (%)**
d_{32} $[mm]$	1.008	1.081	7.2
ϕ_d	3.50	3.21	5.6
Pulsation $\left[\frac{cm}{s}\right]$	**5.5**		**Rel. error (%)**
d_{32} $[mm]$	0.621	0.545	12.2
ϕ_d	4.20	4.04	3.8

Table 6.9: Experimental and simulated Sauter mean diameters and dispersed phase volume fraction considering a dispersed phase flowrate of 50 ml/min, pulsations of 3.5, 4.5 and 5.5 cm/s and a continuous phase flowrate equal to 100 ml/min.

	Experimental	**Simulation**	
Pulsation $\left[\frac{cm}{s}\right]$	**3.5**		**Rel. error (%)**
d_{32} $[mm]$	1.717	1.975	15.0
ϕ_d**(%)**	3.00	2.76	8.0
Pulsation $\left[\frac{cm}{s}\right]$	**4.5**		**Rel. error (%)**
d_{32} $[mm]$	0.914	1.016	11.4
ϕ_d	3.70	3.32	10.3
Pulsation $\left[\frac{cm}{s}\right]$	**5.5**		**Rel. error (%)**
d_{32} $[mm]$	0.599	0.488	18.5
ϕ_d	4.5	4.33	9.8

The counter-current continuous phase flowrate is observed to slow down the falling droplets, which accumulated along the pulsed column, leading to higher dispersed phase volume fractions compared to analogous experiments conducted without a counter-current flowrate. The Sauter mean diameters, instead, decreased since the droplets had a higher residence time inside the column, being therefore exposed to the turbulent stresses for longer periods. The model predicts the Sauter mean diameters with relative errors lower than 13% for a continuous phase flowrate of 50 ml/min and 20% for 100 ml/min. The dispersed phase volume fractions are predicted with a relative error lower than, respectively, of 7% and 11%.

6.4. Conclusions

In this work, a 1D Population Balance Equation model is proposed for simulating the hydrodynamic behavior of the dispersed phase in a pulsed column. The model is based on a finite difference scheme method. The source terms are discretized through the Fixed Pivot Method proposed by Kumar and Ramkrishna. Generalized kernels have been considered in the computation of coalescence and breakage rates. These models are extended to the entire spectrum of the turbulence through a more refined second-order structure function and an energy spectrum developed for all the eddy scales. The turbulent inhomogeneities in the pulsed column, caused by the summing up effects of the pulsation and the continuous phase flowrate, have been accounted through the probability density functions of the turbulent dissipation rate, which were obtained through single-phase CFD simulations of the liquid-liquid contactor.

Liquid-liquid dispersion experiments were carried out in the pulsed column in order to test and validate the model. Firstly, the parameters of the generalized kernels were identified by fitting of experimental data. The model along with the identified parameters has been tested on the other experiments. The model showed a good accuracy in the prediction of the Sauter mean diameters and the dispersed phase volume fractions. Indeed, the maximum relative errors were always lower than 20%. If compared to the empirical correlations present in the literature [4], the proposed model presents several advantages. Indeed, it can be applied to a wider range of operating conditions since it was derived on theoretical basis and not on empirical ones. It can be employed to simulate any extraction column, once the probability density functions of the turbulent dissipation rate ε are provided. Finally, the relative errors made by computing the Sauter mean diameter and the dispersed phase volume fraction through the model are generally lower (< 20%) than the ones done through the empirical correlations (at least 20%, [4]).

7. Conclusions & Perspectives

The main objective of this work was to study and ameliorate the models employed for the computation of the breakage and coalescence rates in turbulent liquid-liquid dispersions. An accurate solution of the Population Balance Equation depends on the breakage and coalescence kernels. Here, the Coulaloglou and Tavlarides models were considered, since it was reported in the literature that these kernels were capable to well reproduce the experimental data of turbulent liquid-liquid dispersions.

The PBE model is strongly influenced by the flow in the liquid-liquid extractor. Indeed, the breakage and coalescence kernels are function of the turbulent kinetic energy dissipation rate ε. Therefore, the PBE is normally coded in a CFD solver and solved along with the Navier-Stokes equations. Although CFD-PBE coupling represents the best approach to account for the flow characteristics in the PBE solution, this method requires huge computational resources and simulation times, which is not suitable for industrial applications. Therefore, in this work, a simplified 0D PBE was considered. In order to account for the ε inhomogeneities, single-phase CFD simulations of the liquid-liquid extractor were run and the probability density functions of ε were extracted. These functions were used to compute volume-averaged kernels, which allowed to consider the turbulence inhomogeneities in a 0D PBE. In order to validate the model, turbulent liquid-liquid dispersion experiments at low viscosity were performed in a stirred tank reactor. The model was capable to well reproduce the obtained experimental data at different turbulent conditions, dispersed phase volume fractions and dispersion configurations (direct or inverse).

The following part of the study dealt with the turbulent liquid-liquid dispersions characterized by higher viscosities of the continuous phase, in order to mimic typical conditions occurring in the nuclear fuel treatment process. Indeed, during the solvent extraction, the viscosity of the organic phase increases due to the higher and higher concentration of uranium. Therefore, experiments at higher continuous phase viscosities were performed. In this case, the model validated at lower viscosities was not able to reproduce the experimental data. Indeed, one of the main assumptions in formulating kernels is that the droplets in the dispersion have dimensions in the inertial subrange of turbulence. It was shown that at higher viscosities this assumption did not hold anymore. Consecutively, the breakage and coalescence models were

generalized to the entire turbulence spectrum by considering a refined second-order structure function. The generalized models allowed to reproduce the experimental data both at higher and lower viscosities.

The last part of the work dealt with the study of the behavior of a droplet dispersion in a pulsed column. A model to describe the hydrodynamics in this liquid-liquid extractor was proposed and validated through experiments. The model is based on a 1D-PBE, which considers the inhomogeneity of the number density function along the axial coordinate (which is the main coordinate). The breakage and coalescence kernels were computed according to the improvements previously proposed. In order to compute the volume-averaged generalized kernels, single-phase CFD simulations of the pulsed column were run and the probability density functions of ε were extracted. The droplet velocities, which were function of the droplet diameters, were computed according to an empirical correlation proposed in the literature. Finally, the model allowed to well reproduce the dispersion experiments carried out in the pulsed column at different pulsations and dispersed and continuous phase flow rates.

Following the improvements in the breakage and coalescence kernels, achieved through a better description of the hydrodynamics of the turbulent liquid-liquid dispersion, the next step may deal with the study of the mass transfer. A first possibility is to consider a simplified plug-flow model both for the continuous and the dispersed phase, where the interfacial area and the dispersed phase volume fraction are obtained by the proposed 1D-PBE model. In the case this model would not provide accurate results, a 2D-PBE model could be developed and employed. In this case, the breakage and coalescence kernels may also depend on the droplet solute concentration; therefore, more studies on these models should be carried out to better predict the rates of these phenomena.

Annex I

In the following Annex, the SOPAT software is detailed. This software is composed of modules that allow to perform different tasks. These modules are:

- Probe controller
- Sample
- Batcher
- Result Analyzer

The "Probe Controller" permits to set-up the probe. The parameters are the focus position, the strobe intensity, and the gain (Fig. I). The focus position indicates the distance between the acquisition plane and the probe lens. A low value of this parameter leads to the capture of the droplet in the very close vicinity of the lens. The strobe intensity is proportional to the intensity of the light emitted by the probe. A low value of this parameter is needed to obtain good quality images. In the case of concentrated dispersed phase, this parameter could take higher values. The gain also deals with the luminosity of the acquired images. This parameter has to be modified when the maximum strobe intensity does not lead to clear images. In the performed experiments, the gain was never changed, since tuning the strobe intensity was enough to obtain good images.

The number of acquired images can be defined in the "Triggering" window (Fig. I). The frame rate indicates the number of images acquired per second of acquisition. Frame rates between 4-7 Hz are suggested and employed in this work. Lower values would lead to longer acquisition periods. Higher values, instead, could lead to the presence of the same droplets in two consecutive images, since the droplets may not have the time to leave the acquisition plane.

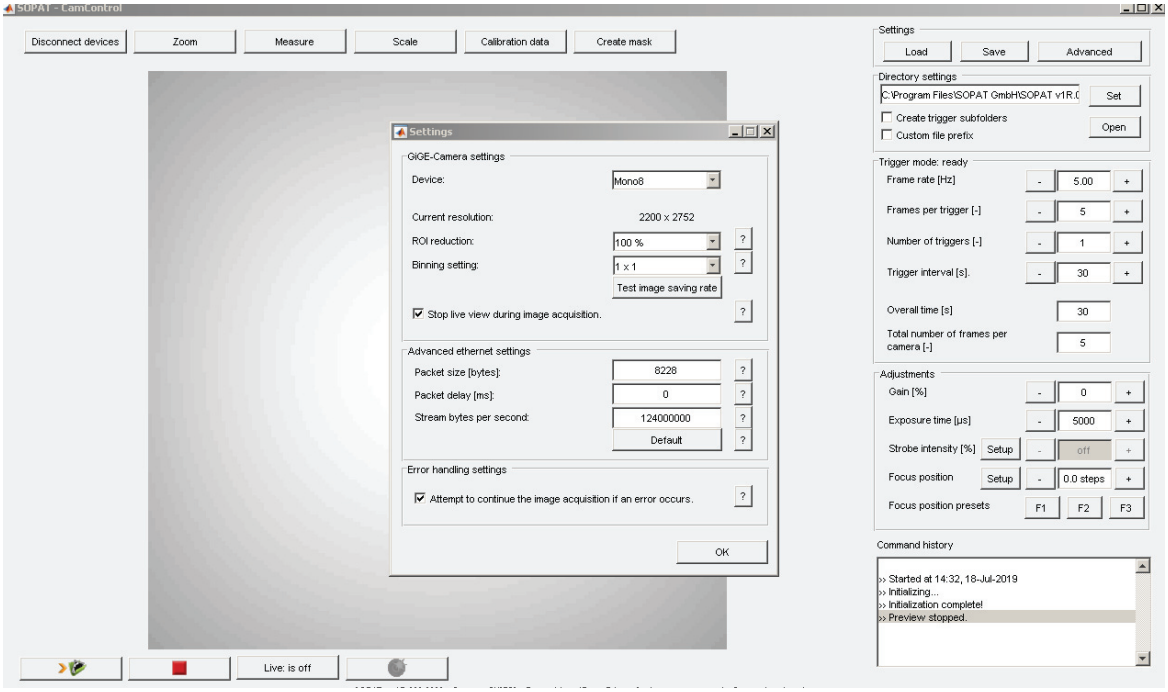


Figure I: Parameter set-up of the SOPAT endoscopic probe

Once acquired, the images have to be processed. The software required the manual selection of typical droplets, for training, that it will later consider as representative of the object to detect in the acquired images (learning step). This operation can be performed through the "Sample" module (Fig. II). The manually selected droplets must have well-defined borders. It has been remarked that three droplets of different sizes (small, medium, large) had to be selected to ensure a good training. Besides this, the minimum droplet size (in pixel) must be defined. A value between 7-10 pixels is suggested, since the conversion factor is equal to 3,6 µm/pixel. This means that the software is able to detect droplets bigger than 20-30 µm. Indeed, lower values lead to the detection by the software of non-existent droplets. The last parameter to be defined is the "candidate threshold". Reducing the value of this parameter leads to the selection by the software of more blurred droplets. An optimal value of the "candidate threshold" allows the detection of a large number of real droplets. A value between 0.37-0.45 was chosen. Once all the parameters and the droplets are selected, the automatic detection is initiated by running "find particles" and "apply it to all the images" to get a preview of the droplet detection by the software. If the result is satisfying, clicking on "generate input parameters" the files .pss and

.psp that will be employed in the "Batcher" module will be generated. In the "Batch" module, the folders containing the images that have to be processed are uploaded.



Figure II: Droplet selection in the "Sample" module

After the "Batcher" module has completed the image processing, the results can be analyzed in the "Result Analyzer" module (Fig. III). In this window, many properties of the analyzed images can be obtained, as the number droplet size distribution or the Sauter mean diameter. The data are later exported and treated in the MATLAB routine solving the PBE.

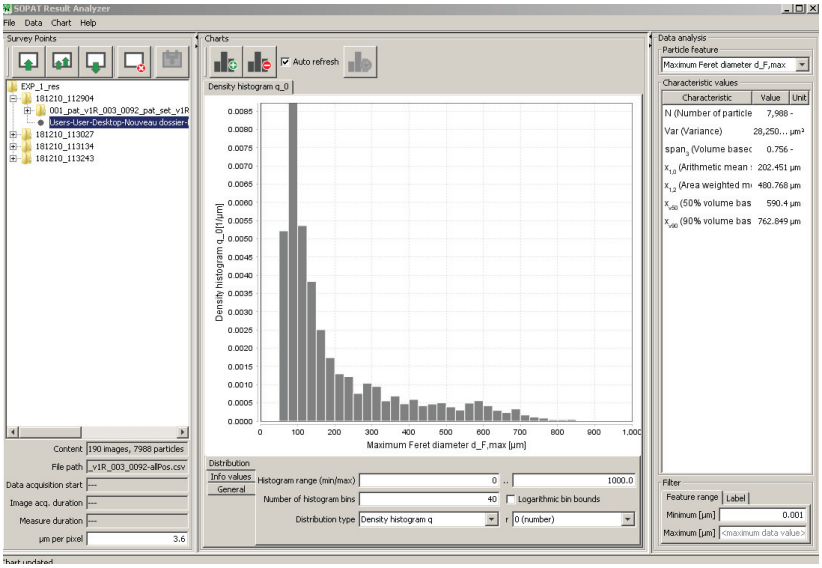


Figure III: Representation of the number droplet distribution function in the "Result Analyzer" module

Annex II

In this Annex, the way on how to get the time-averaged PDF of ε in a compartment of the pulsed column from a CFD simulation is shown. Since the flow in the pulsed column is periodic, the value of ε in a point of the pulsed column varies during the pulsation period. For this reason, a time-averaged PDFs of ε have been considered.

In the ANSYS Fluent software, a "Custom Field Function" equal to the turbulent dissipation rate ε has to be defined (Fig. I).

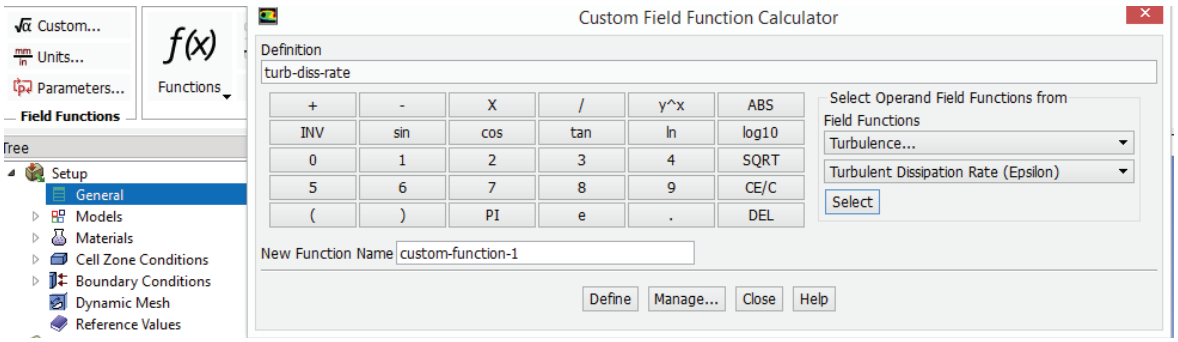


Figure I: Definition of the "Custom Field Function"

Then, before running the simulation, the "Data Sampling for Time Statistics" in the module "Run Calculation" has to be selected, and in the "Sampling Option" box, the custom-function highlighted (Fig. II).

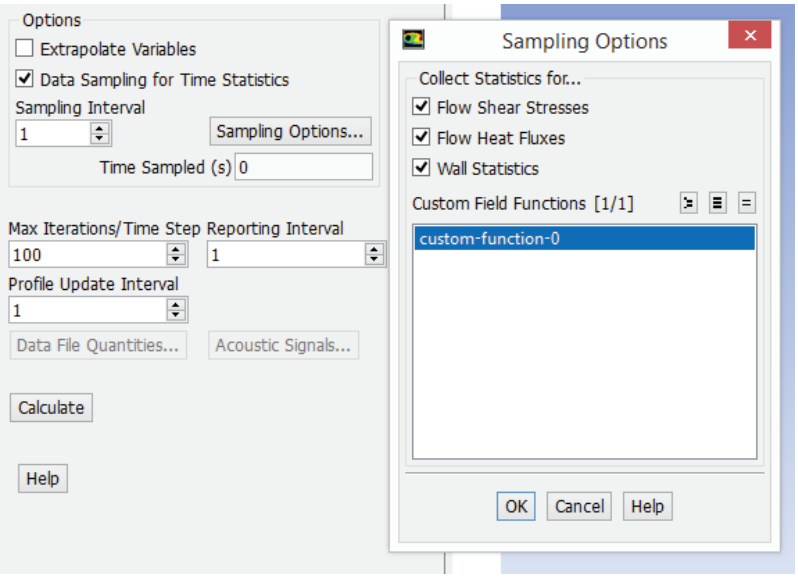


Figure II: "Data sampling" of the turbulent dissipation rate

Once the simulation is completed, it is possible to extract the histogram representing the time-averaged probability of ε in the central compartment of the pulsed column. In order to do this, in the "Results" module, the histogram can be created and printed in the console by selecting the "Unsteady statistics" of the "Mean-custom-function" (Fig. III).

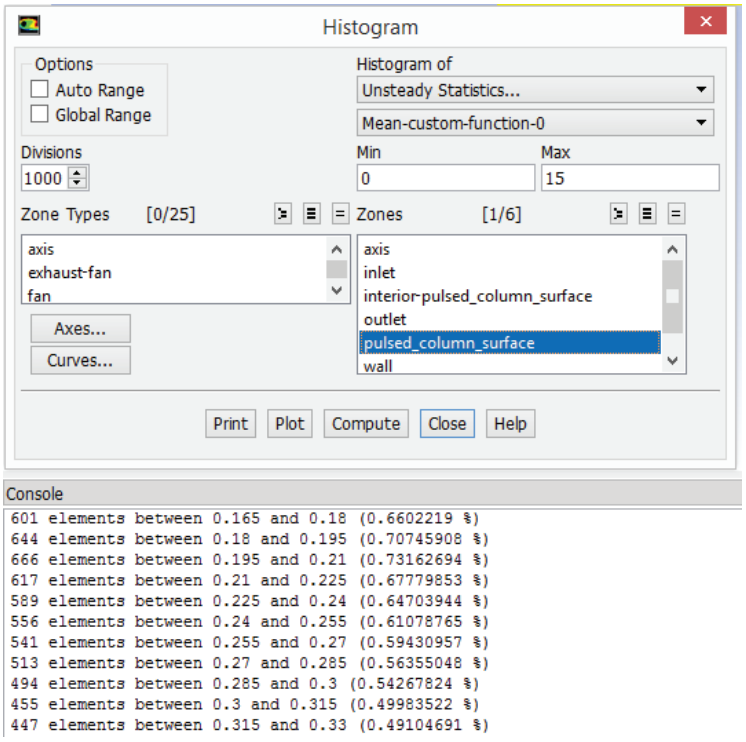


Figure III: Definition of the histogram of ε

Once the probability values of ε have been acquired, it is possible to build the time-averaged PDF of ε by dividing the probability values of having ε in $[\varepsilon, \varepsilon + \Delta\varepsilon]$ by the range $\Delta\varepsilon$. The PDF will be later implemented in the MATLAB routine for the computation of the volume-averaged breakage and coalescence kernels.

Notation

C_1, C_2	Coulaloglou and Tavlarides breakage kernel parameters
C_3, C_4	Coulaloglou and Tavlarides coalescence kernel parameters
d	droplet diameter (m)
D	stirrer diameter (m)
D_t	turbulent diffusivity of the dispersed phase (m^2/s)
f	probability density function
$h(v,v')$	collision frequency
k	turbulent kinetic energy (m^2/s^2)
m_r	mass of fluid in the reactor (kg)
$n(v)$	number density function ($1/m^6$)
N	droplet number
N_p	Power number
N_r	rotational speed (tr/s)
p	pivot of i^{th} cell (m^3)
P	pressure (Pa)
P	dissipated power (W)
$Q(v,v')$	coalescence kernel (1/s)

$s(\boldsymbol{x}, v, t)$	PBE source term
t	time (s)
T	stirred tank diameter (m)
u	velocity of the continuous phase (m/s)
v	droplet volume (m^3)
V	volume of fluid (m^3)
$\boldsymbol{x}$	Cartesian space coordinates
β	daughter size distribution function
Γ	breakup kernel (1/s)
λ	collision efficiency
μ	viscosity (Pa·s)
μ_t	turbulent eddy viscosity (Pa·s)
ε	turbulent kinetic energy dissipation rate (m^2/s^3)
ρ	density (kg/m^3)
σ	interfacial tension (N/m)
$\boldsymbol{\varphi}$	dispersed phase internal coordinates
$\boldsymbol{\phi}$	dispersed phase volume fraction

Bibliography

[1] J.D. Seader, E.J. Henley, D.K. Roper, Separation process principles: chemical and biochemical operations, 3rd ed, Wiley, Hoboken, NJ, 2011.

[2] J.M. Mckibben, Chemistty of the Purex Process, Radiochim. Acta. 36 (1984). doi:10.1524/ract.1984.36.12.3.

[3] A.W. Pacek, C.C. Man, A.W. Nienow, On the Sauter mean diameter and size distributions in turbulent liquid/liquid dispersions in a stirred vessel, Chem. Eng. Sci. 53 (1998) 2005–2011. doi:10.1016/S0009-2509(98)00068-2.

[4] S. Mohanty, Modeling of liquid-liquid extraction column: a review, Rev. Chem. Eng. 16 (2000). doi:10.1515/REVCE.2000.16.3.199.

[5] K. Sreenivasulu, D. Venkatanarasaiah, Y.B.G. Varma, Drop size distributions in liquid pulsed columns, Bioprocess Eng. 17 (1997) 189. doi:10.1007/s004490050374.

[6] D.L. Marchisio, R.O. Fox, Computational Models for Polydisperse Particulate and Multiphase Systems, Cambridge University Press, Cambridge, 2013. doi:10.1017/CBO9781139016599.

[7] D. Ramkrishna, Population balances: theory and applications to particulate systems in engineering, Academic Press, San Diego, CA, 2000.

[8] V. Alopaeus, J. Koskinen, K. I. Keskinen, J. Majander, Simulation of the population balances for liquid–liquid systems in a nonideal stirred tank. Part 2—parameter fitting and the use of the multiblock model for dense dispersions, Chem. Eng. Sci. 57 (2002) 1815–1825. doi:10.1016/S0009-2509(02)00067-2.

[9] H. Luo, H.F. Svendsen, Theoretical model for drop and bubble breakup in turbulent dispersions, AIChEJ. 42 (1996) 1225–1233. doi:10.1002/aic.690420505.

[10] C.A. Coulaloglou, L.L. Tavlarides, Description of interaction processes in agitated liquid-liquid dispersions, Chem. Eng. Sci. 32 (1977) 1289–1297. doi:10.1016/0009-2509(77)85023-9.

[11] T. Wang, J. Wang, Y. Jin, A novel theoretical breakup kernel function for bubbles/droplets in a turbulent flow, Chem. Eng. Sci. 58 (2003) 4629–4637. doi:10.1016/j.ces.2003.07.009.

[12] Y. Liao, D. Lucas, A literature review on mechanisms and models for the coalescence process of fluid particles, Chem. Eng. Sci. 65 (2010) 2851–2864. doi:10.1016/j.ces.2010.02.020.

[13] Y. Liao, D. Lucas, A literature review of theoretical models for drop and bubble breakup in turbulent dispersions, Chem. Eng. Sci. 64 (2009) 3389–3406. doi:10.1016/j.ces.2009.04.026.

[14] J.C. Lasheras, C. Eastwood, C. Martínez-Bazán, J.L. Montañés, A review of statistical models for the break-up of an immiscible fluid immersed into a fully developed turbulent flow, Int. J. Multiph. Flow. 28 (2002) 247–278. doi:10.1016/S0301-9322(01)00046-5.

[15] C. Martínez-Bazán, J.L. Montañés, J.C. Lasheras, On the breakup of an air bubble injected into a fully developed turbulent flow. Part 1. Breakup frequency, J. Fluid Mech. 401 (1999) 157–182. doi:10.1017/S0022112099006680.

[16] R.V. Calabrese, T.P.K. Chang, P.T. Dang, Drop breakup in turbulent stirred-tank contactors. Part I: Effect of dispersed-phase viscosity, AIChEJ. 32 (1986) 657–666. doi:10.1002/aic.690320416.

[17] A. Amokrane, S. Charton, N. Sheibat-Othman, J. Becker, J.P. Klein, F. Puel, Development of a CFD-PBE coupled model for the simulation of the drops behaviour in a pulsed column, Can. J. Chem. Eng. 92 (2014) 220–233. doi:10.1002/cjce.21933.

[18] A. Buffo, D.L. Marchisio, M. Vanni, P. Renze, Simulation of polydisperse multiphase systems using population balances and example application to bubbly flows, Chem. Eng. Res. Des. 91 (2013) 1859–1875. doi:10.1016/j.cherd.2013.06.021.

[19] T. Wang, J. Wang, Numerical simulations of gas–liquid mass transfer in bubble columns with a CFD–PBM coupled model, Chem. Eng. Sci. 62 (2007) 7107–7118. doi:10.1016/j.ces.2007.08.033.

[20] A. Buffo, J. De Bona, M. Vanni, D.L. Marchisio, Simplified volume-averaged models for liquid–liquid dispersions: Correct derivation and comparison with other approaches, Chem. Eng. Sci. 153 (2016) 382–393. doi:10.1016/j.ces.2016.07.032.

[21] A. Prosperetti, G. Tryggvason, Computational methods for multiphase flow, Cambridge University Press, 2007.

[22] S. Castellano, N. Sheibat-Othman, D. Marchisio, A. Buffo, S. Charton, Description of droplet coalescence and breakup in emulsions through a homogeneous population balance model, Chem. Eng. J. 354 (2018) 1197–1207. doi:10.1016/j.cej.2018.07.176.

[23] M. Vanni, Approximate Population Balance Equations for Aggregation–Breakage Processes, J. Colloid Interface Sci. 221 (2000) 143–160. doi:10.1006/jcis.1999.6571.

[24] S. Kumar, D. Ramkrishna, On the solution of population balance equations by discretization—I. A fixed pivot technique, Chem. Eng. Sci. 51 (1996) 1311–1332. doi:10.1016/0009-2509(96)88489-2.

[25] F. Gelbard, Y. Tambour, J.H. Seinfeld, Sectional representations for simulating aerosol dynamics, J. Colloid Interface Sci. 76 (1980) 541–556. doi:10.1016/0021-9797(80)90394-X.

[26] M.J. Hounslow, R.L. Ryall, V.R. Marshall, A discretized population balance for nucleation, growth, and aggregation, AIChEJ. 34 (1988) 1821–1832. doi:10.1002/aic.690341108.

[27] J.D. Lister, D.J. Smit, M.J. Hounslow, Adjustable discretized population balance for growth and aggregation, AIChEJ. 41 (1995) 591–603. doi:10.1002/aic.690410317.

[28] S. Kumar, D. Ramkrishna, On the solution of population balance equations by discretization—II. A moving pivot technique, Chem. Eng. Sci. 51 (1996) 1333–1342. doi:10.1016/0009-2509(95)00355-X.

[29] F. Filbet, P. Laurençot, Numerical Simulation of the Smoluchowski Coagulation Equation, SIAM J. Sci. Comput. 25 (2004) 2004–2028. doi:10.1137/S1064827503429132.

[30] J. Kumar, M. Peglow, G. Warnecke, S. Heinrich, L. Mörl, Improved accuracy and convergence of discretized population balance for aggregation: The cell average technique, Chem. Eng. Sci. 61 (2006) 3327–3342. doi:10.1016/j.ces.2005.12.014.

[31] D.L. Marchisio, R.D. Vigil, R.O. Fox, Quadrature method of moments for aggregation–breakage processes, J. Colloid Interface Sci. 258 (2003) 322–334. doi:10.1016/S0021-9797(02)00054-1.

[32] D.L. Marchisio, J.T. Pikturna, R.O. Fox, R.D. Vigil, A.A. Barresi, Quadrature method of moments for population-balance equations, AIChEJ. 49 (2003) 1266–1276. doi:10.1002/aic.690490517.

[33] D.L. Marchisio, R.O. Fox, Solution of population balance equations using the direct quadrature method of moments, J. Aerosol Sci. 36 (2005) 43–73. doi:10.1016/j.jaerosci.2004.07.009.

[34] C. Yuan, F. Laurent, R.O. Fox, An extended quadrature method of moments for population balance equations, J. Aerosol Sci. 51 (2012) 1–23. doi:10.1016/j.jaerosci.2012.04.003.

[35] C. Yuan, R.O. Fox, Conditional quadrature method of moments for kinetic equations, J. Comput. Phys. 230 (2011) 8216–8246. doi:10.1016/j.jcp.2011.07.020.

[36] R. McGraw, Description of Aerosol Dynamics by the Quadrature Method of Moments, Aerosol Sci. Technol. 27 (1997) 255–265. doi:10.1080/02786829708965471.

[37] Y. Lin, K. Lee, T. Matsoukas, Solution of the population balance equation using constant-number Monte Carlo, Chem. Eng. Sci. 57 (2002) 2241–2252. doi:10.1016/S0009-2509(02)00114-8.

[38] P. Tandon, D.E. Rosner, Monte Carlo Simulation of Particle Aggregation and Simultaneous Restructuring, J. Colloid Interface Sci. 213 (1999) 273–286. doi:10.1006/jcis.1998.6036.

[39] D. Ramkrishna, The Status of Population Balances, Rev. Chem. Eng. 3 (1985). doi:10.1515/REVCE.1985.3.1.49.

[40] K. Lee, T. Matsoukas, Simultaneous coagulation and break-up using constant-N Monte Carlo, Powder Technol. 110 (2000) 82–89. doi:10.1016/S0032-5910(99)00270-3.

[41] H.M. Vale, T.F. McKenna, Solution of the Population Balance Equation for Two-Component Aggregation by an Extended Fixed Pivot Technique, Ind. Eng. Chem. Res. 44 (2005) 7885–7891. doi:10.1021/ie050179s.

[42] J. Kumar, G. Warnecke, M. Peglow, S. Heinrich, Comparison of numerical methods for solving population balance equations incorporating aggregation and breakage, Powder Technol. 189 (2009) 218–229. doi:10.1016/j.powtec.2008.04.014.

[43] P.A. Davidson, Turbulence: an introduction for scientists and engineers, Oxford University Press, Oxford, UK ; New York, 2004.

[44] S.B. Pope, Turbulent flows, Cambridge University Press, Cambridge ; New York, 2000.

[45] G.K. Batchelor, The theory of homogeneous turbulence, Cambridge University Press, Cambridge ; New York, 1982.

[46] G.K. Batchelor, Diffusion in a field of homogeneous turbulence, Math. Proc. Camb. Philos. Soc. 48 (1952) 345–362. doi:10.1017/S0305004100027687.

[47] R.P. Hesketh, T.W. Fraser Russell, A.W. Etchells, Bubble size in horizontal pipelines, AIChE J. 33 (1987) 663–667. doi:10.1002/aic.690330414.

[48] J. Baldyga, W. Podgórska, Drop break-up in intermittent turbulence: Maximum stable and transient sizes of drops, Can. J. Chem. Eng. 76 (1998) 456–470. doi:10.1002/cjce.5450760316.

[49] K.J. Valentas, N.R. Amundson, Breakage and Coalescence in Dispersed Phase Systems, Ind. Eng. Chem. Fundam. 5 (1966) 533–542. doi:10.1021/i160020a018.

[50] R. Andersson, B. Andersson, On the breakup of fluid particles in turbulent flows, AIChE J. 52 (2006) 2020–2030. doi:10.1002/aic.10831.

[51] Reuel. Shinnar, J.M. Church, Statistical Theories of Turbulence in Predicting Particle Size in Agitated Dispersions, Ind. Eng. Chem. 52 (1960) 253–256. doi:10.1021/ie50603a036.

[52] H. Sovová, Breakage and coalescence of drops in a batch stirred vessel—II comparison of model and experiments, Chem. Eng. Sci. 36 (1981) 1567–1573. doi:10.1016/0009-2509(81)85117-2.

[53] W.J. Howarth, Coalescence of drops in a turbulent flow field, Chem. Eng. Sci. 19 (1964) 33–38. doi:10.1016/0009-2509(64)85003-X.

[54] A. Amokrane, S. Maaß, F. Lamadie, F. Puel, S. Charton, On droplets size distribution in a pulsed column. Part I: In-situ measurements and corresponding CFD–PBE simulations, Chem. Eng. J. 296 (2016) 366–376. doi:10.1016/j.cej.2016.03.089.

[55] E.L. Paul, V.A. Atiemo-Obeng, S.M. Kresta, eds., Handbook of industrial mixing: science and practice, Wiley-Interscience, Hoboken, N.J, 2004.

[56] N. Harnby, M.F. Edwards, A.W. Nienow, eds., Mixing in the process industries, 2nd ed., Butterworth-Heinemann, Oxford ; Boston, 1997.

[57] I. Houcine, E. Plasari, R. David, Effects of the Stirred Tank's Design on Power Consumption and Mixing Time in Liquid Phase, Chem. Eng. Technol. 23 (2000) 605–613. doi:10.1002/1521-4125(200007)23:7<605::AID-CEAT605>3.0.CO;2-0.

[58] R.K. Grenville, J.N. Tilton, Jet mixing in tall tanks: Comparison of methods for predicting blend times, Chem. Eng. Res. Des. 89 (2011) 2501–2506. doi:10.1016/j.cherd.2011.05.014.

[59] R. Kacker, S. Maaß, J. Emmerich, H. Kramer, Application of inline imaging for monitoring crystallization process in a continuous oscillatory baffled crystallizer, AIChE J. 64 (2018) 2450–2461. doi:10.1002/aic.16145.

[60] Y. Xiao, X. Li, C. Yang, J. Shen, Particle Scattering Photography Approach for Poorly Illuminated Multiphase Reactors. I: Theoretical Model and Simulation, Ind. Eng. Chem. Res. 57 (2018) 8396–8404. doi:10.1021/acs.iecr.7b05344.

[61] S. Castellano, L. Carrillo, N. Sheibat-Othman, D. Marchisio, A. Buffo, S. Charton, Using the full turbulence spectrum for describing droplet coalescence and breakage in industrial liquid-liquid systems: experiments and modeling, Chem. Eng. J. (2019). doi:10.1016/j.cej.2019.06.032.

[62] A.S. Heeres, K. Schroën, J.J. Heijnen, L.A.M. van der Wielen, M.C. Cuellar, Fermentation broth components influence droplet coalescence and hinder advanced biofuel recovery during fermentation, Biotechnol. J. 10 (2015) 1206–1215. doi:10.1002/biot.201400570.

[63] H.K. Versteeg, W. Malalasekera, An introduction to computational fluid dynamics: the finite volume method, 2nd ed, Pearson Education Ltd, Harlow, England ; New York, 2007.

[64] J.H. Ferziger, M. Perić, Computational methods for fluid dynamics, 3rd, Springer, Berlin ; New York, 2002.

[65] T. Ahmad, S.L. Plee, J.P. Myers, Fluent Theory Guide.

[66] M. Jenne, M. Reuss, A critical assessment on the use of k–ε turbulence models for simulation of the turbulent liquid flow induced by a Rushton-turbine in baffled stirred-tank reactors, Chem. Eng. Sci. 54 (1999) 3921–3941. doi:10.1016/S0009-2509(99)00093-7.

[67] W. Bujalski, Z. Jaworski, A.W. Nienow, CFD study of homogenization with dual rushton turbines—comparison with experimental results PART II: The Multiple Reference Frame, 80 (2002) 8.

[68] S. Baldi, M. Yianneskis, On the quantification of energy dissipation in the impeller stream of a stirred vessel from fluctuating velocity gradient measurements, Chem. Eng. Sci. 59 (2004) 2659–2671. doi:10.1016/j.ces.2004.03.021.

[69] M. Aoun Nabli, P. Guiraud, C. Gourdon, Numerical experimentation: a tool to calculate the axial dispersion coefficient in discs and doughnuts pulsed solvent extraction columns, Chem. Eng. Sci. 52 (1997) 2353–2368. doi:10.1016/S0009-2509(96)00517-9.

[70] M.S. Aoun Nabli, P. Guiraud, C. Gourdon, CFD Contribution to a Design Procedure for Discs and Doughnuts Extraction Columns, Chem. Eng. Res. Des. 76 (1998) 951–960. doi:10.1205/026387698525757.

[71] J.M. Bujalski, W. Yang, J. Nikolov, C.B. Solnordal, M.P. Schwarz, Measurement and CFD simulation of single-phase flow in solvent extraction pulsed column, Chem. Eng. Sci. 61 (2006) 2930–2938. doi:10.1016/j.ces.2005.10.057.

[72] V. Alopaeus, J. Koskinen, K.I. Keskinen, Simulation of the population balances for liquid–liquid systems in a nonideal stirred tank. Part 1 Description and qualitative validation of the model, Chem. Eng. Sci. 54 (1999) 5887–5899. doi:10.1016/S0009-2509(99)00170-0.

[73] A. Buffo, V. Alopaeus, Experimental determination of size distributions: analyzing proper sample sizes, Meas. Sci. Technol. 27 (2016) 045301. doi:10.1088/0957-0233/27/4/045301.

[74] M. Karimi, R. Andersson, An exploratory study on fluid particles breakup rate models for the entire spectrum of turbulent energy, Chem. Eng. Sci. 192 (2018) 850–863. doi:10.1016/j.ces.2018.08.016.

[75] J. Solsvik, H.A. Jakobsen, A review of the statistical turbulence theory required extending the population balance closure models to the entire spectrum of turbulence, AIChE J. 62 (2016) 1795–1820. doi:10.1002/aic.15128.

[76] S.G. Saddoughi, S.V. Veeravalli, Local isotropy in turbulent boundary layers at high Reynolds number, J. Fluid Mech. 268 (1994) 333. doi:10.1017/S0022112094001370.

[77] C.A. Coulaloglou, L.L. Tavlarides, Description of interaction processes in agitated liquid-liquid dispersions, Chem. Eng. Sci. 32 (1977) 1289–1297. doi:10.1016/0009-2509(77)85023-9.

[78] P.J. Becker, F. Puel, R. Henry, N. Sheibat-Othman, Investigation of Discrete Population Balance Models and Breakage Kernels for Dilute Emulsification Systems, Ind. Eng. Chem. Res. 50 (2011) 11358–11374. doi:10.1021/ie2006033.

[79] K. Van't Riet, J.M. Smith, The trailing vortex system produced by Rushton turbine agitators, Chem. Eng. Sci. 30 (1975) 1093–1105. doi:10.1016/0009-2509(75)87012-6.

[80] J. Solsvik, H.A. Jakobsen, A review of the statistical turbulence theory required extending the population balance closure models to the entire spectrum of turbulence, AIChE J. 62 (2016) 1795–1820. doi:10.1002/aic.15128.

[81] M.S. Aoun Nabli, P. Guiraud, C. Gourdon, CFD Contribution to a Design Procedure for Discs and Doughnuts Extraction Columns, Chem. Eng. Res. Des. 76 (1998) 951–960. doi:10.1205/026387698525757.

[82] M.M. Attarakih, H.-J. Bart, N.M. Faqir, Numerical solution of the bivariate population balance equation for the interacting hydrodynamics and mass transfer in liquid–liquid extraction columns, Chem. Eng. Sci. 61 (2006) 113–123. doi:10.1016/j.ces.2004.12.055.

[83] C. Gourdon, G. Casamatta, Influence of mass transfer direction on the operation of a pulsed sieve-plate pilot column, Chem. Eng. Sci. 46 (1991) 2799–2808. doi:10.1016/0009-2509(91)85149-R.

[84] A.J. Klee, R.E. Treybal, Rate of rise or fall of liquid drops, AIChE J. 2 (1956) 444–447. doi:10.1002/aic.690020405.

[85] R.J. LeVeque, Finite Difference Methods for Ordinary and Partial Differential Equations: Steady-State and Time-Dependent Problems, Society for Industrial and Applied Mathematics, 2007. doi:10.1137/1.9780898717839.

[86] G.F. Scheele, B.J. Meister, Drop formation at low velocities in liquid-liquid systems: Part I. Prediction of drop volume, AIChEJ. 14 (1968) 9–15. doi:10.1002/aic.690140105.